NASA CONTRACTOR REPORT

DEVELOPMENT OF AN EXTERNAL CERAMIC

INSULATION FOR THE SPACE SHUTTLE ORBITER

Part 2 - Optimization

edited by

Richard A. Tanzilli
General Electric Co., RESD
Philadelphia, Penna.

NATIONAL AERONAUTICS AND SPACE ADMINISTRATION   March 1973

COVER

DEVELOPMENT OF AN EXTERNAL CERAMIC

INSULATION FOR THE SPACE SHUTTLE ORBITER

Part 2 – Optimization

edited by

Richard A. Tanzilli
General Electric Co., RESD
Philadelphia, Penna.

NATIONAL AERONAUTICS AND SPACE ADMINISTRATION

FOREWORD

This report was prepared by the Re-entry and Environmental Systems Division (RESD) of the General Electric Company, Philadelphia, Pennsylvania under NASA Contract No. NAS 1-10533. The work was administered under the direction of the Langley Research Center's Thermal Protection Materials Branch with Mr. A. J. Chapman, III acting as Contract Monitor.

This report covers the work conducted from March 20, 1972 through November 20, 1972 at the RESD's Advanced Materials Development Laboratory. Dr. R. A. Tanzilli acted as Project Manager and edited the final report. This program was integrated with other current RESD Shuttle thermal protection system (TPS) development programs under the overall leadership of Mr. G. S. Hall, Program Manager, RESD Space Shuttle Programs.

The principal contributors to the technical effort and preparation of the final report are listed below:

Basic Insulation Development	R. C. Thuss, T. Ormiston and Dr. R. A. Tanzilli
Coating Development	P. N. Bolinger, T. Ormiston and Dr. R. A. Tanzilli
Microstructural Characterizations	T. A. Harris, Jr. (XRD)
Thermal Property Evaluation and Technique Development	J. P. Brazel, J. Hanson
Mechanical Property Evaluation and Test Technique Development	D. P. Lowe

In addition, the authors acknowledge the technical support of the following individuals:

V. N. Saffire, Manager, Advanced Materials Development Laboratory
Dr. P. D. Gorsuch, Senior Materials Engineer, Technical Systems
  Engineering, Technology Engineering Laboratory
Dr. S. Musikant, Manager, Metallurgy & Ceramics Laboratory

Also, the authors wish to thank Mrs. Nancy Cerio for typing the final report draft manuscript.

TABLE OF CONTENTS

TABLE OF CONTENTS (Continued)

LIST OF ILLUSTRATIONS

LIST OF ILLUSTRATIONS (Continued)

LIST OF TABLES

SECTION 1

INTRODUCTION

This report documents an 8 month applied research program which was undertaken by the General Electric Company's Re-entry and Environmental Systems Division (RESD) to define an optimized RSI material system for use on the Space Shuttle Orbiter (as defined in NASA-Langley Statement of Work L 12-825A - Modification No. 4). Program logic, including major decision points which influenced program direction are illustrated in the flow diagram shown on the following page. Several advanced material development areas in which further research is recommended are also identified.

A review of the work accomplished under each subtask is given in Sections 2, 3 and 4 of this report. Program conclusions and recommendations are described in Section 5. A series of Appendices have been added, after the conclusions and recommendations, which include physical property data and descriptions of test techniques used for design data generation.
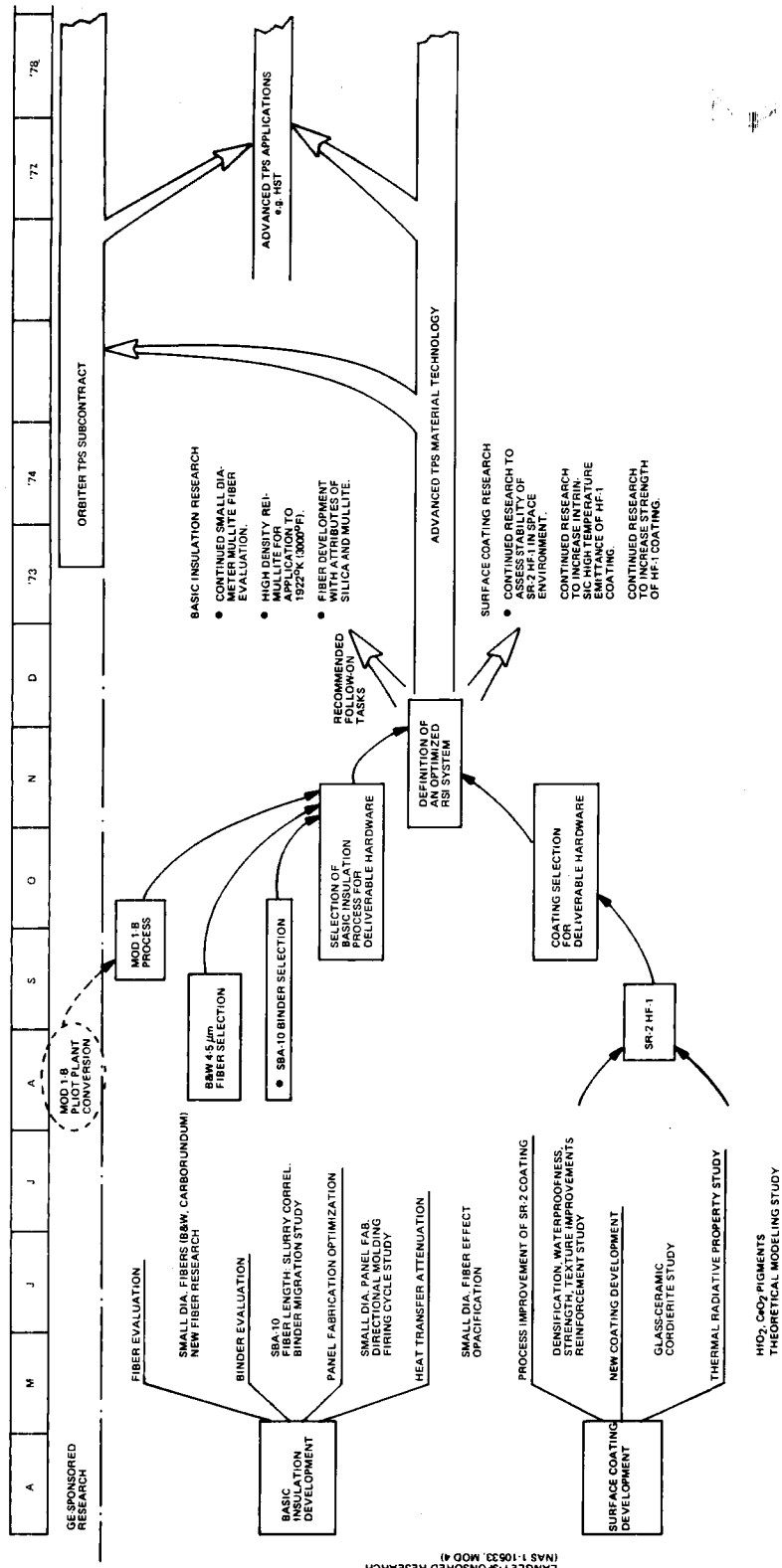
Task summary for NASA–Langley RSI optimization program (NAS 1-10533, mod 4)

GE SPONSORED RESEARCH

ORBITER TPS SUBCONTRACT

MOD 1 B PILOT PLANT CONVERSION

MOD 1 B PROCESS

B&W 4-5 μm FIBER SELECTION

SBA-10 BINDER SELECTION

SELECTION OF BASIC INSULATION PROCESS FOR DELIVERABLE HARDWARE

DEFINITION OF AN OPTIMIZED RSI SYSTEM

RECOMMENDED FOLLOW-ON TASKS

ADVANCED TPS APPLICATIONS e.g. HST

ADVANCED TPS MATERIAL TECHNOLOGY

BASIC INSULATION RESEARCH
- CONTINUED SMALL DIA-METER MULLITE FIBER EVALUATION.
- HIGH DENSITY REINFORCED MULLITE FOR APPLICATION TO 1922°K (3000°F).
- FIBER DEVELOPMENT WITH ATTRIBUTES OF SILICA AND MULLITE.

SURFACE COATING RESEARCH
- CONTINUED RESEARCH TO ASSESS STABILITY OF SR-2 HF-1 IN SPACE ENVIRONMENT.
- CONTINUED RESEARCH TO INCREASE INTRIN. SiC HIGH TEMPERATURE EMITTANCE OF HF-1 COATING.
- CONTINUED RESEARCH TO INCREASE STRENGTH OF HF-1 COATING.

COATING SELECTION FOR DELIVERABLE HARDWARE

SR-2 HF-1

BASIC INSULATION DEVELOPMENT

FIBER EVALUATION
SMALL DIA. FIBERS (B&W, CARBORUNDUM) NEW FIBER RESEARCH

BINDER EVALUATION
SBA-10
FIBER LENGTH. SLURRY CORREL. BINDER MIGRATION STUDY

PANEL FABRICATION OPTIMIZATION
SMALL DIA. PANEL FAB. DIRECTIONAL MOLDING FIRING CYCLE STUDY

HEAT TRANSFER ATTENUATION
SMALL DIA. FIBER EFFECT OPACIFICATION

SURFACE COATING DEVELOPMENT

PROCESS IMPROVEMENT OF SR-2 COATING
DENSIFICATION, WATERPROOFNESS, STRENGTH, TEXTURE IMPROVEMENTS REINFORCEMENT STUDY

NEW COATING DEVELOPMENT
GLASS-CERAMIC CORDIERITE STUDY

THERMAL RADIATIVE PROPERTY STUDY
HfO₂, CeO₂ PIGMENTS THEORETICAL MODELING STUDY

LANGLEY-SPONSORED RESEARCH (NAS 1-10533, MOD 4)

A M J J A S O N D '73 '74 '72 '78

2

SECTION 2

BASIC INSULATION DEVELOPMENT

2.1 PROCESS IMPROVEMENT AND PROPERTIES OPTIMIZATION

2.1.1 INTRODUCTION

The primary objective of this research has been to identify and evaluate processes for improving the mechanical and thermal properties of the REI-Mullite basic insulation. As described in the Phase 1 portion of this program (Reference 1), the basic insulation consists of two major components: the Babcock and Wilcox (B&W) experimental mullite fiber and a silica-boria-alumina binder. These components are schematically illustrated on the phase diagram shown in Figure 1. The B&W fiber is a quaternary oxide system whose mean composition lies within the phase equilibria tetrahedron. As pointed out by Fetterolf in Reference 2, considerable variations in fiber properties may be achieved by adjustment of the relative proportions of the four oxide phases. For example, the presence of boric oxide and phosphorous pentoxide ($\sim$ 6w/o) have been shown to result in significant fiber strength improvement as a result of grain-growth inhibition. Although not evaluated on this study, it is anticipated that a considerable lattitude in fiber property tailoring should be possible with this relatively unexplored quaternary oxide system. Also shown in Figure 1 is the mean composition of the silica-boria-alumina binder (SBA-10) which lies on one of the ternary triangle faces of the tetrahedron (cross-hatched). This binder composition has resulted in near optimum fillet formation and is compatible with the fiber in terms of phase and dimensional stability and physical properties.

The basic insulation improvement study concentrated upon evaluating variables which could result in significant near-term gains in mechanical behavior and insulation effectiveness of the previously described baseline system. The approaches undertaken included: evaluation of small diameter fibers, optimization of binder: slurry characteristics, evaluation of techniques for controlling fiber orientation, optimization of firing cycle, and the evaluation of methods for improving insulation efficiency. A detailed discussion of these basic insulation improvement studies undertaken are contained in the following subsections.

2.1.2 FIBER EVALUATIONS

Small-diameter fiber evaluations included laboratory quantities of the Babcock and Wilcox (B&W) mullite fiber and Carborundum's high alumina-silica fiber. The B&W fibers were formed by two different processes: the standard spinning technique and a more recent blowing technique which was being developed under NASA-Lewis Research Center sponsorship (Contract No. NAS 3-16764). It has been found that the fibers formed by the blown process are shorter in length and have a greater proportion of fiber diameters below 2 microns when compared to the spun process. A comparison of fiber diameter distributions for the two types of fibers processed to yield fiber

3

QUATERNARY SYSTEM

$Al_2O_3 - SiO_2 - B_2O_3 - P_2O_5$

SiO_2 (1996°K)

SBA-10 BINDER
(TERNARY SURFACE)

FIBER COMPOSITION
(WITHIN TETRAHEDRON)

B_2O_3 (723°K)

$2S \cdot P$ (1393°K)

$S \cdot P$ (1563°K)

$B \cdot P$ (1723°K)

P_2O_5 (842°K)

$3A \cdot 2S$ (2123°K)

$A \cdot 3P$

$A \cdot P$

(1308°K) $2A \cdot B$

(2225°K) $9A \cdot 2B$

Al_2O_3 (2323°K)

$A = Al_2O_3$ $B = B_2O_3$ $S = SiO_2$ $P = P_2O_5$
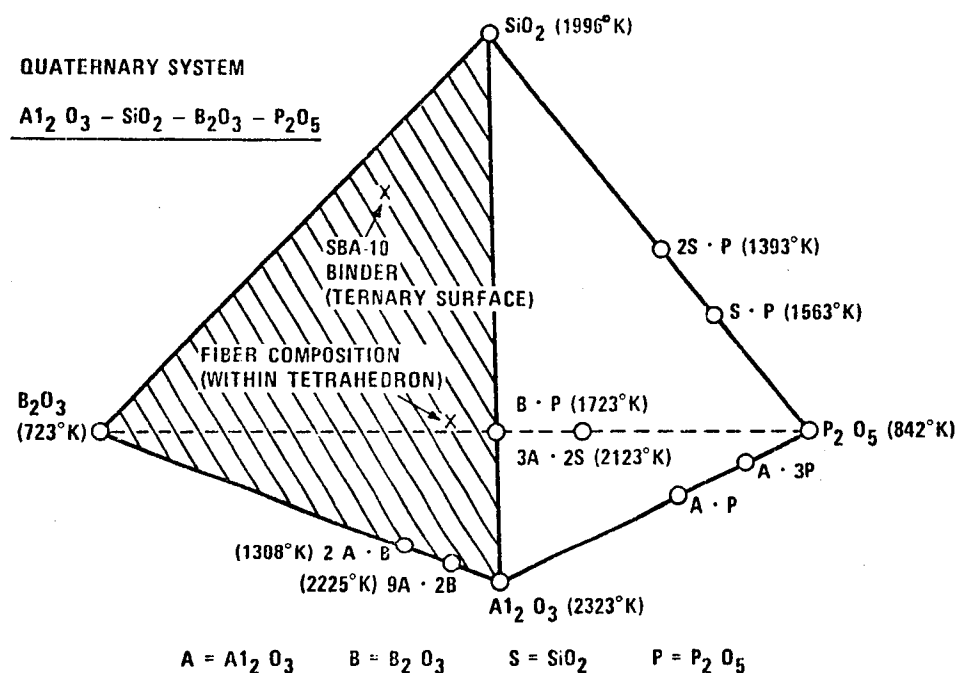
Figure 1. Phase diagram for the REI-Mullite system showing
binder and fiber mean compositions.

diameters smaller than the standard B&W product is illustrated by the histograms
shown in Figure 2. The as-fabricated fibers formed by both processes have similar
phase compositions: γ-alumina, mullite and an amorphous component. Typical x-ray
diffraction patterns are shown in Figure 3 for each process. Scanning electron micro-
graphs of both types of fibers are illustrated in Figure 4. A considerable amount of
unfiberized debris (shot) has been detected in the limited quantity of material produced
to date. Elimination of this debris by post-fabrication cleaning procedures or,
preferably, through improved processing would be required before implementation into
the current REI-Mullite system.

In addition to the B&W small diameter fibers, an experimental Carborundum, high
alumina-silica fiber (62 w/o Al_2O_3, 38 w/o SiO_2) was evaluated. Figures 5 and 6 show
a typical fiber diameter histogram and scanning electron micrograph of as-fabricated
batting in which a series of elutriation treatments were used by the vendor to remove
a significant portion of "shot" from the original batting. It should be noted that the
experimental Carborundum fiber is formed from the melt which yields, in addition to a
fibrous component, a significant weight percent of "shot" (non-fibrous component).
This phenomenon is presumably due to the non-ideal viscosity-surface tension behavior
(for fiber-forming) of high alumina-silica glasses.

4
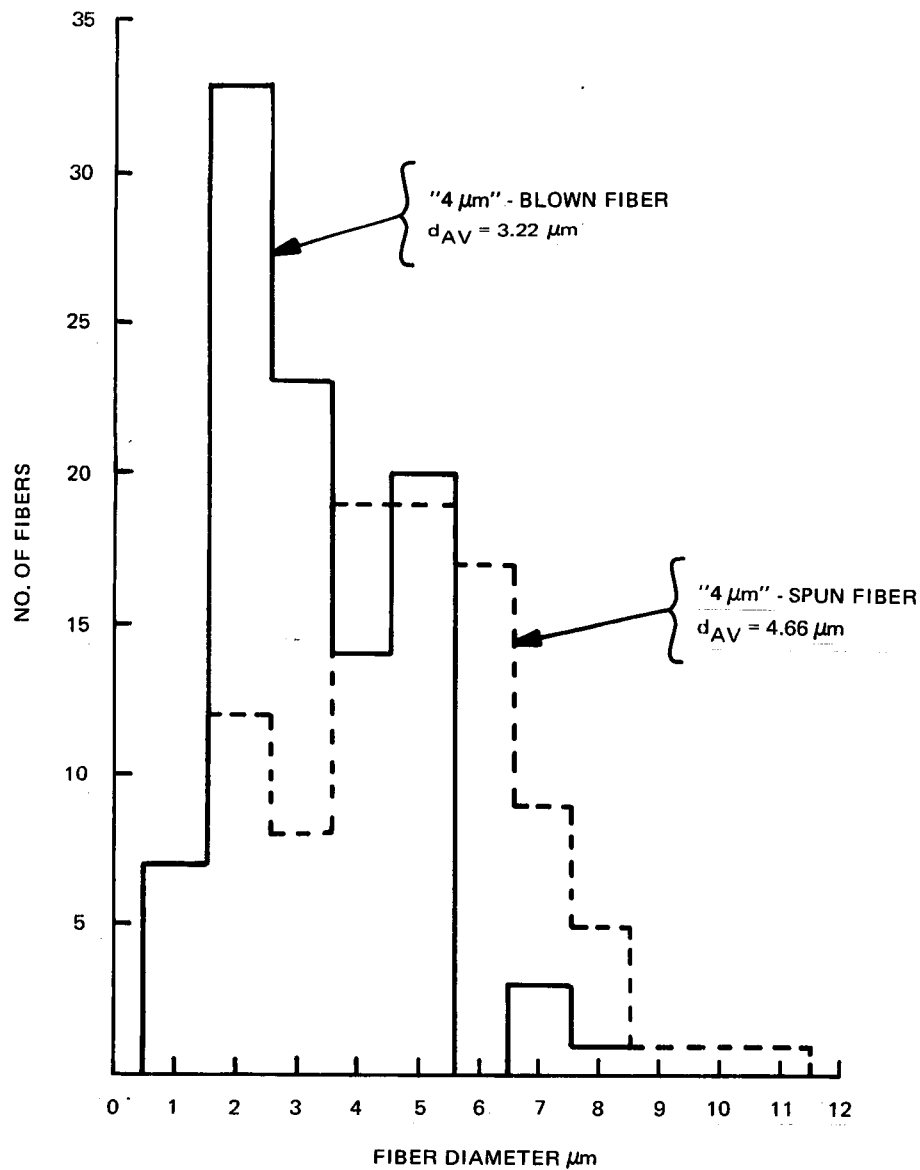
Figure 2. Comparison of fiber diameter distributions for small-diameter Babcock and Wilcox experimental mullite fibers

(a) SPUN FIBER

GAMMA ALUMINA

2θ

(b) BLOWN FIBER

GAMMA ALUMINA

2θ
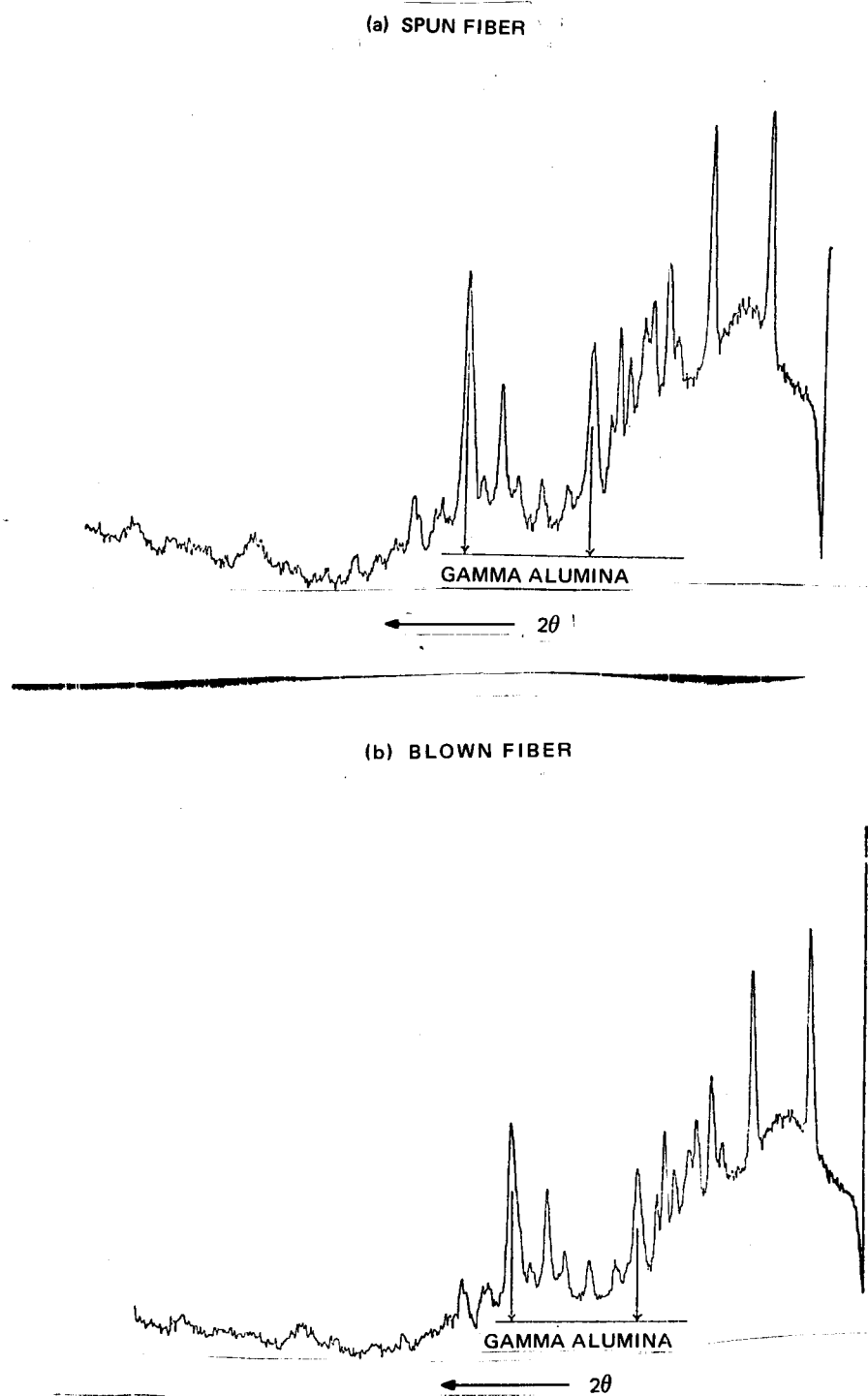
Figure 3. Comparison of x-ray diffraction patterns for small-diameter Babcock and Wilcox experimental mullite fibers. γ -alumina lines identified; remaining diffraction lines are those of mullite.

6
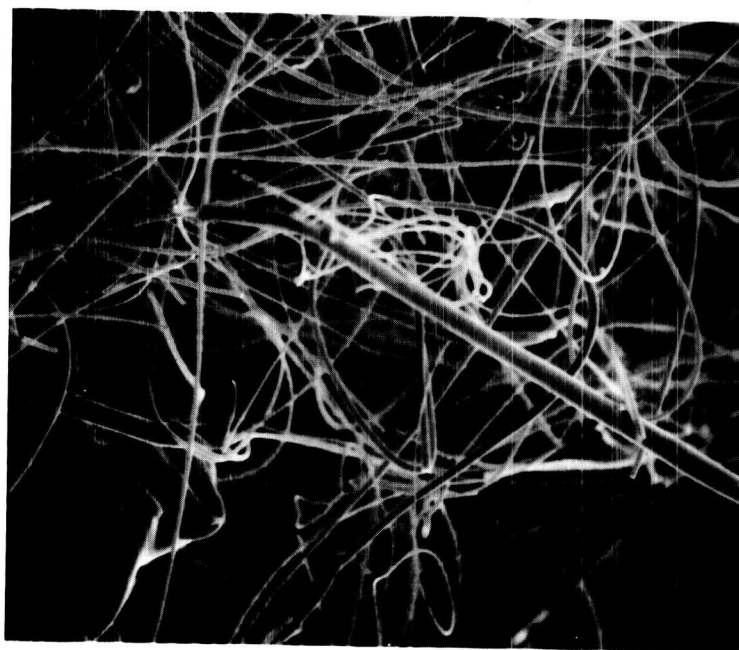
(a) As received – blown fiber
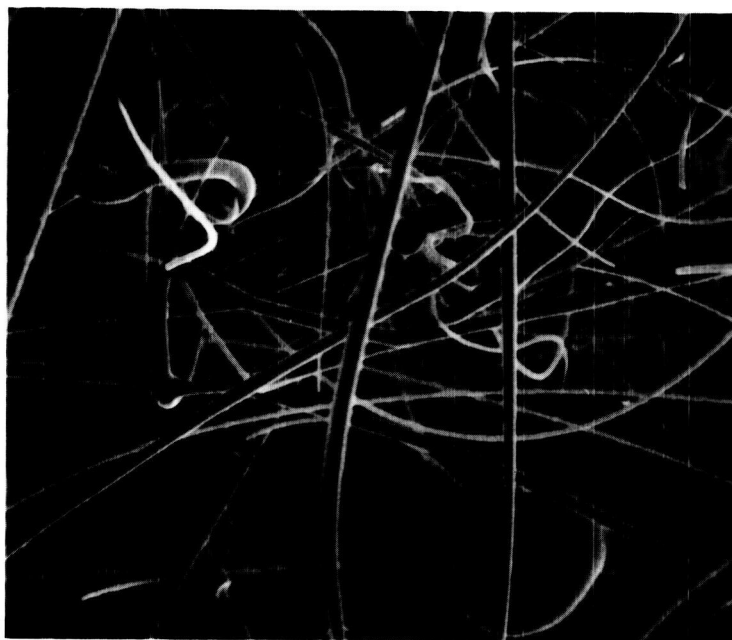
(b) As received – spun fiber

Figure 4. Scanning electron micrographs of small diameter Babcock and Wilcox experimental mullite fibers. (Mag. 300X)
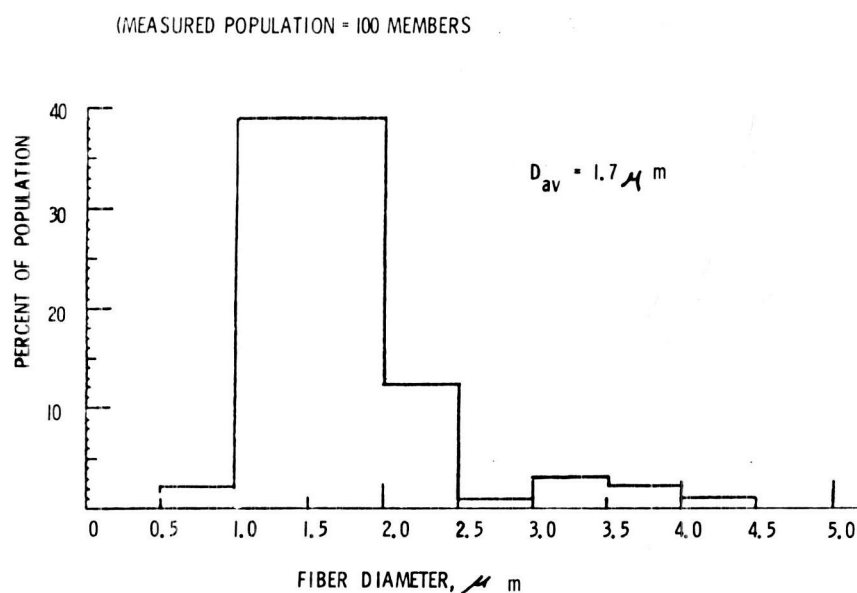
Figure 5. Fiber diameter distribution for the experimental melt-
formed high alumina-silica Carborundum fiber
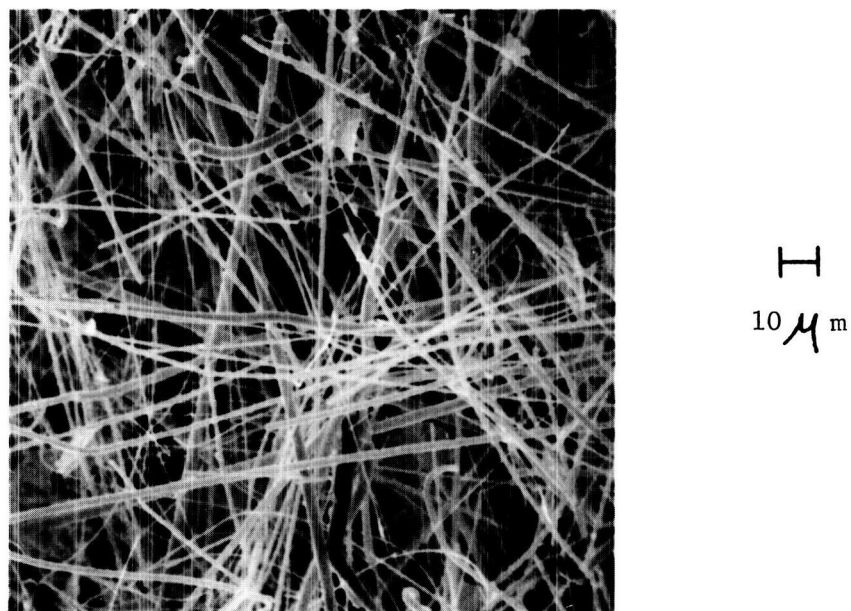
Figure 6. Scanning electron micrograph of the experimental melt-
formed high alumina-silica Carborundum fiber

8

Experimental laboratory panels were fabricated using each of these fibers and mechanical and thermal properties evaluated. The results of these evaluations are described in Section 2.1.4 and 2.1.5.

2.1.3 BINDER EVALUATION

2.1.3.1 SBA-10 Binder

The Mod 1-A binder (SBA-10), which is a proprietary GE-RESD development characterized on the Phase 1 portion of this program, was used as the baseline system for evaluating the effects of small diameter fibers on basic insulation mechanical and thermal behavior. The SBA-10 binder system was evolved through a study of the softening points of a number of silica-boria-alumina glasses. In these studies, increasing quantities of alumina were added to a non-alumina containing borosilicate mixture until the desired high temperature flow characteristics were achieved. In particular, the formulation was selected which would wet the fibers as well as concentrate at the fiber intersections. The strength and strain-to-failure characteristics of these composites were improved compared to the original Mod 1 process with an incremental improvement in insulation effectiveness. It was further found that the SBA binder (74.8 percent SiO_2, 18.7 percent B_2O_3 and 6.5 percent Al_2O_3) was resistant to α - cristobalite formation for times up to six hours at 1644°K (2500°F).

Figure 7 shows the SBA-10 binder composition located on the SiO_2-B_2O_3-Al_2O_3 phase diagram proposed by Gielisse and Foster (Reference 3). Reaction of the SBA-10 binder with the mullite-base fibers during exposure of the rigidized composites to temperatures of 1533°K (2300°F) or higher increases the binder liquidus temperature. Also shown in Figure 7 is the direction (shown by arrows) in which the average binder composition is expected to change due to this high temperature exposure.

2.1.3.2 Fiber-Length Optimization

One of the major variables which effect the physical properties of rigidized fibrous insulations is the fiber length. With the gravity-drain panel formation technique (currently used for REI-Mullite processing) excessive fiber chopping during the mixing phase yields high-density panels with inferior mechanical properties (on a strength: weight basis). It has been found that fiber diameter and fiber diameter distribution determine, to a large extent, the final fiber-length distribution for a fixed fiber:binder slurry mixing time.

A literature search was conducted to uncover possible experimental techniques suitable for grading fibers by length, thus offering a possible approach for controlling this parameter during processing. A commercial source for such an instrument was found: Ultrasonoscope Company Limited, Sudbourne Road, London SW2. A schematic of the original prototype which, sorted into two grades, is illustrated in Figure 8. Subsequent machines which sort into three classes or more have been based upon the
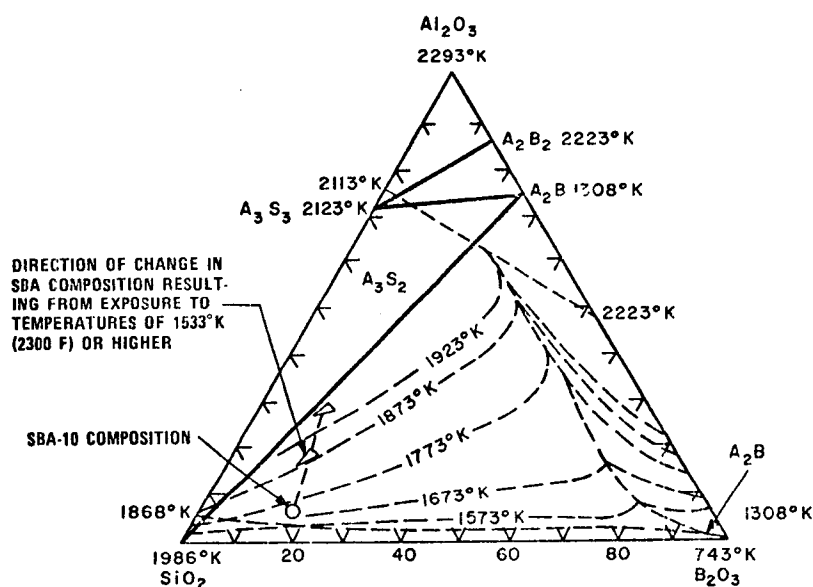
Figure 7. Liquidus surface of the SiO_2-B_2O_3-Al_2O_3 ternary oxide system showing the location of the SBA-10 binder composition.
Note: $A(Al_2O_3)$; $B(B_2O_3)$, $S(SiO_2)$
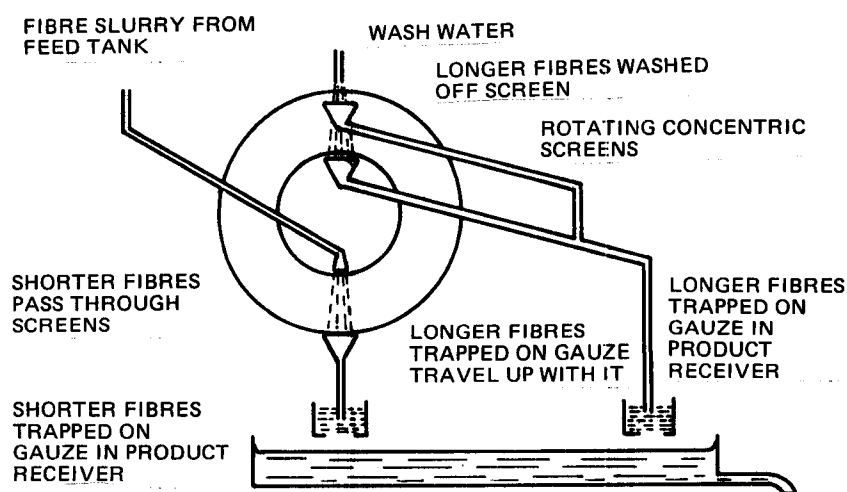
Figure 8. Schematic of a prototype single-wheel classifier for separating two fiber-length size classes (Reference 5)

10

prototype design. The principle of operation is as follows: fibers are first dispersed in water and then sprayed on the inside of a rotating drum of wire gauze. Short fibers fall through the gauze while longer fibers are carried up to the top of the drum where a water spray disperses the fiber onto a second collecting tray. The mesh size of the gauze determines the approximate size class at which separation occurs. By increasing the number of wheels, additional size class separations are achieved. A schematic of such a device is illustrated in Figure 9. A more detailed description of these fiber-length separators is given in References 4 and 5.

2.1.3.3 Correlation of Fiber length with Slurry Viscosity

One of the most critical parameters in the panel fabrication process is the average fiber length that is produced during the fabrication process. Presently, control on this parameter is achieved by keeping the fiber chopping time constant from panel to panel. Since this technique does not always result in uniform panel properties, it is desirable to have a technique which measures some fundamental property of the fiber-binder slurry which is a function of the fiber length.

One such property is the viscosity or, more technically correct, the consistency of the slurry. A correlation of consistency measurements with fiber-chopping time was made on the SBA-10 binder-fiber slurry. Tests were run on a Stormer Viscosimeter using a paddle-type rotor. The procedure was a modification of ASTM standard D-562. The selection of a representive sample from the binder:fiber slurry was critical for achieving reproducible measurements. A non-representative sample which was highly concentrated would tend to form a turbulent mixing vortex while a dilute sample would tend to settle before a measurement could be made.

The fibrous slurry on which consistency readings were taken was produced using scaled fabrication equipment. The fibers were chopped in the SBA-10 binder for times of 4, 7, 12 and 22 minutes. Consistency data (as measured by the time required for one hundred revolutions of the paddle rotor) was generated on 500 ml samples taken after several chopping times. The data is shown in Table 1 below.

Fiber length distributions were determined for the two extreme fiber chopping times (2 and 20 minutes) and correlated with the Stormer viscosimeter data reported earlier. It was possible to distinguish, on the basis of average slurry fiber length, between slurries chopped for 2 and 20 minutes. Figure 10 compares the fiber length distribution functions for the two chopping times. The ability to correlate fiber-length distribution with an in-process slurry-viscosity measurement should improve insulation-fibrication quality control.

11
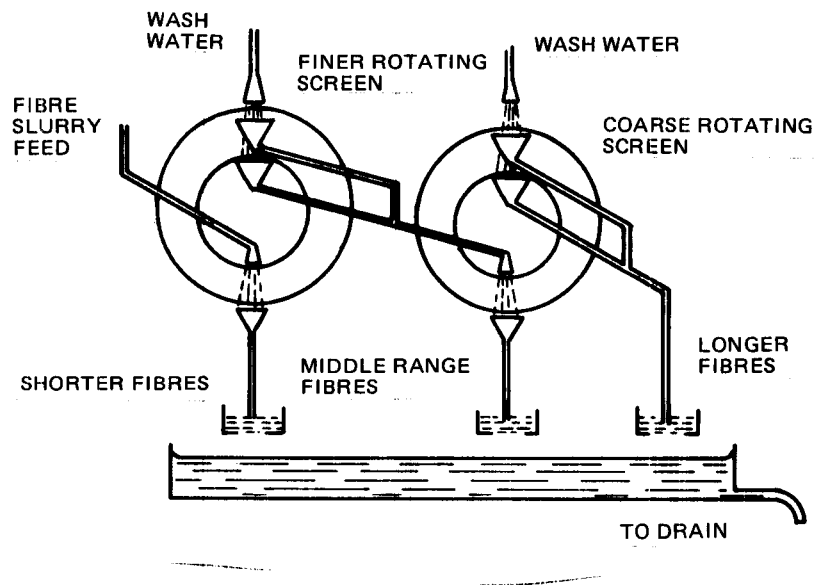
Figure 9. Schematic illustration of a two-wheel fiber classifier for
separating into three fiber-length size classes (Reference 5)

TABLE 1

Fiber-slurry Consistency Data Recorded Using the Stormer Viscosimeter.

Fiber Addition Time (Minutes)	Fiber Chopping Time (Minutes)	Consistency (Secs/100 Revs.)
2	2	19.3
2	5	18.8
2	10	18.1
2	20	17.7
SBA-10 Binder		17.5

12
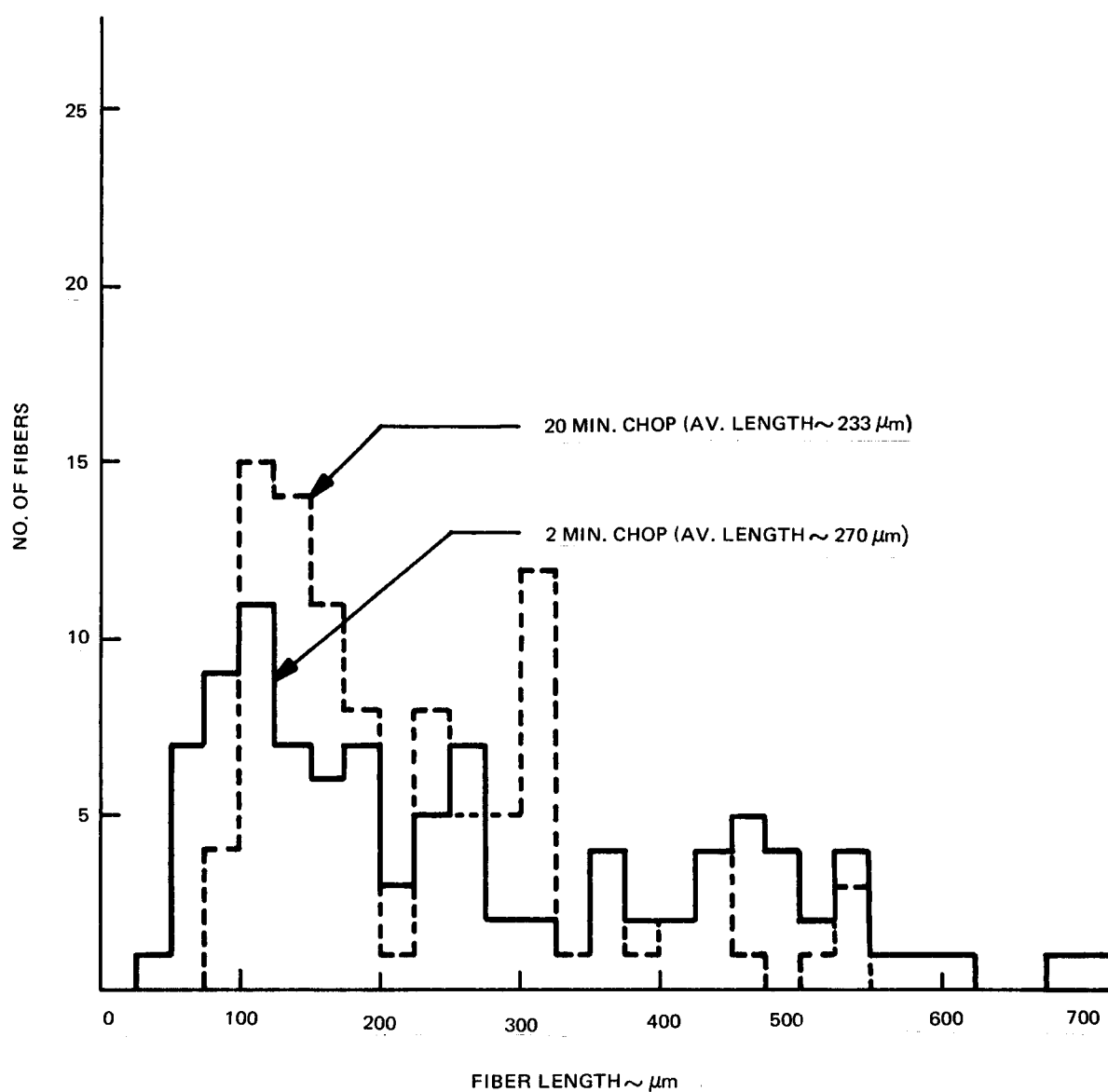
Figure 10. Comparison of fiber length distribution as
a function of slurry chopping time

2.1.3.4 Binder Migration Study

Several methods have been explored for prevention of binder migration through the REI panel during drying. Aside from slow, humidity-controlled, air drying procedures used in most common ceramic drying applications, there have been two methods developed for controlling the migration of the binder to the surface of panel. The first is to gel the binder immediately after the binder has drained by passing ammonia through the wet tile. The ammonia precipitates colloidal particles of aluminum hydroxide which either absorb or trap the other binder constitutents.

Another method used for prevention of binder migration was to add enough ammonia to the binder to make it slightly alkaline, dissolve alginic acid in the binder, and then pass HC1 gas through the wet tile. In this system, the alginate precipitates and traps the binder in the tile. This system works somewhat better than the ammonia-gelled system with regards to binder migration, however, it does alter the casting procedure since the binder solution becomes much more viscous with the addition of the alginate.

2.1.4 PANEL FABRICATION OPTIMIZATION

2.1.4.1 Small-Diameter Fiber Panel Fabrication

Several laboratory panels were fabricated using small-diameter Babcock and Wilcox (B&W) experimental mullite fibers and, also, Carborundum's experimental 62 Al_2O_3 – 38 SiO_2 fiber. The Mod 1-A REI-Mullite process was scaled-down in terms of mixing and molding techniques for this study primarily because of the high initial cost of the B&W small-diameter fibers ($500/lb). A description of the panels fabricated is given in Table 2; Figures A-1 through A-10 (Appendix 1) illustrate the mechanical behavior data obtained on these panels in terms of tensile strength, strain and Young's modulus. The following conclusions have been reached regarding these data:

1. Low-density panels using both types of B&W fibers exhibited comparable in-plane mechanical behavior (Figures A-1 and A-2).

2. A comparable-density panel using the Carborundum fiber (Figure A-3), although exhibiting similar in-plane strength, had failure strains approximately half that of the B&W panels (with tensile moduli double that of the B&W panels). This could be the result of the lower fiber:binder ratio required for fabricating a usable panel with the smaller-diameter Carborundum fiber.

3. Similar transverse mechanical behavior was observed for the B&W panels (Figure A-4); however, the corresponding Carborundum panel had approximately half the transverse tensile strength (also shown in Figure A-4).

4. Higher-density panels (FJC-4 and FJC-1), using the B&W-Spun and Carborundum fibers respectively, exhibited increased in-plane tensile strength, the B&W fiber again showing higher in-plane failure strain and corresponding lower tensile moduli (compared to the Carborundum panel) (Figures A-5 and A-6).

14

Table 2. Description of Processing Parameters for Small Diameter Fiber Panels.

Panel Code	Fiber Type	Panel Density		Panel Size		Estimated Fiber Length Range for Majority of Fibers (μm)	Average Fiber Diameter (μm)	Fiber Wt. Kg	Binder Conc. gms. (solid)/liter	Fiber:Binder Ratio	Mixing Technique	Mechanical Property Data
		Kg/m³	pcf	cm.	In.							
FJC-5	B&W-Spun(1)	208.13	13.0	15.74x15.74x5.72	6x6x2-1/4	200-500	4.66	0.240	52	93:7	Marine Impellor	Fig. A-1, A-4
FJC-8	B&W-Blown(2)	200.13	12.5	15.74x15.74x5.72	6x6x2-1/4	200-500	3.22	0.240	52	80:20	Marine Impellor	Fig. A-2, A-4
FJC-6	Carborundum(3)	212.93	13.3	30.48x30.48x5.40	12x12x2-1/8	100-300	1.70	0.599	26	70:30	Marine Impellor	Fig. A-3, A-4
FJC-4	B&W-Spun	294.58	18.4	15.74x15.74x2.54	6x6x1	100-300	4.66	0.240	52	80:20	Shear Blade	Fig. A-5
FJC-1	Carborundum	294.58	18.4	30.48x30.48x6.35	12x12x2-1/2	100-300	1.70	0.898	26	68:32	Marine Impellor	Fig. A-6
FJC-12	B&W-Spun	201.73	12.6	15.74x15.74x6.35	6x6x2-1/2	10,000-50,000	4.66	0.240	52	80:20	Paddle	Fig. A-8, A-9
FJC-11	B&W-Blown	212.93	13.3	15.74x15.74x6.35	6x6x2-1/2	1,000-5,000	3.22	0.240	52	76:24	Paddle	Fig. A-7, A-9
FJC-9	B&W-Spun	225.74	14.1	25.40x48.26x6.03	10x19x2-3/8	300-700	4.66	1.315	52	79:21	Marine Impellor	Fig. A-10

(1) Fiber Distribution - Figure 2

(2) Fiber Distribution - Figure 2

(3) Fiber Distribution - Figure 5

15

It should be noted that the high-density B&W panel was fabricated using the pilot-plant process developed for the standard 4.7μm average diameter B&W fiber; it is believed that excessive fiber chopping during mixing was the cause of the high formation density. Subsequent low-density B&W panels (Table 2, FJC-5 and FJC-8) utilized a less severe mixing procedure (Marine Impellor).

5. Since in-plane tensile strength, using the modified (scaled) pilot-plant Mod 1-A process, was yielding low in-plane tensile strength, it was suspected that fiber lengths were too short. A series of panels FJC-11 and 12) were fabricated using a wooden paddle to mix the fiber:binder slurry. The mechanical behavior data for the panels (Figures A-7, A-8 and A-9) indicated that the resulting long fiber lengths severly limited mechanical properties. An optimum fiber length would appear to be one intermediate between shear-blade and marine-impellor mixing. The extremely low transverse directional strengths reflect the planar arrangement of the fibers caused by the long lengths.

6. A pilot-plant sized panel was fabricated using the B&W-spun fiber (FJC-9) to evaluate whether the generally poor mechanical properties were due to inapplicable scaling of the pilot-plant Mod 1-A process. (It should be noted that panel FJC-5 was a laboratory-size panel). Fiber lengths for this panel were reduced by using a marine impellor for mixing (as was FJC-5). In-plane mechanical behavior data for this panel are shown in Figure A-10. Specimens 1, 2 and 3, corresponding to the top half of the as-cast panel, indicated that mechanical integrity comparable to the 4.7μm B&W fiber can be achieved using the smaller diameter B&W-spun fiber. However, the data-scatter observed for this panel (and earlier panels) indicated that a major change in previously developed processing parameters would be required.

7. Dimensional stability data obtained on processed panels, which were subsequently heat-treated for 5 hours at 1644°K (2500°F), led to the following conclusions:

    a. Both the B&W-spun and -blown fibers, when processed into panels using the SBA-10 binder, demonstrated the excellent dimensional stability of the B&W fiber, as shown in Table A-1.

    b. Panels fabricated using the Carborundum fiber exhibited unacceptable shrinkage levels (compared to the B&W panels). Significantly higher transverse shrinkage was observed for the lower-density Carborundum panels.

Since the small-diameter fibers were only available in limited quantities, and since no significant advantage in mechanical behavior was observed using currently-available developmental material, it was concluded that additional program tasks (including hardware deliverables) would be implemented using the less costly and readily available standard 4.7 μm average diameter B&W fiber. As noted in Section 2.1.5.1, however, significant reductions in thermal conductivity were obtained using the small-diameter fibers and, therefore, further research with small-diameter fibers is fully justified.

16

2.1.4.2 Mod 1-B Process

During the later part of this study, a major breakthrough in upgrading Mod 1-A REI-Mullite properties was achieved through a modified firing procedure. Although developed on a concurrent in-house sponsored activity, the Mod 1-B process was used for program deliverables. The Mod 1-B material is fired in an atmosphere which appears to modify the interfacial tension of the binder phase on the mullite fibers. As a result, the binder preferentially flows to the fiber intersections. Hence, more efficient use is made of the available binder and strength and strain-to-failure are increased. Figure 11 presents data obtained on experimental panels of the Mod 1-B REI-Mullite produced in the GE-RESD pilot plant using the standard $4.7\,\mu$m diameter B&W fibers. This material is undergoing extensive characterization, but these data are adequate for indicating the magnitude of the property improvement achieved through modification of the firing cycle.

2.1.4.3 Directional Molding

The mechanical behavior of panels formed by the gravity-drain process are orthotropic in nature. The plane normal to the pressing direction is the plane of isotropy. The tensile strength and Young's modulus are significantly higher in this plane (xy-plane) compared to the transverse plane (z-plane). However, tensile strain capability in the xy-plane is lower than that in the transverse plane (z-plane). A directional molding technique was developed to initially explore the feasibility of reversing the in-plane and transverse properties such that maximum strength would be achieved in the transverse direction and maximum strain capability in-plane (xy-plane). Figure 12 illustrates the apparatus fabricated for achieving these properties. The principle of operation, sketched in Figure 13, is described below.

The fiber-binder slurry is poured into the xz plane of the mold with the y dimension being the pour depth. The panel is compressed by dead-weight loading in the y-direction to a nominal fiber density of 144.18 kg/m^3 (9 lb/ft^3). During this phase of the molding, the fibers are randomly oriented in the xz plane with significantly less fibers going in the y direction than in either the x or z. The mold is then activated and the panel is compressed approximately 10% in the x direction. This has the effect of forcing the fibers to be lined up parallel to the z axis. In the optimum situation, fibers would be forced out of the x direction systematically into both the z and y directions such that the mechanical properties in the x and y directions would become similar (i.e., medium strength, high strain) and in the z direction would be significantly different (high strength, low strain).

The measured mechanical properties for the directionally molded panel are as shown in Table 3. If the panel had not been directionally molded, the properties in the x and z directions should be identical. As can be seen from the data, this is not the case.

17
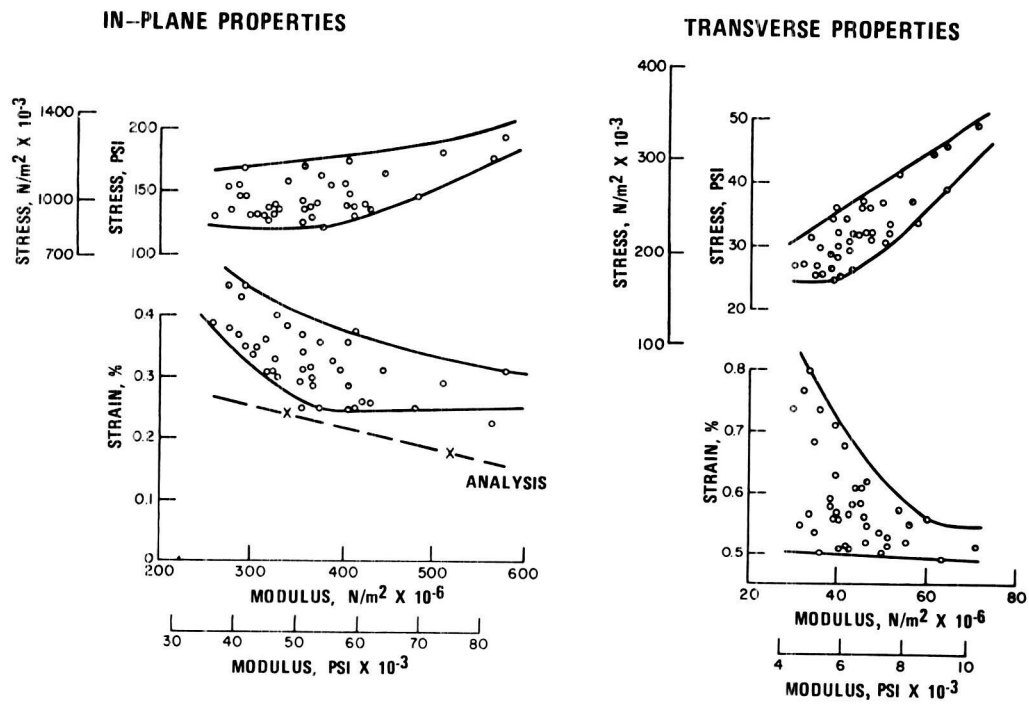
Figure 11. Mechanical behavior of Mod 1-B REI-Mullite in tension.
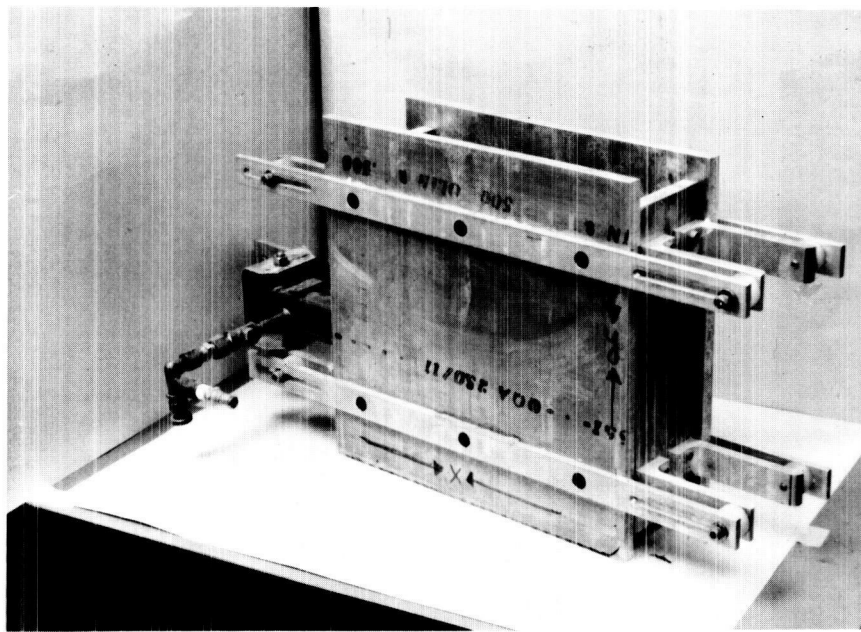
Figure 12. Photograph of directional molding apparatus.
Principal panel directions are identified on
photograph as: "X", "Y" and "Z"

18

DIRECTION OF
FIBER-BINDER POURING (XZ-PLANE)

MOVABLE SIDES
FOR COMPRESSING
PANEL IN X-DIRECTION
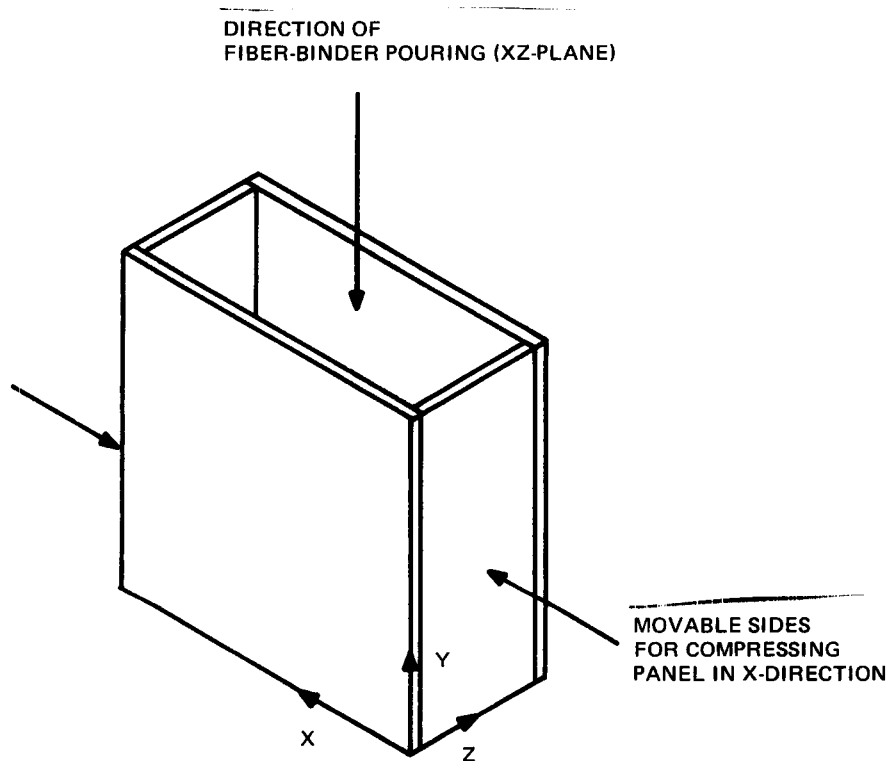
Figure 13. Sketch of directional molding device showing directions
of pouring and mechanically-applied compression.
Compression in Y-direction is achieved by gravity-drain
through base of mold with dead-weight applied in the
XZ plane.

The data does indicate that there was definitely some perferential orientation in the
z direction achieved by compression in the x direction; both the modulus and the
failure strain averages are significantly different in the x and z directions, correspond-
ing to what would be expected if fibers were preferentially oriented parallel to the
z axis. It is apparent from the data that considerably more x compression would be
required to yield specimens with equal properties in the x and y directions. The data
does indicate, however, that higher strain-to-failure can be achieved in both the x and
y directions by directional molding or selective fiber orientation. Extension of this
concept to three-directional molding should enable an isotropic panel to be fabricated.

2.1.4.4 Effect of Coating Firing Cycle on Mechanical Properties of Basic Insulation

The B&W experimental mullite fiber, being a polycrystalline ceramic, experiences
some degradation in mechanical properties as a result of grain-growth. The kinetics
of grain-growth with this quaternary oxide system have not been established but it is
known that B_2O_3 and P_2O_5 act as grain-growth inhibitors. (Reference 2). It has also
been shown that both of these oxides tend to vaporize from the fiber at elevated tempera-
tures for extended times as shown in Figure 14. (Reference 6).

19

Table 3. Tensile Properties of Directionally Molded REI-
Mullite Test Temperature = 297°K (75°F)

Test Direction	Specimen No. (1)	Ultimate Tensile Strength kN/m^2	Elastic Modulus GN/m^2	Strain-at-failure Percent
X	1	229.60	129.63	0.246
	2	306.14	155.14	0.329
	3	318.55	151.69	0.281
	4	281.32	138.59	0.317
	$\bar{X}$	292.35	143.42	0.293
Y	1	113.77	51.02	0.259
	2	110.32	45.51	0.272
	3	106.18	34.48	0.402
	4	112.59	34.48	0.442
	$\bar{X}$	110.32	41.37	0.344
Z	1	458.52	311.65	0.147
	2	242.70	137.90	0.239
	3	343.37	248.91	0.101
	4	259.94	137.90	0.220
	$\bar{X}$	326.13	208.92	0.177

NOTES: (1) Bonded Butt Tensile Test, one cm square

When the fiber is combined with the SBA-10 binder during the rigidization process, the resulting composite properties reflect the combined effect of binder and fiber. It has found that surface coated basic-insulation mechanical properties show considerably less degradation compared to uncoated basic insulation when fired under identical temperature-time histories.

In order to further capitalize on this observed phenomena, it has been found that firing the surface coating in a sealed-enclosure tends to completely eliminate basic insulation strength degradation during this processing stage. Table 4 lists a consistent set of developmental data on sections of a single panel after regidization at 1533°K (2300°F) and also after a subsequent coating firing cycle at 1644°K (2500°F) in a sealed saggar. The data show essentially no strength or strain degradation in either plane as a result of firing panels in a sealed enclosure. It has been hypothesized that the rate of loss of the grain-growth inhibitors (B_2O_3, P_2O_5) from the fiber has been reduced (or eliminated) as a result of this firing cycle modification. This coating process modification was

20

THE LOSS OF ADDITIVES FROM MULLITE FIBERS
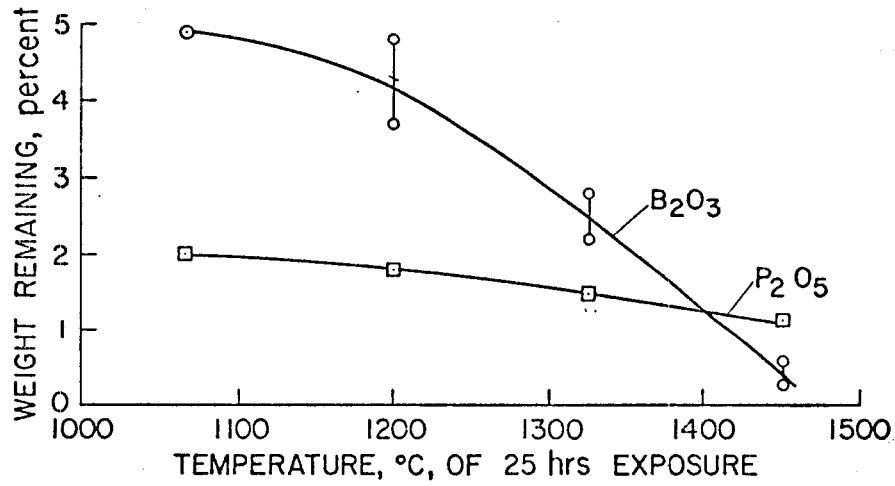
Figure 14. Loss of B_2O_3 and P_2O_5 from Babcock and Wilcox fiber as a function of thermal exposure. (Reference 6)

Table 4. Effect of Coating Firing in Sealed Enclosure on Mechanical Behavior of Basic Insulation.

Thermal History	Strength (kN/m^2)*		Strain (%)*	
	In-Plane	Transverse	In-Plane	Transverse
1 hr/1533°K	404.05	115.84	0.21	0.44
1 hr/1533°K + 1 hr/1644°K in a sealed saggar	421.28	98.60	0.24	0.50

* Average of 3 test points

planned for fabricating program deliverables; however, unavailability of suitable impermeable saggars prevented this procedure from being implemented. Several attempts were made using vitrified alumina saggars; however, saggar thermal stress failures resulted in an unacceptable specimen yield of deliverable hardware. Nevertheless, this process modification has been included in the definition of an optimized RSI base system (Section 4).

21

2.1.5 HEAT TRANSFER ATTENUATION PROCESS DEVELOPMENT

2.1.5.1 Small Diameter Fiber Evaluation

For fibrous insulations, the principal mode of heat transfer at elevated temperatures is by thermal radiation. In general, the radiative contribution can be estimated from an empirical fit of the data with an equation of the form:

$$K_r = CT^m \qquad (1)$$

where C and m are empirical constants determined by experiment.

In order to proceed with a systematic optimization program, it is necessary to define the material variables which effect radiative transfer. Several theoretical models have been proposed which interpret these variables theoretically. For example, Larkin and Churchill (Reference 7) developed the following expression:

$$K_r = \frac{8\ T^3}{A + 2S} \qquad (2)$$

where A is the absorption cross-section of the fibrous insulation and S is the back-scattering cross-section of the fibrous insulation. The coefficients A and S are readily determined experimentally from spectral transmission measurements. Their study identified fiber diameter as a major variable influencing the backscattering cross-section and fiber:void volume opacity as the variable influencing the absorption cross-section. Also, fiber diameter was shown by Strong et.al. (Reference 8) to affect the gaseous component of the total thermal conductivity function, especially in the range of pressures experienced by the Shuttle thermal protection system.

During this phase of the program, an experimental evaluation of the insulation effectiveness of panels fabricated from available small-diameter fibers was conducted as a function of pressure and temperature. Experimental lots of small-diameter B & W fibers, formed by the spinning and blowing processes, were rigidized with the SBA-10 binder and subsequently machined into specimens suitable for thermal conductivity measurement. As-received fiber diameter distributions for these two classes of fibers are compared in Figure 2. In addition, a panel fabricated from the high alumina-silica Carborundum fiber was also included in this study. A typical fiber distribution for the melt-formed high alumina-silica Carborundum fiber is shown in Figure 5.

Table 5 and Figure 15 summarize the thermal conductivity data obtained as a function of pressure and temperature for the three types of small diameter panels. The thermal conductivity functions were found to rank according to the fiber diameter distributions shown in Figures 2 and 5. The theoretical prediction of a reduced thermal conductivity function for small diameter fibers has been verified, especially for the Carborundum fiber where a factor of two reduction in thermal conductivity has been obtained (compared to the B&W panel formed using the spinning process which was of comparable density).

TABLE 5. Thermal Conductivity Data for Small-Diameter Fiber Panels

A. Small Diameter B&W Spun Fiber; ρ = 0.209 g/cc (13.0 pcf)

Temperature		Pressure		Thermal Conductivity	
°K	°F	N/m^2	atm	W/m-°K	BTU/ft-sec-°F
477	400	1.013×10^3	10^{-2}	0.055	0.881×10^{-5}
812	1001	1.013×10^3	10^{-2}	0.090	1.450×10^{-5}
477	400	1.013×10^5	1	0.072	1.150×10^{-5}

B. Small Diameter B&W Blown Fiber, ρ = 0.257 g/cc (16.2 pcf)

Temperature		Pressure		Thermal Conductivity	
°K	°F	N/m^2	atm	W/m-°K	BTU/ft-sec-°F
477	400	1.013×10^3	10^{-2}	0.055	0.890×10^{-5}
811	1000	1.013×10^3	10^{-2}	0.082	1.320×10^{-5}
1144	1600	1.013×10^3	10^{-2}	0.112	1.800×10^{-5}
477	400	1.013×10^5	1	0.078	1.250×10^{-5}

C. Small Diameter Carborundum Melt-formed Fiber, ρ = 0.215 g/cc (13.4 pcf)

Temperature		Pressure		Thermal Conductivity	
°K	°F	N/m^2	atm	W/m-°K	BTU/ft-sec-°F
481	405	1.013×10^3	10^{-2}	0.035	0.555×10^{-5}
814	1006	1.013×10^3	10^{-2}	0.040	0.645×10^{-5}
1033	1400	1.013×10^3	10^{-2}	0.046	0.736×10^{-5}
1144	1600	1.013×10^3	10^{-2}	0.057	0.914×10^{-5}
477	400	1.013×10^5	1	0.057	0.917×10^{-5}
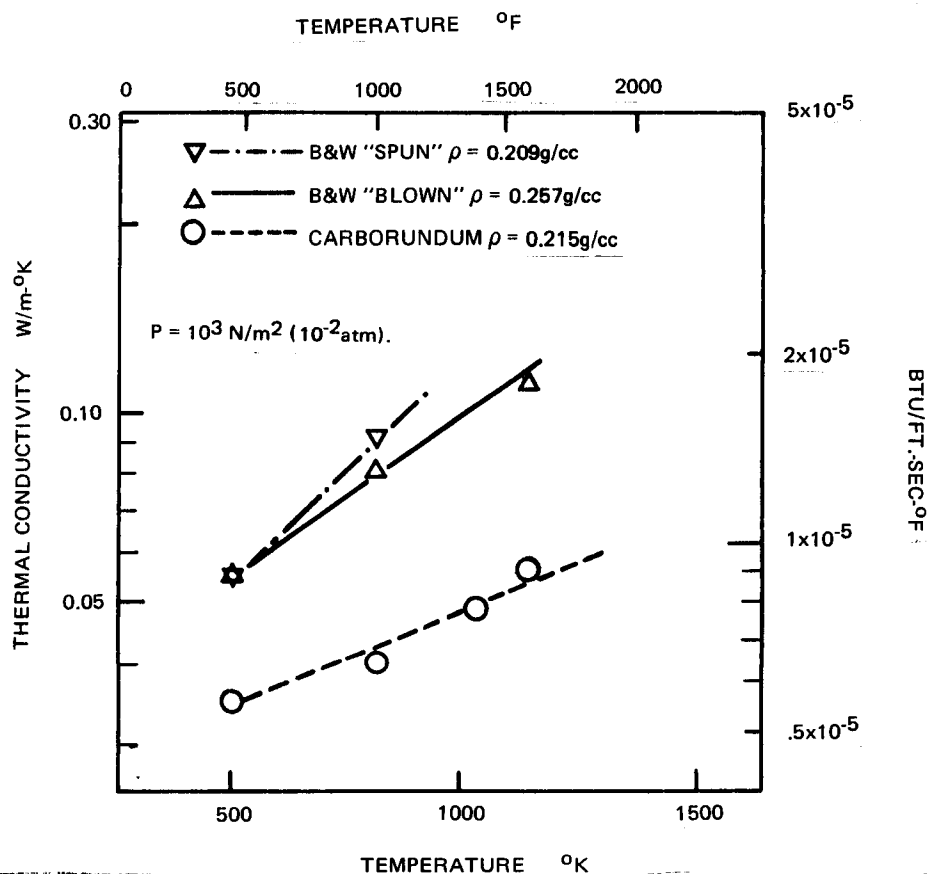
Figure 15. Thermal conductivity of small-diameter fiber panels as a function of pressure and temperature.

The B&W panel formed using the blowing process had a twenty-three percent higher density which may have contributed to its unanticipated higher thermal conductivity level (compared to the Carborundum fiber panel). Also, the B&W fibers formed by the blowing process had a high "shot" content (non-fibrous debris) which could have adversely affected its thermal conductivity function. It should be noted that the Carborundum fiber as processed also contains a high "shot" content and the batting used in this study was processed by the vendor to remove the non-fibrous component.

It is anticipated that panels fabricated from the B&W "blown" fiber with "shot" contents and densities similar to the Carborundum fiber panel would yield similar thermal conductivity functions. The B&W fiber would also have the additional advantages of higher tensile strength and dimensional and phase stability at 1644°K (2500° F). It should be noted that B&W is producing, on an experimental basis, "blown" mullite fibers with the majority of the fibers below 2 μm under a NASA-Lewis Research Center sponsored study (Contract No. NAS 3-16764). At the conclusion of the contract activities, a decision will be made regarding the desirability of process scale-up to achieve higher production quantities.

2.1.5.2 Fiber: Void Opacification

Additional reductions in thermal conductivity can be achieved through the utilization of opacification techniques to attenuate thermal radiation transfer through fibrous insulations.

The development of a novel technique for applying a near-continuous fiber coating of chromia platelets on mullite fibers (shown in Figure 16 (a)) has enabled a direct quantitative assessment of this heat transfer attenuation mechanism to be made. The fiber coating system, evaluated on the Phase 1 portion of this program, is applied by impregnating rigidized panels with a Cr_2O_3 solution. Figure 16 (b) compares the thermal conductivity function for chromia opacified REI-Mullite with that of unopacified REI-Mullite. Above temperatures of 1100° K, a significant reduction in thermal conductivity has been achieved (approaching a factor of 2) at 1644° K (2500° F).

As part of the Phase 2 study, direct spectral transmittance measurements were made on opacified and unopacified REI-Mullite. Figure 16(c) clearly shows that opacification acts as a direct thermal radiation barrier and may be used to effectively deal with the the shine-in component of thermal-radiative heat transfer. Although fiber:void opacification has not been incorporated into the primary Phase 2 deliverables (due to limited data on its effects on basic insulation and surface coating mechanical behavior), its utilization in an operational Shuttle RSI system should result in significant TPS weight reductions. The combined effect of small diameter fibers and fiber:void opacification, when implemented into the REI-Mullite system, should lead to TPS weight reductions approaching a factor of two. This projection is based upon a recently developed TPS

weight correlation parameter, $W_{TPS} = \left(\dfrac{k}{c_p}\right)^{1/2} \rho^{7/8}$, which is described in the

following paragraph.

2.1.5.3 Dependence of Insulation Weight Requirements on Thermal Properties

It has been demonstrated from previous studies (Reference 1) that for typical lifting entry missions where the heat conducted into the insulation is small compared to the heat radiated away from the surface (studies show 97 percent of the incident heat flux is rejected by re-radiation from the surface), the controlling parameter group affecting insulation weight is $(k\rho/c_p)^{1/2}$. More recent parametric studies including the effect of temperature-dependent properties has shown the density-dependence in the above function to be $\rho^{7/8}$ instead of $\rho^{1/2}$. In addition, these studies also indicate that, for preliminary design computations, weight estimates could be made using thermal properties at 811° K (1000° F) and 1.013 kN/m^2 (10^{-2} atm). Table 6 compares the insulation weight parameter for the Mod 1A REI-Mullite system with a candidate RSI-Silica system.

Table 6. Comparison of Insulation Efficiency Parameters for Candidate RSI-Mullite and Silica Systems

RSI System	Density		Weight Efficiency Parameter $\left(\dfrac{k}{c_p}\right)^{1/2} \rho^{7/8}$	
	kg/m^3	lb/ft^3	$\left(\dfrac{lb}{ft\text{-}sec\text{-}°R}\right)^{1/2}$	$\left(\dfrac{lb}{ft^3}\right)^{7/8}$
Mod 1A REI-Mullite	192.24	12.0	0.576	
RSI-Silica	240.30	15.0	0.570	
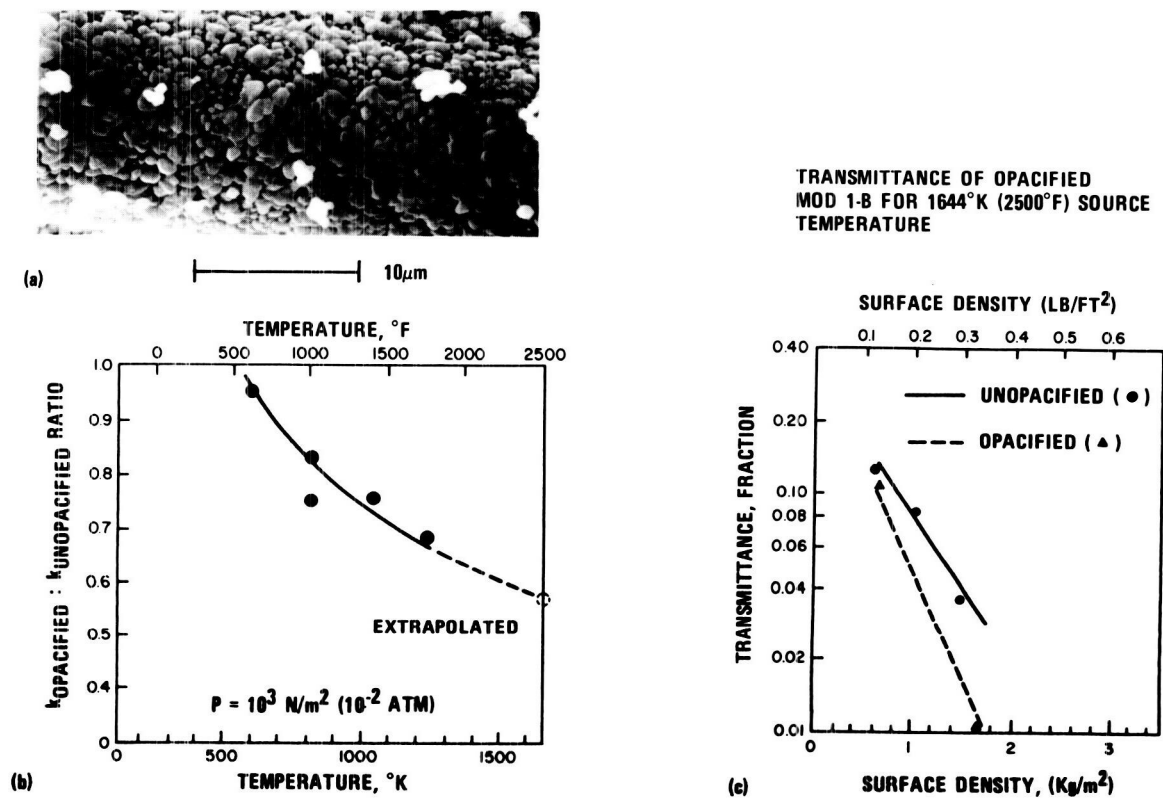
Figure 16.   Effect of Cr_2O_3 fiber:void opacification on thermal conductivity.

Of significance is the prediction that the Mod 1A REI-Mullite system is comparable to a 240.30 kg/m^3 (15.0 lb/ft^3) RSI-Silica system. This latter prediction has recently been confirmed by arc-test data from NASA-Ames Research Center which included the effects of bond-soak out after heating termination, an effect which is also included in the weight-efficiency correlation parameter. Table 7 is a reprint of the pertinent data which appeared in the OAST April 1972 Monthly Report which clearly shows that a 192.24 kg/m^3 (12.0 pcf) REI-Mullite system and a 240.3 kg/m^3 (15.0 pcf) RSI-Silica system are of equal insulation efficiency (within ±10%) when evaluated under conditions of comparable specific weight and complete re-entry simulated heating (including soak-out effects). Since small-diameter mullite fibers (1-2 μ m) have yet to be incorporated into the REI-Mullite system, it is projected that its thermal insulation efficiency will exceed that of a 240.3 kg/m^3 (15 lb/ft^3) RSI-Silica panel. This improvement is based on a projected reduced thermal conductivity function (Figure 15) which is anticipated for small-diameter fibers.

26

Table 7. Summary of Plasma-Arc/Radiant Preheater Test Results for RSI Material Candidates (Reference 9)

Material	Test Cycles	Specimen Density		Specimen Thickness		Stagnation Heating Rate		Surface Temperature		Backwall Temperature	
		kg/m^3	pcf	cm	in.	W/cm^2	BTU/ft^2-sec	°K	°F	°K	°F
LI 1542	12	240.30	15	3.81	1.500	33.9	30	1433	2120	336	145
REI Mod 1A	5	240.30	12	3.81	1.500	27.1	24	1413	2083	377	220
REI Mod 1A	1	192.24	12	4.76	1.875	33.9	30	1455	2160	344	159

SECTION 3

SURFACE COATING DEVELOPMENT

3.1 PROCESS IMPROVEMENT AND PROPERTIES OPTIMIZATION

3.1.1 INTRODUCTION

The primary objective of this portion of the program was to identify and evaluate processes for improving the mechanical and thermal performance of the REI-Mullite surface coating. The approaches evaluated included process improvements associated with the SR-2 coating developed on the original program and the development of new coating systems compatible with an optimized basic insulation. For both approaches, techniques for tailoring the thermal radiative properties to meet the combined orbital and entry requirements with a completely reusable coating were developed. The work accomplished on each of these is described in the following subsections.

3.1.2 MODIFICATIONS OF THE SR-2 COATING SYSTEM

The SR-2 coating system (developed on the initial phase of this contract) consists of the following constituents:

X • Basic Oxides	Y • Neutral Oxides	Z • Acid Oxides
0.180 Li_2O 0.027 Ca O 0.186 Mg O 0.104 NiO	1.000 Al_2O_3	2.700 SiO_2

Note: X, Y, Z are the oxide weight: molecular weight ratios

During the course of subsystem evaluation testing, several problem areas were identified with the SR-2 coating system. These included: (1) the tendency of the NiO pigment to change oxidation state in simulated entry heating tests, (2) its marginal resistance to cracking in simulated entry heating tests, (3) the tendency to develop pinholes during processing, (4) the development of a rippled surface texture due to solution reactions at the surface coating: basic insulation interface, and (5) the inability of the SR-2 coating to meet the NR/SD orbital solar absorptance: emittance ratio requirement of 0.40. Exploratory materials

development studies (described in the following subsections) were initiated on this program with the goal of eliminating these problems.

3.1.2.1 Surface Densification

The machined surface of porous REI-Mullite must be densified before an acceptable coating can be applied. The densifying procedure previously developed consisted of the SR-2 formulation with the emittance enhancer (NiO) removed and the glass frit (P-941) reduced by 1/3. This densifier (XSR2) was compatible with both the REI and the coating. The oxide formulation for XSR2 is:

$$.157 \ Li_2O$$
$$.018 \ CaO \qquad 1.00 \ Al_2O_3 \qquad 2.56 \ SiO_2$$
$$.126 \ MgO$$

The application procedure for XSR2 was to brush the composition into and on the REI to a dry weight of $0.754 \ kg/m^2$. After drying, the densified sample was heated to $755°K$ ($900°F$) to burn out the temporary binder (PVA). The excess loose surface material was removed by brushing until the densifier weight was $0.259-0.431$ kg/m^2. This densifier worked well but the application procedure described above produced a wide variation in densifier weight and thickness which resulted in a variation in overall coating thickness. Studies were directed toward optimizing the densifier application procedure. The results of this evaluation are listed in Table 8.

Table 8

Densification Procedures and Results

Densifier Weight (kg/m²)	Temperature Treatment	Results
0.431	755°K (900°F)	Insufficient densifier after removal of loose surface material
0.754	755°K (900°F)	Wide scatter in densifier weight.
0.754	922°K (1200°F)	Wide scatter in densifier weight
0.754	1225°K (1800°F)	Some adherence – densifier too heavy.
0.431	1366°K (2000°F)	Some flaking of densifier – densifier too heavy (lower weight yielded improved performance).
0.431	1644°K (2500°F)	Some glazing of surface, covercoat SR-2 tended to "crawl"

30

The optimum densifying procedure developed which controls total coating weight and coating thickness, minimizes crawling of the coating, and produces a well-bonded coating was found to be the XSR-2, applied at 0.269-0.323 kg/m^2 and fired to 1366°K (2000°F). This densifier modification was incorporated into program deliverables.

3.1.2.2 Composition Adjustments to Eliminate Pinholes

One of the problems associated with the SR-2 coating was the development of pin-holes in the coating during the firing cycle. These pinholes have been attributed to one or more of the following phenomena: (1) entrapped gases, (2) decomposition of some constituents in the coating mixture, (3) outgassing of the REI and/or (4) lack of coating fluidity to heal minor flaws at the maximum firing temperature used. Several approaches were studied to reduce "pinholing". These were: (1) adjust-ment of composition to increase fluidity of the coating at 1644°K (2500°F), (2) firing the coating in vacuum, and (3) removal of NiO.

Calcium oxide (CaO) is known to increase the fluidity of certain glasses at high temperature (Reference 10). In an effort to reduce the pinhole development in the SR-2 coating, a small amount of CaO was added to the SR-2 formulation and this coating was applied to a densified REI tile and fired to 1644°K (2500°F). The coat-ing severely attacked the REI. Smaller amounts of CaO may have caused less attack, but it was obvious from this result that a more fluid coating of this general composition was not the proper direction to investigate for reducing pinholes.

Several SR-2 type coatings were fired in vacuum in an effort to eliminate entrapped gases introduced during the mixing and spraying operation. In all cases, the coatings fired in this manner had a pebbly surface. Examination of these speci-mens indicated that the coating began to glaze before some decomposition gases and/or entrapped gases could escape.

Pinholes were finally eliminated when the NiO was removed from the composition. Pinholes are, therefore, believed to be caused by reduction of the NiO with resul-tant loss of oxygen at a temperature where the coating is viscous but not fluid enough to heal.

Figure 17 is an SEM photograph showing an SR-2 coated REI tile and another REI coated tile with a coating which does not contain nickel oxide. The SR-2 coating with the nickel oxide pigment shows a number of gas pockets or voids whereas the other coating, which is identical except that the NiO was replaced with HfO_2, is free of voids. This photograph is typical of results obtained on numerous samples. Thus, the pinhole problem associated with the SR-2 coating was essentially eli-minated when nickel oxide was removed from the formulation.

31

NiO PIGMENT

SURFACE COATING

Hf O$_2$ PIGMENT

RIGIDIZED MULLITE FIBER INSULATION

100 μ m

100 μ m
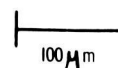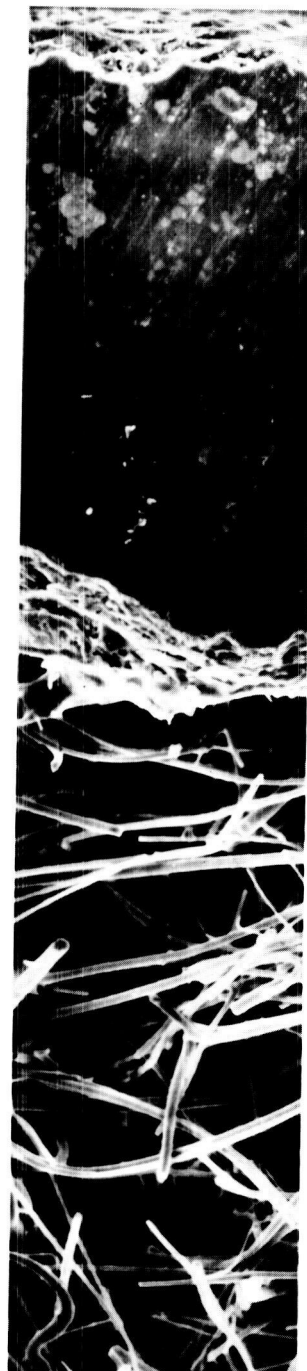
Figure 17. SEM photographs of an SR-2 coating (NiO pigment) and a modified coating with no NiO. Notice the voids in the SR-2 coating and no voids in the modified coating.

3.1.2.3 Effect of Firing Schedule on SR-Series Glass-Phase Morphology

The glass phase of the SR-2 coating (which is a quaternary SiO_2-Al_2O_3-MgO-CaO glass designated P-941) was exposed to a variety of heat-treatment schedules to determine which crystalline phases would develop and how sensitive this glass was to firing and/or heating-cooling cycles. Table 9 summarizes the heat treatment schedules followed. Figures 18 and 19 summarize the results of the study both visually and by x-ray diffraction analyses for specimens which were air quenched. Good correlation was obtained between the visual appearances of a crystalline phase and that detected by XRD.

Table 9

Firing Schedule – P941 Glass Firing Study

Sample	Heat Treatment Temperature °K (°F)	Time hr.	Additional Heat Treatment Temperature °K (°F)	Time hr.	Cooling Conditions
A	1644 (2500)	1	None	4	Air Quench
B	1644 (2500)	1	1561 (2350)	4	Air Quench
C	1644 (2500)	1	1561 (2350)	4	Furnace Cooled
D	1644 (2500)	1	1477 (2200)	4	Air Quench
E	1644 (2500)	1	1477 (2200)	4	Furnace Cooled
F	1644 (2500)	1	1366 (2000)	4	Air Quench
G	1644 (2500)	1	1366 (2000)	4	Furnace Cooled

X-ray diffraction (XRD) analyses of the specimens indicated that as the additional heat-treatment temperature was decreased crystallization within the glass was initiated. XRD patterns obtained for samples A, B and C indicated that these materials were noncrystalline, i.e., no sharp diffraction peaks - only a very broad diffraction band at the low 2θ diffraction angles. Samples D and E indicated the presence of a crystalline compound (a few sharp diffraction peaks) in addition to some noncrystalline material. Samples F and G indicated a high concentration of crystalline material in addition to a minor noncrystalline phase. The crystalline component, which was first observed at low concentrations in samples D and E and at higher concentrations in samples F and G, has been identified as cordierite ($2MgO \cdot 2\ Al_2O_3 \cdot 5\ SiO_2$). In addition, a very weak phase of $MgSiO_3$ (pyroxene) may also be present.

33
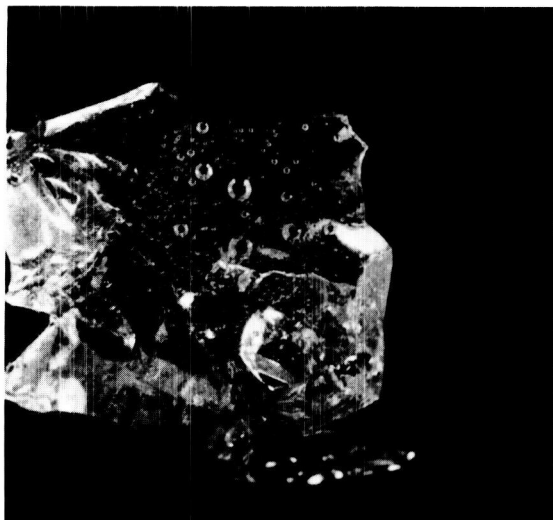
Sample A
1 Hr. @ 1644° K (2500° F)
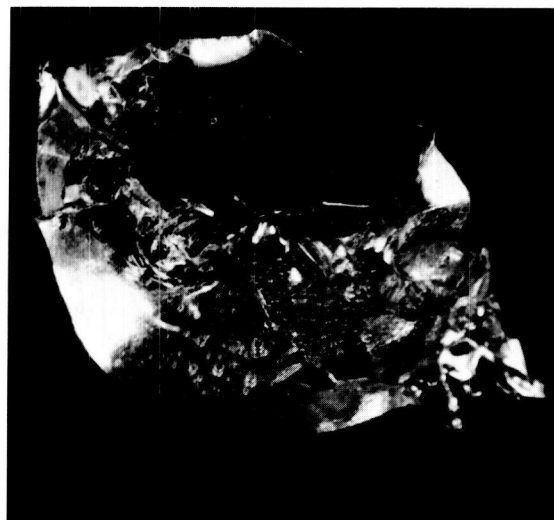
Sample B
1 Hr. @ 1644° K (2500° F) Plus
4 Hrs. @ 1561° K (2350° F)
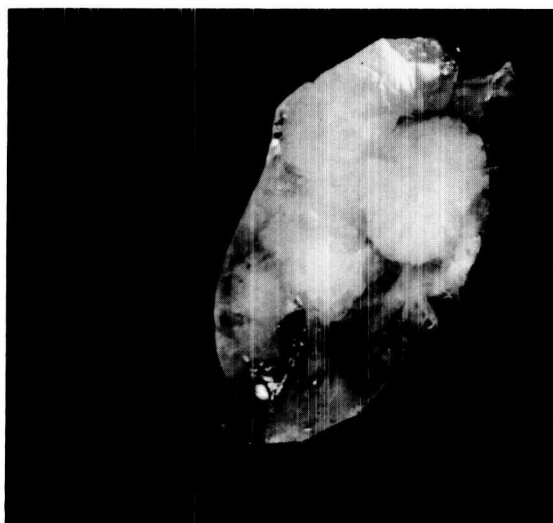
Sample D
1 Hr. @ 1644° K (2500° F) Plus
4 Hrs. @ 1477° K (2200° F)
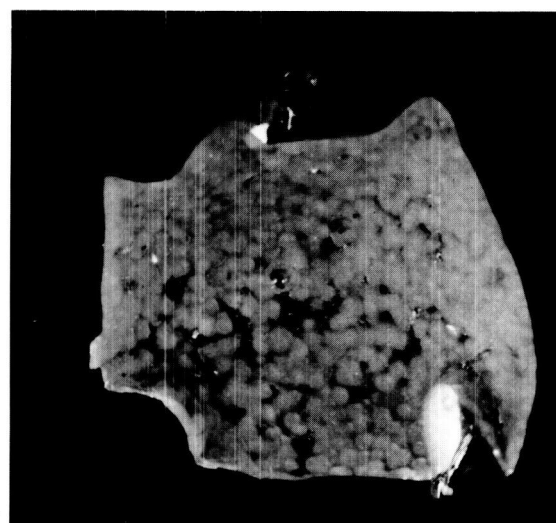
Sample F
1 Hr. @ 1644° K (2500° F) Plus
4 Hrs. @ 1366° K (2000° F)

Figure 18. Photographs of P-941 glass after various heat treatments. No visible crystalline phase was developed at 1644°K or 1561°K. The 1477°K soak produced a few large crystals while a hold at 1366°K produced many small crystals. The crystal phase was identified by XRD as α-cordierite ($Mg_2Al_4Si_5O_{18}$).

XRD SAMPLE "A"
1 HR. @ 1644°K (2500°F)

XRD OF SAMPLE "B" (P941 GLASS)
1 HR. @ 1644°K (2500°F) PLUS 4 HRS.
@ 1640°K (2350°F)
(AIR QUENCH)

XRD SAMPLE "D" (P941 GLASS)
1 HR. @ 1644°K (2500°F) PLUS 4 HRS.
@ 1477°K (2200°F)

XRD SAMPLE "F" (P941 GLASS)
1 HR. @ 1644°K (2500°F) PLUS 4 HRS.
@ 1366°K (2000°F)

2θ

2θ

2θ

2θ
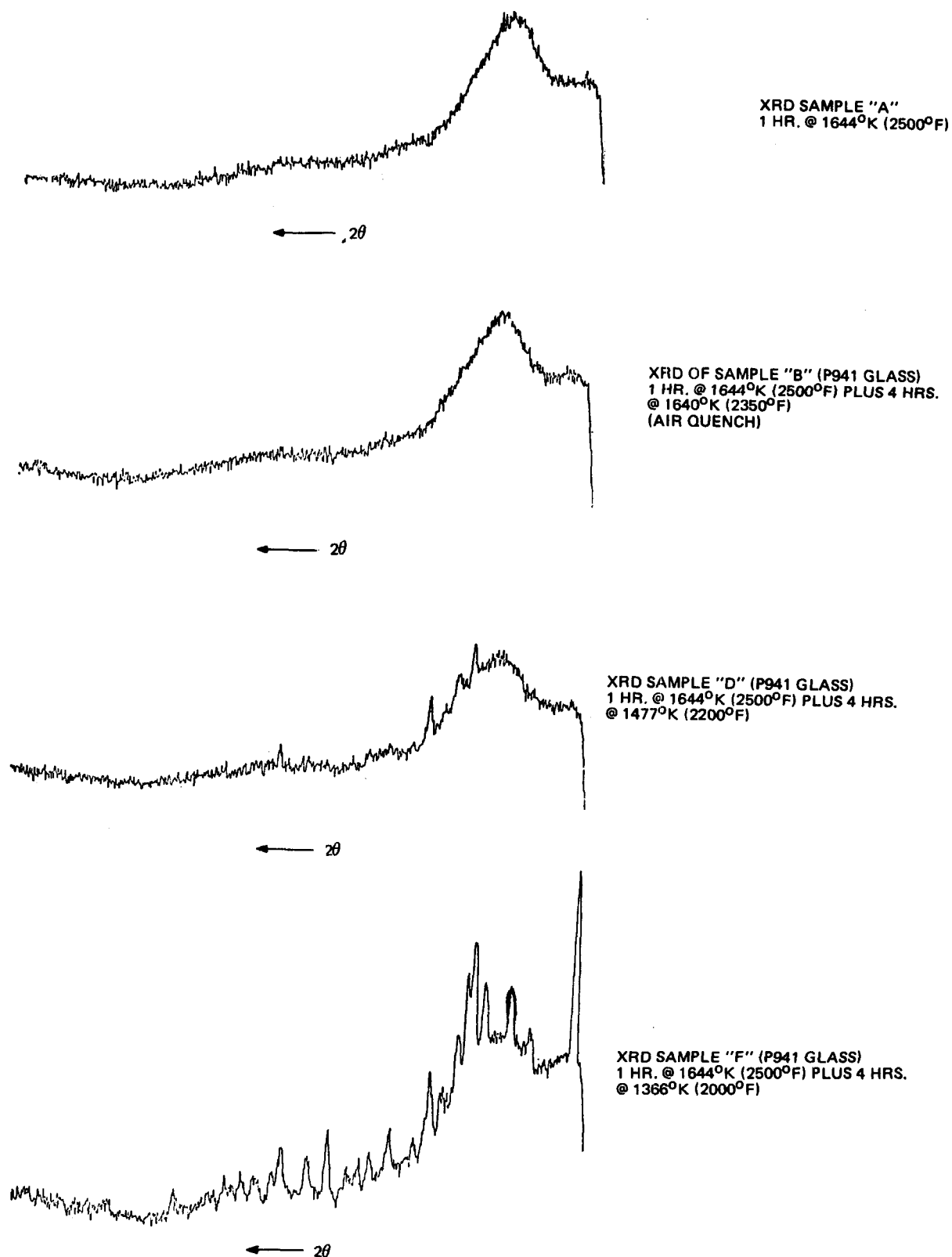
Figure 19. Comparison of XRD patterns for P941 glass as a
function of heat treatment schedule

35

Since a composite of microcrystals in a glass matrix (obtained by devitrifying glass) may have many advantages (or disadvantages) depending upon the topology of the two phases, a study (described in the next section) was conducted to determine whether the presence of the α-cordierite phase in the P941 glass matrix would act as a strengthening mechanism for the SR-2 coating.

3.1.2.4 Strength and Strain Improvements in SR-Series Coatings

A series of programs were conducted to increase the strength and strain capability of the SR-series coatings. Approaches taken included: (1) nucleation of the α-cordierite from the glass phase, (2) variations in coating thickness and glass content and (3) preparation of coating samples by conventional cold-pressing and sintering to establish the upper bound for achievable strength and strain capability with the SR-series coatings. The latter two approaches were conducted on a concurrent GE-RESD sponsored program and are reported for completeness.

The first approach was an attempt to improve the strength by converting the glass portion of the coating to a high-strength crystalline phase. The coating employed in this effort was SR2-HF1C. SR2-HF1C is similar to the standard coating (SR-2) except the emittance enhancer was changed from ($\sim$ 3 w/o) nickel oxide to 20 w/o HfO_2. In addition, the glass content was increased to compensate for the additional refractory material (HfO_2) and to maintain total glass content at 16.1 w/o. This coating was developed for firing at 1644°K (2500°F) and, after firing, to be impervious and free of flaws. As reported previously, the replacement of NiO with HfO_2 reduced the tendency to develop pinholes in the coating and also decreased solar absorptance to an acceptable level. Figure 20 is an SEM photograph showing this coating fired on an REI-Mullite tile.

Samples of REI-Mullite were coated with SR2-HF1C to determine the effects of firing cycle on mechanical properties. The firing cycles used were similar to those used to nucleate a stable cordierite phase from the glass frit as discussed in section 3.1.2.3. The procedure used for preparing these samples is described in Table 10. A summary of the test data is given in Table 11. Coating strain data was obtained from strain gages placed directly on the coating surface. This data was also used to compute the elastic tensile moduli. It should be noted that the ultimate tensile strength data represent minimum values. The post-fabrication heat treatments did not impart the strength and strain-capability improvements anticipated from the formation of microcrystals in the P941 glass matrix. Since the achievement of improved strength by glass-ceramic processing is critically dependent upon the topology of the dispersed crystalline phase, it appears that additional research regarding identification of an optimum post-fabrication heat treatment cycle will be required to fully exploit this strengthening approach.

36

HFIC COATING
NOTICE COATING IS FREE OF VOIDS.

COATING INTERFACE
NOTICE GOOD WETTING OF MULLITE FIBERS BY COATING.
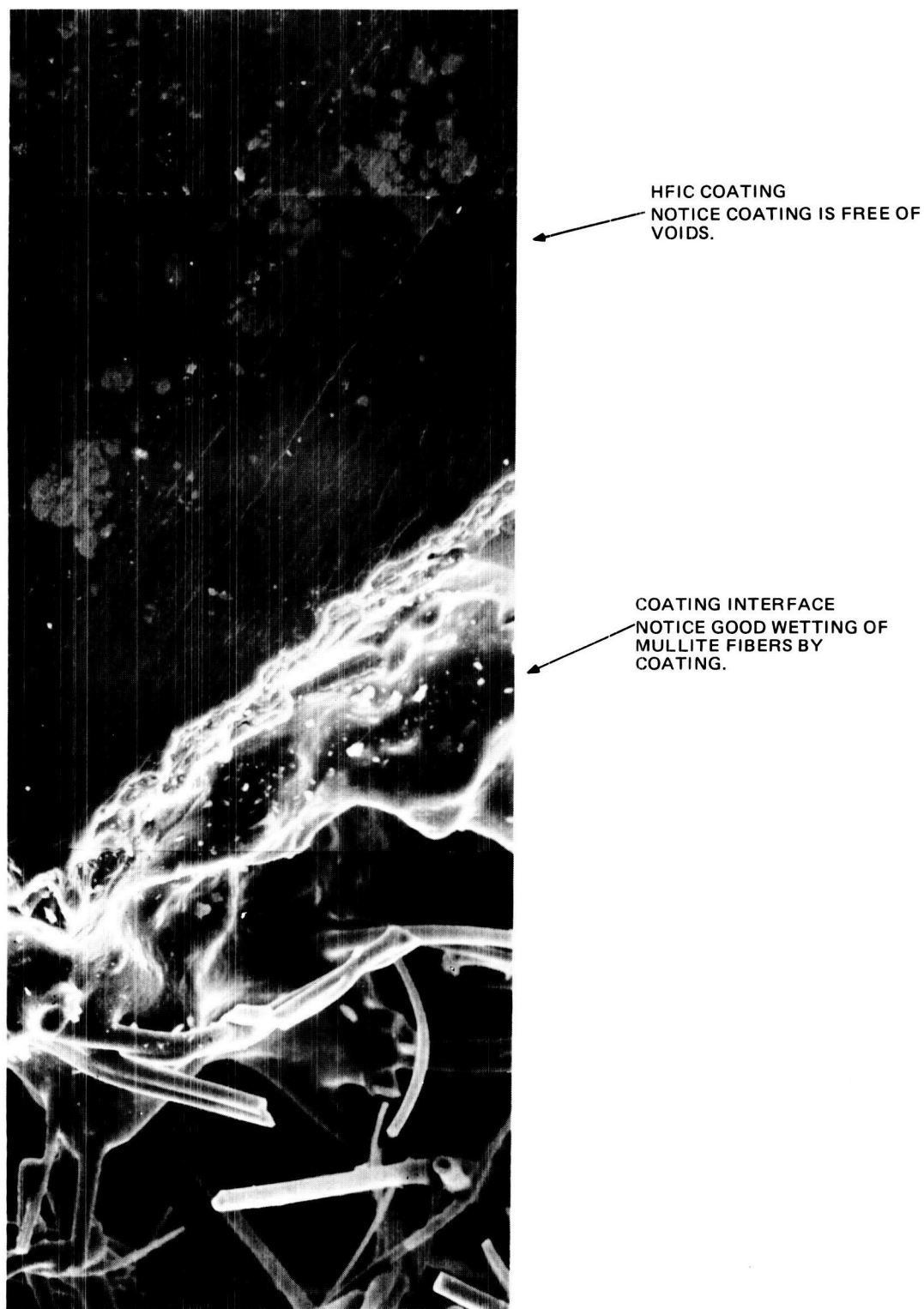
Figure 20. SEM photograph of SR2-HFIC Coating on REI-Mullite. Coating fired to 1644°K (2500°F) (Mag. 300X)

Table 10

Procedure for Preparation and Evaluation of Coating
Mechanical Behavior Specimens

Process Step	Description
A.	Panels 12.70 x22.86x1.27 cm (5x9x1/2 in) were densified on top and bottom surfaces (12.70x22.86 cm) with XSR 2 and fired to 755°K (900°F).
B.	Panels were coated on top and bottom surfaces with SR2-HF1C and fired to 1255°K (1800°F). After this firing strips 2.54x22.86 cm (1x9 in) were machined from the panels.
C.	Groups of specimens were fired at each of the following conditions: 1. 3 hours to 1644°K (2500°F), held at 1644°K (2500°F) for 1 hour, and furnace cooled. 2. Same as 1. except after the 1644°K (2500°F) hold, the samples were cooled to 1366°K (2000°F) and held 4 hours, and furnace cooled. 3. Same as 1. except after the 1644°K (2500°F) hold, the samples were cooled to 1477°K (2200°F) and held 4 hours, and furnace cooled.
D.	Flexure strength, strain-to-failure, elastic modulus, and failure mode of the three types of specimens were determined.

In addition to this crystallization study an internally-funded program was conducted to determine the effect of coating thickness and glass content on coating strength. In general, it was found that, if the coating thickness was increased about 1/3 to 0.813mm (0.032 in) the coating strength would increase; however, above this thickness, the strength of the coating decreased. The effect of changing the glass content of the coating was not as conclusive. It was found that a decrease for 16 to 11 w/o increased coating strength and an increase for 16 to 23 w/o increased coating strength. To optimize the glass content from a strength standpoint will require development of improved sample preparation and test techniques.

38

Table 11

Mechanical Data Derived From Four Point Bending Of SR2-HFIC Coated REI-Mullite Beams

Test Sample	Firing Cycle	Data Derived at Failure Load							Failure (1)
		REI-Shear Stress		Coating Tensile Stress		Coating Tensile Modulus		Coating Elongation	
		kN/m²	(psi)	MN/m²	(psi)	GN/m²	(10⁶ psi)	(%)	
1-1	1644°K(2500°F)-1 hr.	154.44	22.4	11.45	1660	67.29	9.76	0.0172	S
1-2		166.85	24.2	14.45	2110	57.16	8.29	0.0254	C
1-3		159.27	23.1	13.86	2010	84.46	12.25	0.0168	S/C
1-4		157.20	22.8	12.07	1750	58.40	8.47	0.0209	S/C
2-1	1644°K(2500°F)-1 hr. plus 1366°K(2000°F)-4 hr.	98.60	14.3	8.21	1190	46.26	6.71	0.0181	T
2-2		140.65	20.4	10.82	1570	58.05	8.42	0.0196	C
2-3		95.84	13.9	6.72	975	35.09	5.09	0.0212	T
2-4		72.40	10.5	6.41	930	54.88	7.96	0.0116	T
3-1	1644°K(2500°F)-1 hr. plus 1477°K(2200°F)-4 hr.	151.69	22.0	12.89	1870	61.09	8.86	0.0212	S
3-2		139.96	20.3	10.41	1510	46.47	6.74	0.0220	S
3-3		146.86	21.3	12.48	1810	60.40	8.76	0.0204	C
3-4		84.12	12.2	6.83	990	50.54	7.33	0.0137	C

Specimen Geometry: 22.86x2.54x1.27 cm (9x1x1/2 in)
                     Coating thickness - 0.6096 mm (0.024 in)

Test Set-Up: Support span - 20.32 cm (8 in), load span - 10.16 cm (4 in)

(1) T = tensile failure in constant moment section
     S = shear failure near support
     C = local compression failure at support

To establish the upper strength limit attainable with this coating, a bar of SR2-HFIC formulation was pressed at 10,000 psi and subsequently fired for 1 hour at 1533°K (2300°F). This bar was strained-gauged and loaded to failure in a flexure mode. A comparison of this test with the average values of SR2-HFIC coating previously measured is shown in Table 12.

Table 12

Comparison of the Mechanical Behavior of SR-2 HF1C Coating As-fabricated on an REI-Mullite Surface and As-prepared by a Conventional Cold-Pressing and Sintering Technique

Sample Description	Flexure Strength		Bending Modulus		Strain-to-Failure (%)
	MN/m^2	psi	GN/m^2	$psi \cdot 10^{-6}$	
SR-2 HF1-C As-fabricated on REI-Mullite	12.96	1880	6.48	9.4	0.020
SR-2 HF1-C As-prepared by Conventional Cold-pressing and Sintering Technique	38.54	5590	7.03	10.2	0.056

The results of this test illustrate that the SR2-HF1C coating can be optimized to obtain strengths approaching 5000-6000 psi and strain-to-failures approaching 0.06%. The optimization required would be to develop application techniques which would produce a somewhat denser coating than is obtained using present procedures. Particle size distribution of initial coating constituents and firing procedures appear to be the most promising areas for investigation.

3.1.2.5 Coating Reinforcement

The SR2-HFIC coating was also used to produce a coating which was reinforced with platinum mesh. The platinum mesh available for this effort was not uniform in spacing but was used to determine if wetting of the platinum could be achieved with this type of coating. A 12.7x12.7x5.1 cm (5 x 5 x 2 in) sample was prepared by densifying the REI in the standard manner using XSR2. After firing to 755°K (900°F), a thin coat of SR2-HFIC was applied to the top surface of the specimen and then a "fire-polished" platinum mesh screen was placed over the wet SR2-HFIC and an additional coating was sprayed over the mesh to embed the mesh in

the coating. This sample was then fired to 1644°K (2500°F) for 1 hour and good wetting between the platinum and the SR2-HF1C was achieved. (See Figure 21). Process feasibility having been established a uniform platinum mesh was ordered to determine if strength and impact resistance of this type of reinforced coating would have superior properties and performance as compared to the standard coating. Unfortunately, the mesh was not received in time to prepare the test samples for this program. Further efforts directed towards this approach appear warranted.

In addition to the Pt-mesh reinforcement a technique was developed for aligning mullite fibers in the coating. The procedure developed is described below:

Fibers are mixed in a solution of alginic acid, ammonia and hydrochloric acid which suspends the fibers in a viscous medium. The fiber suspension can then be either brushed or extruded onto a tile surface where they will align due to the laminar flow from the brush or extruder. Subsequent drying will hold the fibers in an organic matrix until the tile is fired. This procedure was successfully used for producing a coating with aligned mullite fiber reinforcements. Impact data from these coatings has not shown any improvement over a non-reinforced coating, however, further optimization of this approach appears warranted. Variables to be evaluated should include: fiber diameter, length, type, and volume fraction.

3.1.2.6 Studies to Improve Homogeneity, Texture and Purity

1. Fritting Portions of Coating

Another approach taken to improve the SR-2 type coating was to frit all or portions of the coating to improve homogenity and to assure more predictable melting and flow characteristics. Several compositions were investigated by this method. The first frit was made by melting the glass, NiO and petalite (BASR-2) at 1755°K (2700°F) for 4 hours. This mixture melted to form a viscous glass which could be poured. An REI sample coated with 60% of this frit plus 40% calcined kyanite, when fired to 1644°K (2500°F), developed small shrinkage cracks, had an uneven color and was not water repellent. Another frit (BASR-6) was similar except the P-941 glass was replaced with a high zinc oxide glass (P-1P32). An REI sample was coated with 60% of this frit plus 40% calcined kyanite and fired to 1644°K (2500°F). This sample had large shrinkage cracks and the glass frit tended to ball-up and not wet the kyanite. The coating was not waterproof.

Two other batches were fritted. These both had similar oxide formulations (SR-2) but one was formulated from pure chemicals and the other from the minerals kyanite and petalite plus P-941 glass. These glasses

41
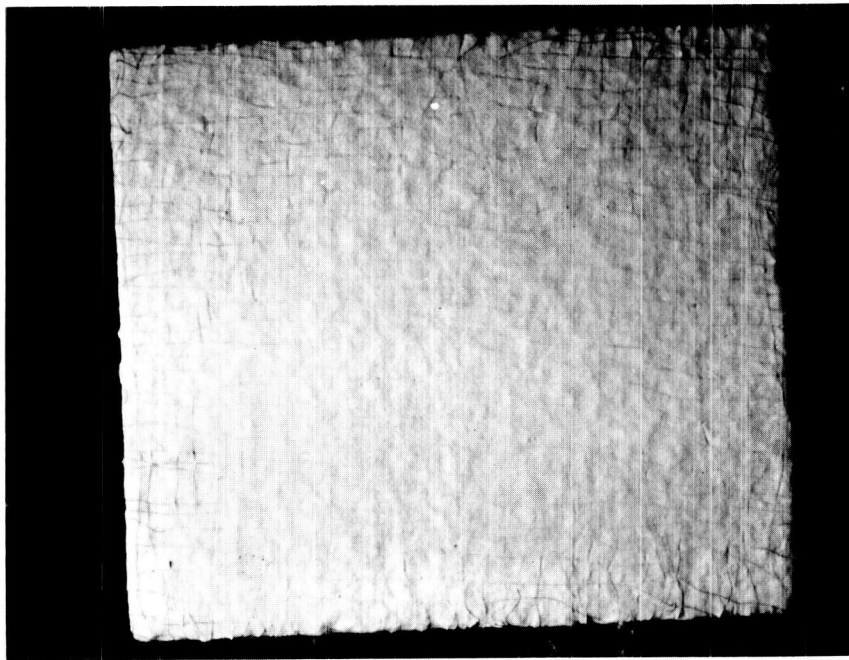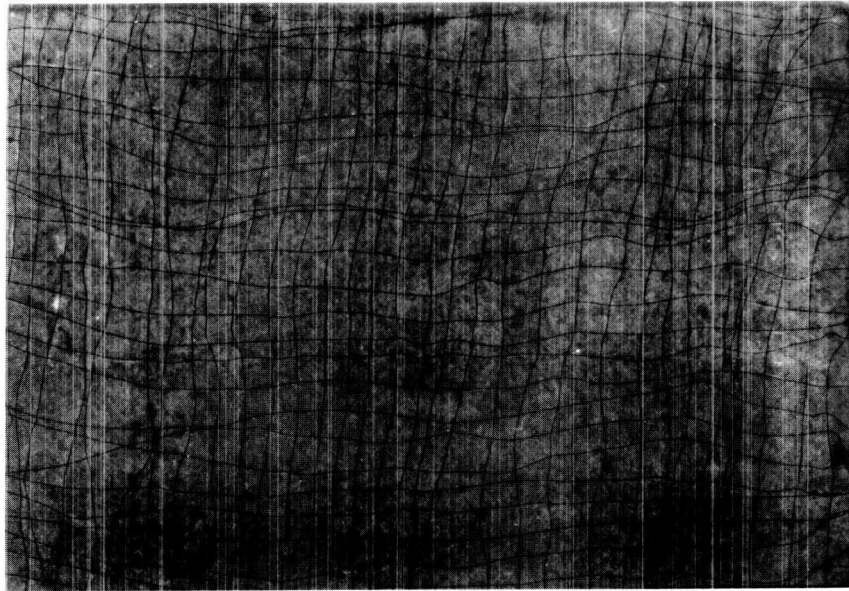
Radiographic Positive (Mag. IX)

Photograph (Mag 0.5X)

Figure 21. Sample of SR2-HFIC coating on REI-Mullite tile reinforced with platinum mesh

were melted at 1839°K (2850°F)*. Both the pure oxide frit (1991-O) and the frit made from minerals (1991-M) were mixed with 50 w/o of standard SR2 and then applied to densified REI and fired to 1644°K (2500°F). The sample coated wtih 1991-O had a green, speckled appearance, some pinholes and some shrinkage cracks. The sample coated with 1991-M was more glassy and was full of pinholes and shrinkage cracks. These results are summarized on Table 13.

The fritting of a major amount of the coating system did not result in improved coatings. This approach may be beneficial but will require additional work to develop the proper parameters needed to produce a good coating. Fritting also appears to cause a major change in the thermal expansion characteristics as would be expected and compositional adjustments will be required.

2. Modified P-941 Glass Frit

The P-941 glass frit contains 3.3 w/o CaO which is a very active flux at elevated temperatures. It is postulated that the rough, uneven surface of REI tiles coated with the SR2 coating system (XSR2 + SR2) results from the CaO attack on the REI. Earlier studies had confirmed that adding small amounts of CaO to the coating greatly increases the attack on REI. In addition, it is believed that a β-quartz solid solution could possibly be formed from the P-941 glass. The β-quartz solid solution has a highly anisotropic crystalline thermal expansion and thus may cause serious degradation to the coating during thermal cycling. Studies were conducted to modify P-941 glass by replacing the CaO with a less reactive flux and by adding Al_2O_3 and SiO_2 in proportions that would move the principal equilibrium phase away from β-quartz solid solution regime.

The first series of modified P-941 consisted of replacing the CaO with ZnO, B_2O_3 and combinations of these oxides. Table 14 lists the compositions evaluated. None of these compositions melted sufficiently to permit fritting of these glasses. Another series of less refractory glass compositions were formulated and melted. These compositions (listed in Table 15) were melted at 1727°K (2650°F) for one hour and fritted by pouring the melted glass into water. All compositions listed are formulated to replace the CaO with fluxes which would not attack REI but would produce a glass with a thermal expansion similar to P-941 frit.

---

*Formulation and fritting was accomplished at the GE Corporate Research and Development Center.

43

Table 13

Summary – Fritted Composition Experiments

Sample	Frit No	Frit Composition	Batch Composition	Results
1	BASR-2	Petalite + P-941 + NiO	Frit + Calcined Kyanite	Small shrinkage cracks, uneven color, refractory
2	BASR-6	Petalite + P-1P32 + NiO	Frit + Calcined Kyanite	Larger shrinkage cracks, frit tended to form balls of glass, uneven color
3	1991-O	SR-2 made with pure chemicals	50% Frit + 50% SR-2	Green speckled, pinholes, some shrinkage cracks
4	1991-M	SR-2 made from mineral constituents	50% Frit + 50% SR-2	More glassy than sample 3, green speckled, no shrinkage cracks, no pinholes, large grains

Table 14

Modified P-941 Glass Composition - Series I

Sample	Composition (Moles)						Results
	CaO	MgO	ZnO	Al_2O_3	B_2O_3	SiO_2	
MGZ-1	–	.87	.13	.42	–	2.21	Glass would not pour @ 1700°K (2600°F)
MGB-1	–	.87	–	.42	.13	2.21	Glass would not pour @ 1700°K (2600°F)
MGZB-1	–	.87	.065	.42	.065	2.21	Glass would not pour @ 1700°K (2600°F)
P-941	.13	.87	–	.42	–	2.21	—

Table 15

Modified P-941 Glass Compositions - Series II

Sample	Composition (Moles)							Results after Melting at 1727°K (2650°F)
	CaO	MgO	ZnO	SrO	Al_2O_3	B_2O_3	SiO_2	
P-941	.13	.87	–	–	.42	–	2.21	
MG-4	–	.87	.13	–	.42	.10	2.21	Very fluid, fritted well
MG-5	–	.87	.13	–	.21	.21	2.21	Fritted well
MG-6	.04	.87	.09	–	.32	.10	2.21	Fritted well
MG-7	–	.87	.09	.04	.32	.10	2.21	More viscous, fritted
MG-8	–	.87	–	.13	.32	.10	2.21	Viscous, poor fritting

Buttons of these glasses were prepared by cold pressing powders into discs at 34.48 MN/m^2 (500 psi). These buttons were placed on a mullite refractory slab which was placed in a furnace at a 45° tilt. The buttons were fired to 1644°K (2500°F) for 60 minutes. The results are shown in Figure 22. Notice in this photograph that the P-941 glass flow was "sucked" into the mullite slab. For comparison, a button of a commercial borosilicate glass (Corning's 7740) was also included in this experiment. Notice this glass flowed but did not penetrate into the mullite to any great degree. The other modified glasses also melted and flowed but did not penetrate into the mullite. The glasses with the ZnO replacements for CaO were the most refractory. The glasses with the SrO were the most fluid in this experiment.

Unfortunately, these studies were made late in the program and no coatings could be made with these modified glasses. However, this study indicated that the coating could be probably improved by substituting a modified glass for the current glass frit used. These modified glasses would appear to have a much better probability of maintaining water repellancy through numerous heating/cooling cycles. In addition, it appears that the modified glass would also reduce attack on the REI and, thus, would improve coating smoothness and coating thickness uniformity. It appears warranted to continue studies in this area to establish phase stability, coating mechanical properties and coating performance.
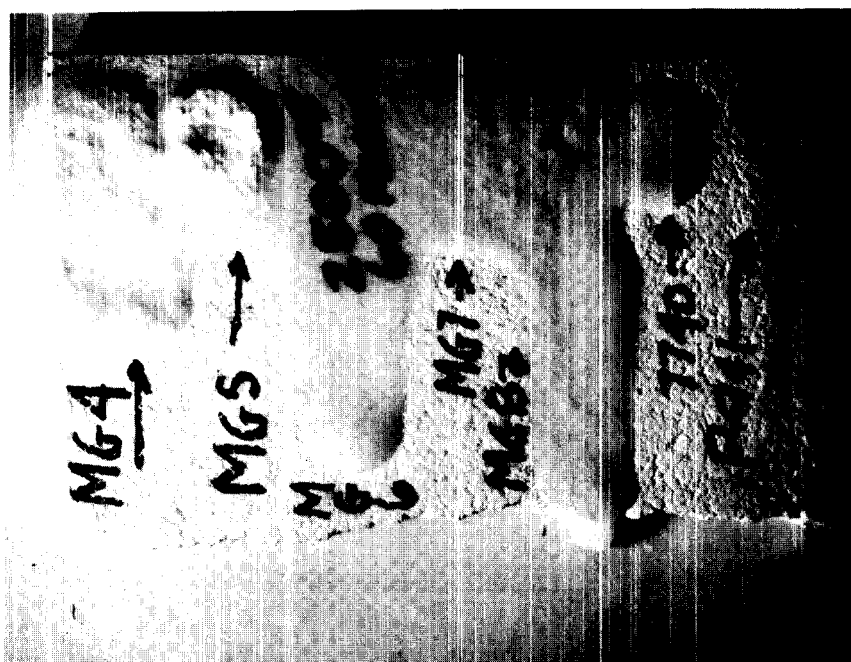

Figure 22. Results of modified P-941 glasses fired to 1644°K (2500°F) for 1 hour. Notice P-941 "sucked" into mullite slab while modified glasses did not.

3. Synthetic Minerals

Another approach investigated for improving the SR-2 coating was to substitute purer materials for the minerals kyanite and petalite. These minerals contain some impurities which could lead to variations in coating lots. Also, the maintenance of optical properties is critically dependent upon consistent control of impurity level.

The first series of materials investigated consisted of substituting reagent chemicals for the minerals and glass frit used in the SR-2 coating. Table 16 lists the compositions of the first series of coatings evaluated. These compositions produced a coating with a lower solar absorption than could be obtained with an SR-2 coating without NiO but in general were too refractory and did not appear satisfactory as a coating for REI-Mullite.

A second approach was to attempt to synthesize the kyanite and petalite minerals using pure chemicals and substitute the synthesized materials in an SR-2 coating with the standard glass frit. Four samples of petalite and nine samples of kyanite were formulated and calcined (Table 17). X-ray diffraction data (Table 18) for synthesized kyanite samples SK-1, SK-2, SK-3 and SK-4 were determined after the material had been calcined at 1922°K (3000° F). XRD results showed that this treatment did not synthesize significant amounts of mullite, but rather α-alumina and cristobalite. Therefore, it was decided to use a more reactive source of alumina, $Al(OH)_3$, and to use mineralizers such as B_2O_3 and P_2O_5. Samples SK-5 to SK-9 were then formulated and fired to 1922°K (3000°F). (See Table 17.) The yield of mullite was significantly higher for this series, however some cristobalite and α-alumina were still present.

Concurrent with this synthesis study, a separate investigation was directed toward finding a source of pure mullite. A source for leached mullite with low Fe_2O_3 and TiO_2 content was found, and thus, the effort to synthesize a high purity kyanite was discontinued. Although petalite could also be synthesized it was found that the relatively low impurity content did not warrant further refinement and control at this point in the development program.

3.1.3 THERMAL RADIATIVE PROPERTY STUDY

3.1.3.1 Orbital and Entry Thermal Radiative Requirements

The forcing functions for both the orbital and entry thermal radiative requirements are graphically illustrated in Figures 23 (a) and (b). During orbit, the REI equilibrium temperatures are proportional to the fourth root of the solar absorptance: emittance ratio (α_s/ϵ_H), as plotted in Figure 23 (a). Original North American Rockwell Corp. (N/R) design requirements had established an $\alpha_s:\epsilon_H$ ratio of 0.40-0.50 as an optimum goal for orbital temperature control. The criticality of achieving this goal is

47

Table 16

SR-2 Type Coatings Formulated With Pure Chemicals (Series I)

| Coating | Composition (Parts by Weight) | | | | | | | Results |
	Al_2O_3	SiO_2	Li_2CO_3	CaO	MgO	BaO	HfO_2	1644° K (2500° F) Firing for 1 hr.
SR-S1	125	240	10	4	18.5	-	-	Porous, white-cream colored coating. No attack, some small pin holes and shrinkage cracks.
SR-S2	125	240	10	2.2	30.0	-	-	Impervious, white-cream colored coating, free of pin holes and shrinkage cracks.
SR-S3	125	240	10	2.2	18.5	5.0	-	Porous, white-cream colored coating with some pin holes and shrinkage cracks.
SR-S4	125	240	10	2.2	18.5	-	45.0	Good coating, white, impervious, solar absorption $\alpha_s \sim 0.1$.

Table 17

Formulations for Synthetic Minerals

Parts by Weight

Synthetic Petalite	Li$_2$CO$_3$	Al(OH)$_3$	SiO$_2$	Li$_2$SiO$_3$	LiAlO$_2$	Lithsil-4
SP-1	24.8	52	160	-	-	-
SP-2	-	52	140	30	-	-
SP-3	-	-	160	-	44	-
SP-4	-	52	61	-	-	455

Synthetic Kyanite	AlCl$_3$	Cab-O-Sil	Al$_2$O$_3$	SiO$_2$	Al(OH)$_3$	B$_2$O$_3$	P$_2$O$_5$
SK-1	72	28	-	-	-	-	-
SK-2	-	-	72	28	-	-	-
SK-3	-	14	72	14	-	-	-
SK-4	-	28	72	-	-	-	-
SK-5	-	-	-	28	110	-	-
SK-6	-	-	-	28	110	-	-
SK-7	-	-	-	28	110	2	-
SK-8	-	-	-	28	110	2	5
SK-9	-	8	-	28	110	2	-

Table 18

XRD Results for SK-1 Through SK-4 Calcined at 1922° K (3000° F)

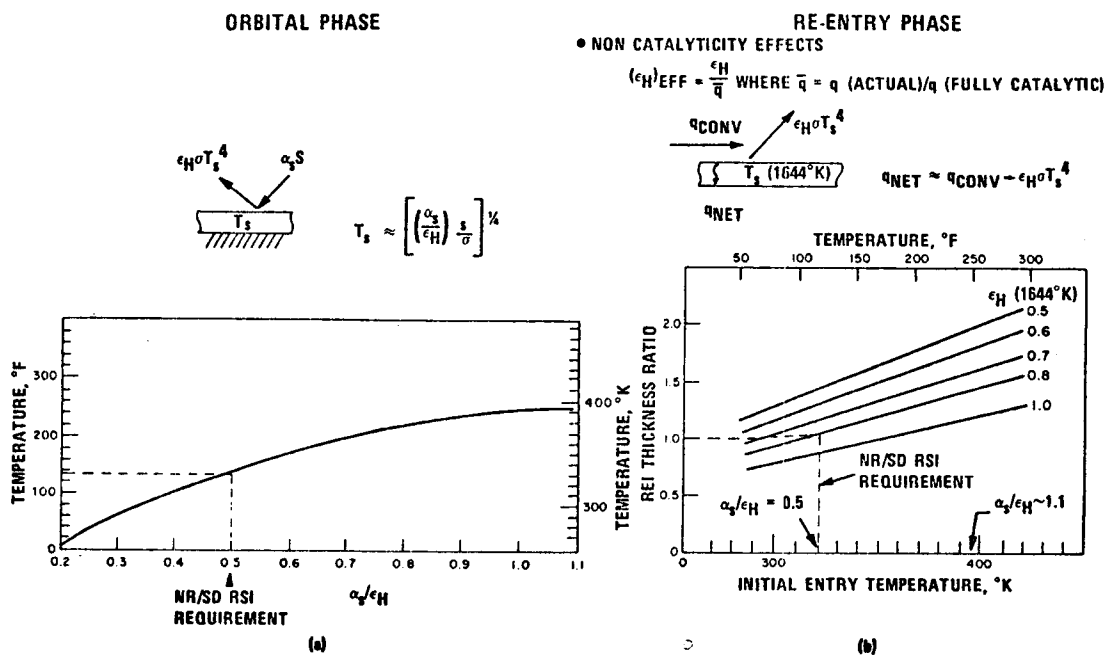| Specimen	Phases Identified
SK-1	Mullite, a low concentration of α-Cristibalite
SK-2	α-Alumina, a high concentration of α-Cristobalite, and a medium concentration of Mullite.
SK-3	α-Alumina, a high concentration of α-Cristobalite, and a medium concentration of Mullite.
SK-4	α-Alumina, a high concentration of α-Cristobalite, and a medium concentration of Mullite.

Figure 23. Origin of orbital and entry thermal radiative requirements.

illustrated from one point of view in Figure 23 (b) where normalized basic insulation thickness is plotted as a function of initial entry temperature (or α_s:ϵ_H ratio). The thickness relationship holds true for the entire thermal protection system (TPS) surface area and, therefore, has significant systems weight impact. Figure 24 (a) shows the results of a TPS weight-sensitivity analysis recently conducted by N/R (Reference 11) which clearly shows the significant influence of the orbital α_s:ϵ_H ratio in terms of orbiter weight. In addition to the TPS sensitivity, the subsystem thermal control system (TCS) has a similar sensitivity to the surface coating α_s:ϵ_H ratio. Figure 24 (b) shows the results of a TCS sensitivity analysis also conducted by N/R (Reference 11) which shows that above a ratio 0.8 active cooling of additional large subsystems may be required. Also of importance is the simultaneous achievement of a high temperature emittance during re-entry as illustrated by the surface boundary condition in Figure 23 (b). The systems weight impact of high-temperature, re-entry emittance, although significant, is less than that of (α_s/ϵ_H) control, primarily because its effect decreases with peak surface temperature. If the beneficial effects of coating non cata-lyticity are taken into account (as shown in the boundary condition in Figure 23 (b)), an effective emittance during re-entry more correctly describes the re-radiating capability of the orbiter surface.

3.1.3.2 Definition of Coating Characteristics

The experimental approach taken focussed initially upon meeting the orbital requirement. A hypothetical "ideal" coating was defined which exceeded the N/R orbital requirement. This served as a basis for screening candidate coating systems. Figures 25 (a) and (b) show the nature of this "ideal" coating in terms of its spectral reflectance distribution over the range of pertinent wavelengths which are used for estimating solar absorptance and low- and high-temperature emittance. Figure 25 (c) lists the equations used for evaluating these functions numerically. As a point of reference, the peaks of the respective black-body energy distributions are listed. Thus, in order to meet the solar absorptance goal, a high reflectance is required between 0.4 and 1 micron. The low temperature emittance requirement is achieved with a coating which has low reflectance in the 2 to 25 micron region. The more difficult to achieve high temperature emittance property requires low spectral reflectance down to about 1.5 microns, at which point an abrupt rise in reflectance is required to maintain the spectral reflectance necessary for optimum solar absorptance.

3.1.3.3 Selection of Candidate Pigments

A literature search was initially conducted of available emittance data on refractory oxides. Non-oxide systems were eliminated from consideration due to potential problems associated with an environmentally reactive surface during re-entry. In general, it was found that the refractory oxides had a high emittance in the far infrared wavelength regions (~10 μm) but a low emittance in the near and medium infrared. Typical near and medium-infrared spectral emittance data of four polycrystalline oxides (Ref. 12) is shown in Figure 26. The development of the vibrational absorptance edge (Note: spectral emittance is equivalent to spectral absorptance for opaque bodies by Kirchoff's

51

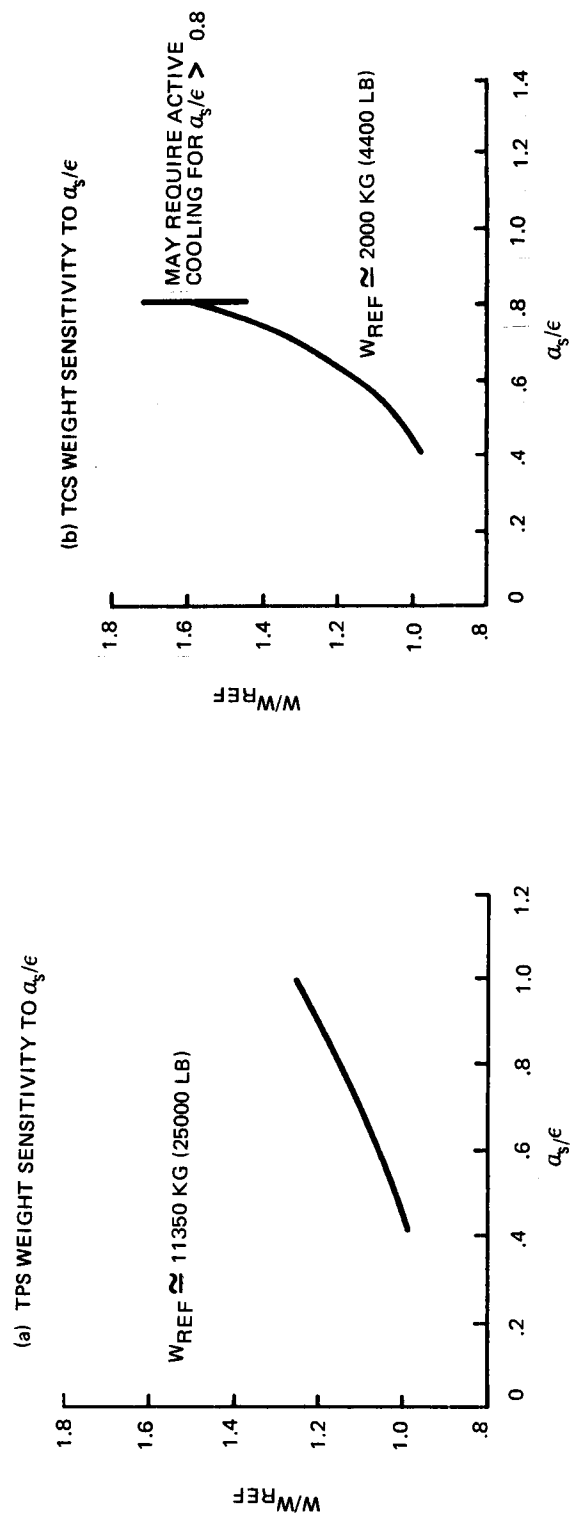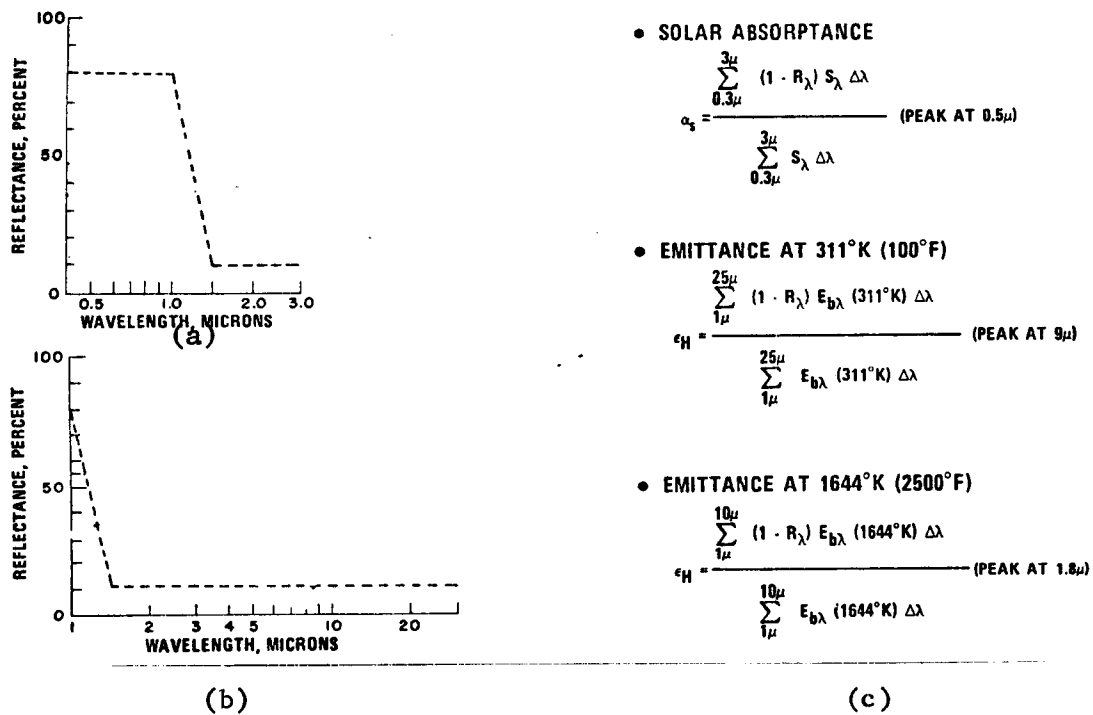Figure 24. System weight sensitivity to α_S/ϵ_H (Reference 11)

Figure 25. Selection of an Optimized Thermal Radiative Coating System
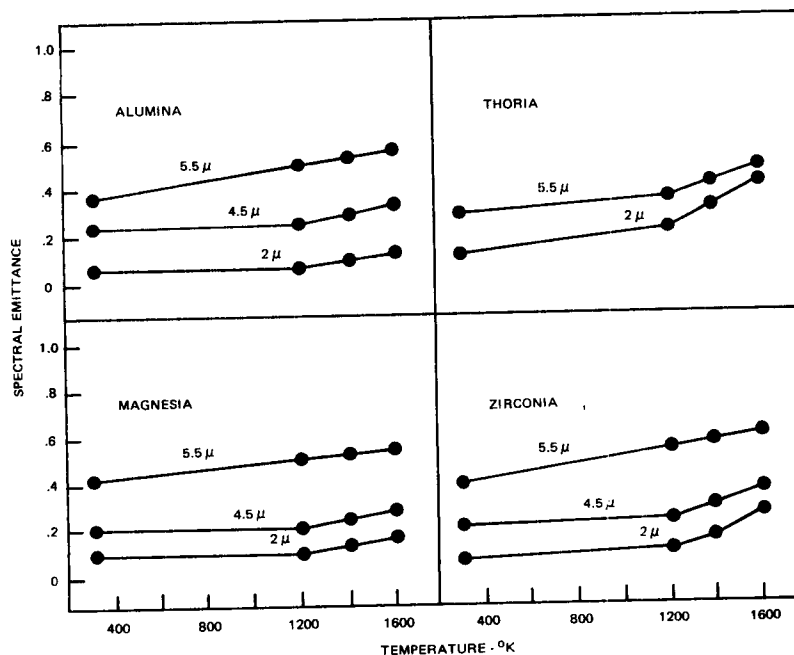

Figure 26. Temperature dependence of normal spectral emittance of four polycrystalline ceramic oxide (Ref. 12)

53

law) for each of these oxides occurs at approximately 5 μm. Also, the data show a relatively weak dependence of spectral emittance with temperature. Two investigators, who evaluated HfO_2, found it to have a high-temperature emittance function approaching 0.80. (References 13 and 14). Also, CeO_2 was reported by at least two sources to have a high-temperature emittance function also approaching 0.80 (Reference 14 and 15). Thus, exceptions to the previous rule that most refractory oxides have low near-infrared spectral emittance were found. Experimental research with these oxide systems conducted on this program has provided considerable insight into the behavior of these apparently anomalous oxides. Oxide purity, stoichiometry, particle size and thickness were found to major variables. Slight variations in some of these parameters were found to significantly alter spectral reflectance functions.

3.1.3.4 Coating Development — Orbital Requirement

Table 19 lists the major components of the SR-series coating system. The approach taken for meeting the orbital optical requirement was to replace the NiO pigment of the SR-2 coating system with candidate "white" oxides. In addition, the basic coating system, without any pigment was also evaluated. Figures 27 and 28 compare the spectral reflectance functions for the more promising oxides (HfO_2, CeO_2) which were reported in the literature to also possess relatively high emittance at elevated temperatures. Also included for comparison is the spectral reflectance function of the original SR-2 coating pigmented with NiO. From this data (using the equations listed in Figure 25 (c)), the α_s/ϵ_H at 311°K (100° F) was computed. Table 20 lists the results of these computations. Also listed is the NR orbital design requirement. The HfO_2 pigment was found to best meet the orbital requirement. The CeO_2 pigment initially produced an unacceptable coating, however, after a high temperature heat treatment, the spectral reflectance function increased in the visible wavelength region providing a coating which now satisfied the orbital requirement. This acceptable reflectance characteristic was found to be stable after subsequent recycling at elevated temperatures.

Table 19

Major Components of the SR-Series Coating System

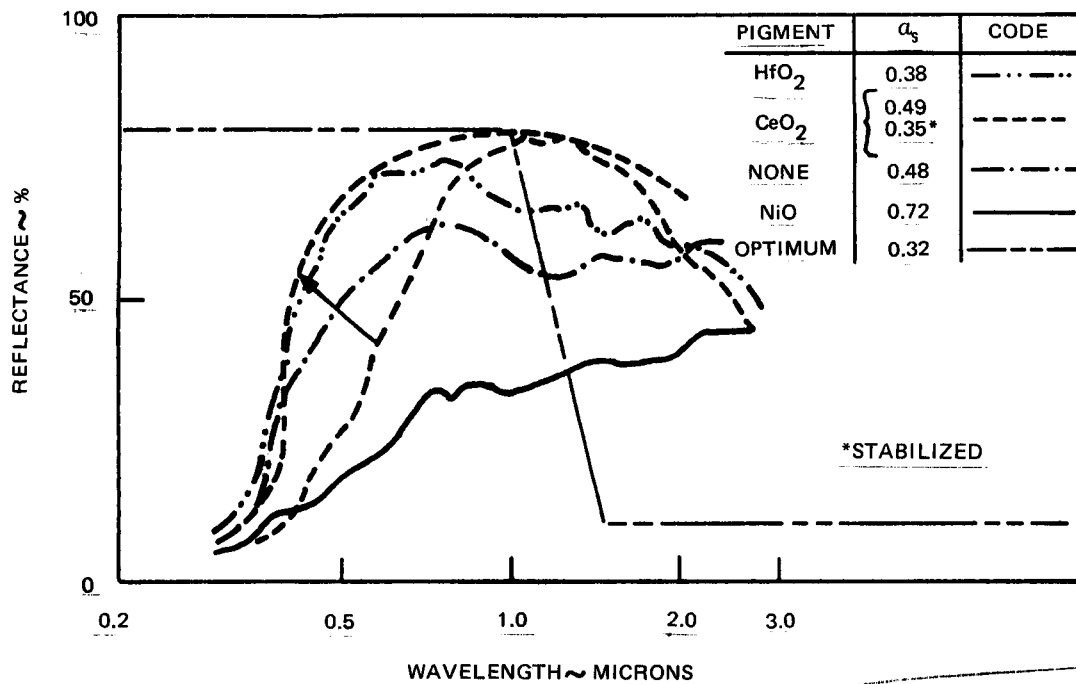| Component	Composition	Primary Function
Kyanite	$3Al_2O_3 \cdot 3SiO_2$	Stable Filler
Petalite	$Li_2O \cdot Al_2O_3 \cdot 8SiO_2$	Thermal Expansion Control
Glass	$SiO_2 - Al_2O_3 - MgO - CaO$	Strength, H_2O Repellency, Non Catalycity
Pigment	HfO_2 (SR-2 HF) NiO (SR-2)	Thermal Radiative Property Control

Figure 27. Spectral reflectance of candidate SR-series coatings over the solar wavelength region
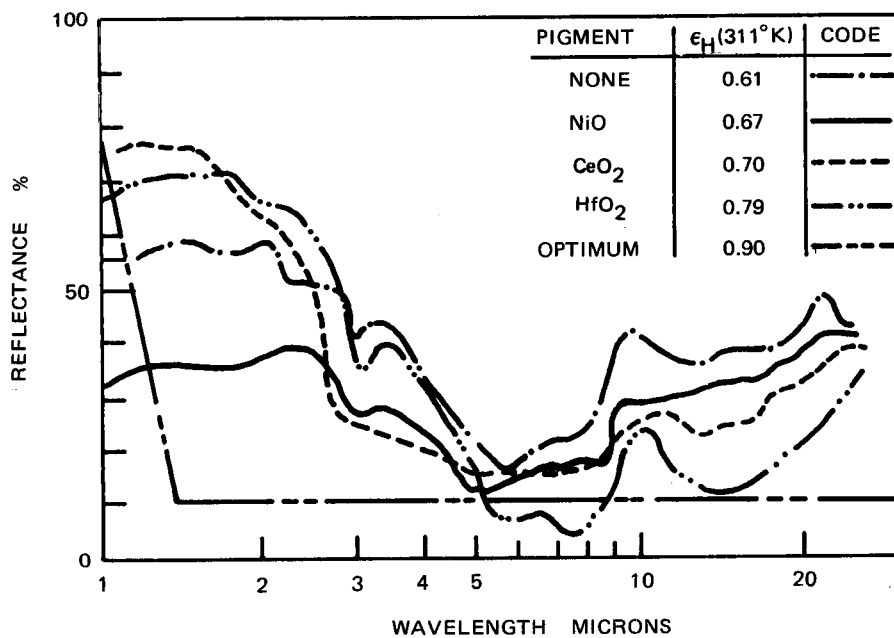

Figure 28. Spectral reflectance of candidate SR-series coatings over the near and far infrared wavelength region

55

Table 20

Summary of Thermal Radiative Property Measurements on Modified SR-Series Coating Systems

| Major Pigment[1] | α_s | ϵ_H (311°K)[4] | α_s/ϵ_H (311°K) | Computed[4] | | Measured[5] |
				ϵ_H (1644°K)	ϵ_H (1366°K)	ϵ_H (1366°K)
NR/SD Requirement	-	-	0.40 - 50	>0.80	-	-
CeO$_2$[2]	0.49	0.70	0.70	0.54	0.61	0.70
CeO$_2$[3]	0.35	0.70	0.50	0.51	0.58	0.70
None	0.48	0.61	0.79	0.53	0.58	0.65
HfO$_2$	0.38	0.79	0.49	0.52	0.60	0.56
NiO	0.72	0.67	1.10	0.68	0.67	0.70

(1) Additional coating impurities include: 1.40 w/o TiO$_2$, 0.94 w/o Fe$_2$O$_3$

(2) As fabricated

(3) Stabilized by subsequent heat treatment

(4) Computed from room temperature spectral data

(5) Non-catalycity in flow environment indicate $\epsilon_H \geq 1.00$

As part of this study, the effect of pigment purity level was evaluated for HfO_2. Figure 29 compares the spectral reflectance of three grades of HfO_2 over the solar wavelength region. The solar absorptance (computed from these data) was found to be sensitive to purity level and, for a given purity level, the vendor source. It was found that the Aremco grade of HfO_2 when used in the SR-series coating best satisfied the orbital α_s: ϵ_H requirement. The HfO_2 pigment data shown in Table 20 used the Aremco grade. The minima in reflectance at approximately 2.8 microns for the 99.9% pure grades is believed to be due to the $[OH]^-$ group which has a characteristic absorption in this wavelength region.

3.1.3.5 Coating Development — Re-entry Requirement

During re-entry, a surface emittance of 0.8 or greater has been established as a goal for the shuttle orbiter. If one assumes that the low temperature spectral reflectance function is invariant with temperature, a prediction of the total hemispherical emittance function at elevated temperatures may be made using Equation 3 shown in Figure 25 (c). The results of these calculations are included in Table 20. The HfO_2 pigmented SR-series coating (and the CeO_2 system) are predicted to have high temperature emittance functions which would fall short of the 0.80 emittance goal. Direct high temperature emittance measurements were performed to evaluate the validity of these predictions.

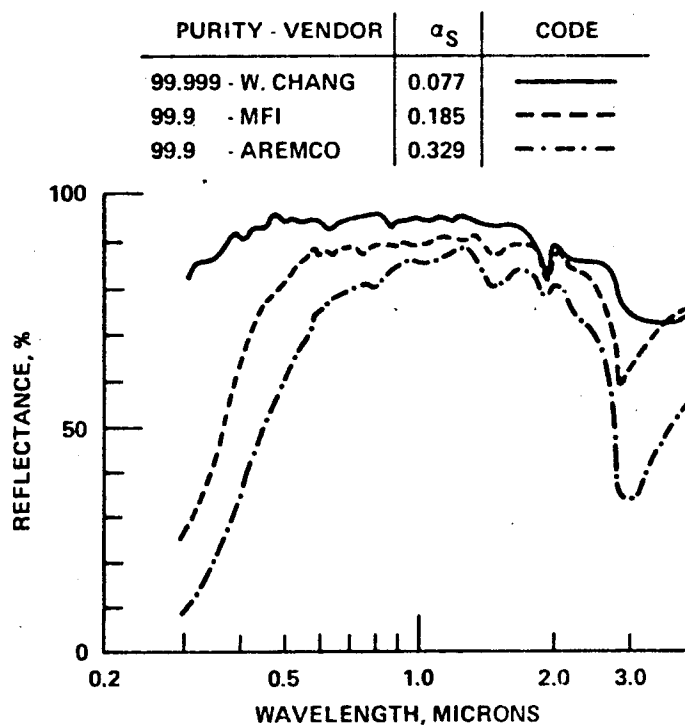| PURITY - VENDOR	α_S	CODE
99.999 - W. CHANG	0.077	————
99.9 - MFI	0.185	— — — —
99.9 - AREMCO	0.329	— · — · —

Figure 29. Spectral reflectance of HfO_2 pigments over the solar wavelength region

Measurement techniques included calorimetry, radiometry, and deductions made from plasma arc testing. Figure 30 illustrates the high temperature emittance data obtained on the HfO_2 modified SR-series coating (SR-2 HF-1C). Emittance data deduced from plasma arc testing indicates that the goal requirement is satisfied up to 1422°K (2100°F). Both the calorimetric and radiometric techniques indicated a somewhat lower value. Also shown for comparison are the integrated emittance data computed from low temperature spectral reflectance measurements shown previously in Figure 28. The 1366°K (2000°F) prediction agrees with both the radiometric and calorimetric measurements. The predicted function above 1366°K (2000°F) crosses the plasma arc data, being slightly higher at 1644°K (2500°F). Additional research was initiated to further enhance the high temperature emittance of the hafnia doped system. Techniques considered included particle-size control and modification of the intrinsic optical absorption edge of HfO_2.

To tailor the absorption edge, the parameters governing the optical vibration frequency must be altered. This frequency is a function of the reduced cation-anion mass of the oxide, coordination number, and interatomic spacing.

By adding impurities that form a solid solution with hafnia, both the lattice constant and the effective mass of the lattice can be altered. The addition of 5% Zirconia to 99.999% pure HfO_2 was found to measurably shift this absorption edge as shown in Figure 31.
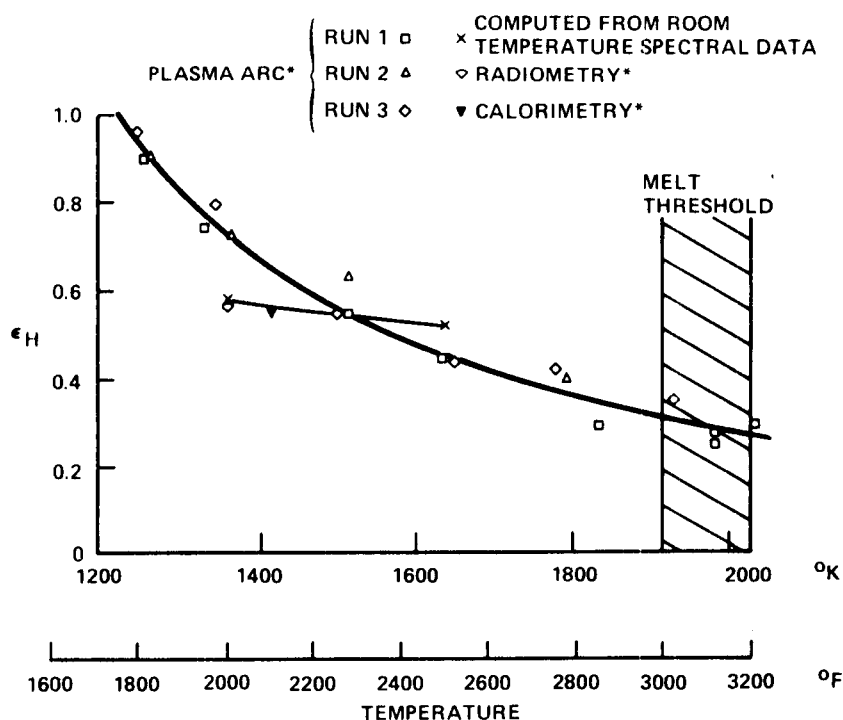

Figure 30. Comparison of total hemispherical emittance of the SR2-HF1
coating system measured by different techniques
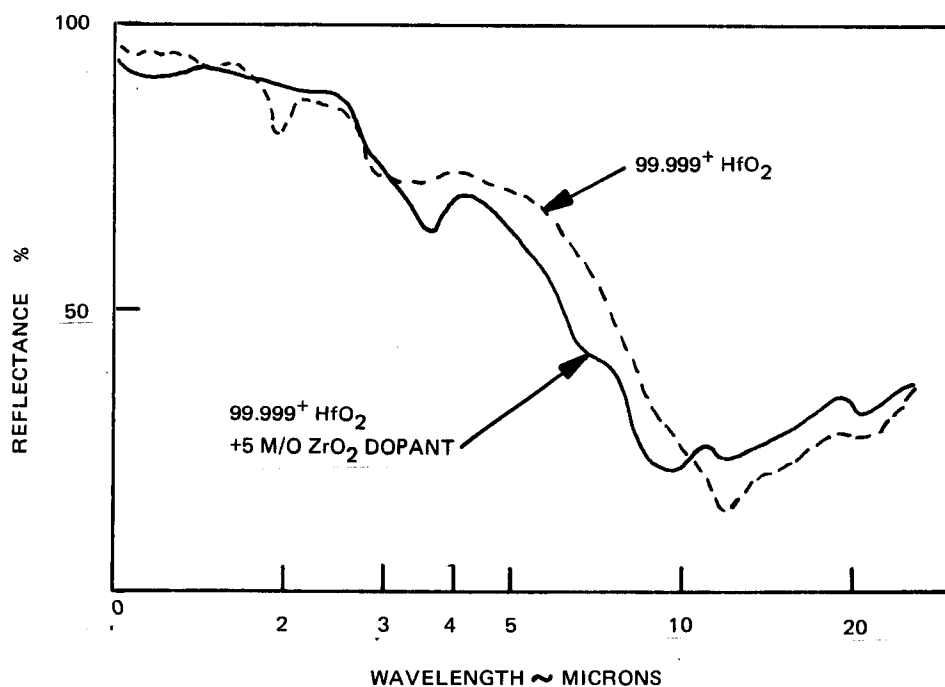(Measurement techniques are described in Appendix 3)

58

Figure 31. Comparison of the spectral reflectance function
of ZrO_2 doped HfO_2 with that of pure HfO_2 over
the near and far infrared wavelength region

It is reasonable to assume that the addition of TiO_2 or a greater percentage of ZrO_2 will shift the absorption edge even further thereby giving a mechanism for tailoring this property. Unfortunately, time did not permit full exploration of this approach, although preliminary results were encouraging.

Another approach taken to favorably control the optical absorption edge was to obtain a material whose absorption edge was intrinsically temperature dependent. The CeO_2 pigment was found to exhibit this characteristic. Radiometric emittance measurements at 1366°K (2000°F) indicated an emittance level of 0.70 compared to a predicted level (computed from low temperature spectral reflection data) of 0.58. Since generally good agreement was obtained with other systems between the computed and measured high temperature emittance (SR-2, SR-2 HF-1C), it has been concluded that a significant shift in the near infrared reflectance characteristics occurred with the CeO_2-doped specimens during radiometric measurement. Distinct color-changes were observed during the transient cool-down period.

Further literature study of this phenomenon indicated that CeO_2 has been used as a dopant in the Welsbach mantle to enhance luminosity at elevated temperatures. (Note: the Coleman lantern utilizes a thoria mantle doped with ceria). The stability of the oxides of ceria at reduced pressure and elevated temperature remains to be evaluated, however, it was found that the low temperature α s: ϵ_H ratio after high-temperature exposure during emittance measurements resulted in stabilization of this property at an

59

an acceptable level, as shown in Table 20. Further research with "white" rare-earth pigments appears warranted based upon the results of this preliminary study.

3.1.3.6 Layered Coatings

Since the SR-series coatings consist of two separate layers, the possibility of applying a near-infrared window material over a high-emittance densifier was evaluated. The overlay coating would be of minimal thickness and sufficiently pigmented to satisfy the orbital requirements. At elevated temperatures, the high emittance underlay would contribute to the overall volume emittance because of the partial near-infrared transparency of the overlay. A schematic of this concept is shown below:
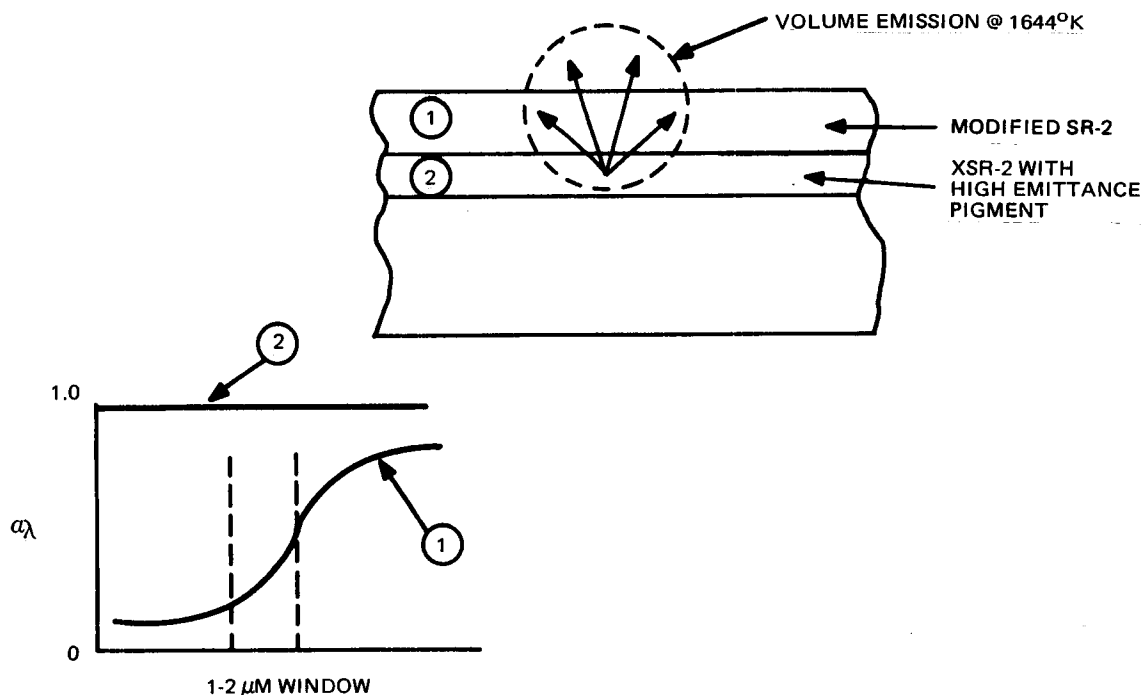
The XSR-2 densifier was pigmented with increasing weight percents of NiO to establish an upper bound for achievable high temperature emittance. Radiometric emittance measurements at $1366°K$ ($2000°F$) are shown in Figure 32; the upper bound for emittance was found to be 0.75. A composite coating consisting of a surface layer passified with TiO_2 and SnO_2 and the 33 w/o NiO pigmented densifier yielded an emittance of 0.62 at $1366°K$ ($2000°F$) which represents a slight increase in emittance (compared to the SR-2 HF measured by the radiometric technique, Figure 30). Although this concept yielded promising results, the complexity of the system discouraged further research.
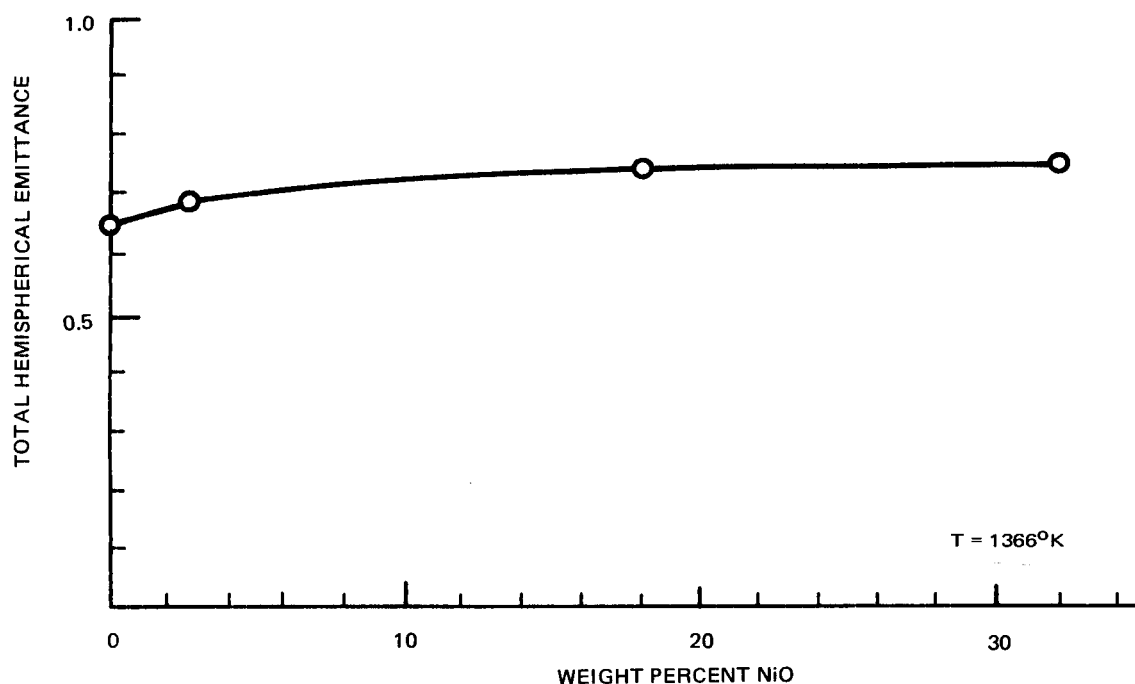
60

Figure 32. Total hemispherical emittance of NiO-doped XSR2
densifier as a function of NiO weight percent

3.1.4 DEVELOPMENT OF NEW COATINGS

3.1.4.1 Glass-Ceramic Coating Systems

The mechanical and thermal properties of a glass-ceramic are frequently superior to those of the parent glass. Tensile strengths and refractoriness generally increase, however, achievement of optimum properties is critically dependent upon composition, nucleation treatment and subsequent crystallization. In general, an optimum nucleation and growth rate may be identified for a given system, as shown schematically in Figure 33. A typical processing cycle for the production of a glass-ceramic from a glass melt is shown in Figure 34. For this study, a coating composition was sought which could be processed at temperatures below the maximum reuse temperature of 1644° K (2500° F), yet, when crystallized would impart increased strength and refractoriness superior to the SR-series coating. Impetus to this research was given by a concurrent systematic study in the Li_2O-SiO_2 system (Reference 17) where fracture strength was doubled by controlled nucleation and crystallization of a binary glass melt.

The approach selected for this task was to develop a glass which, with proper annealing, could be converted to a strong glass-ceramic and which would be refractory to 1644° K (2500° F) and would have a thermal expansion compatible with REI-Mullite.
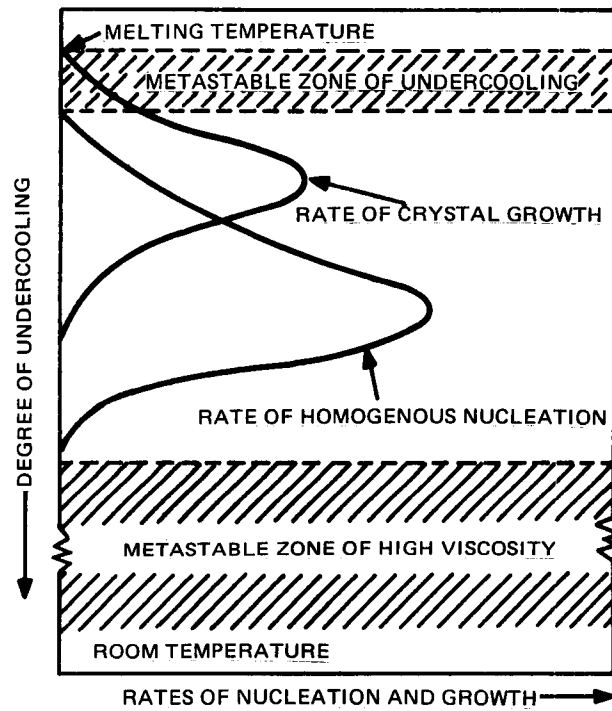
61

Figure 33. Rates of homogeneous nucleation and crystal growth as functions of degree of undercooling in viscous liquid (Ref. 16).
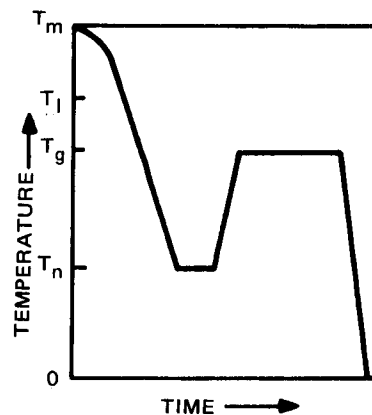

Figure 34. A processing cycle for production of a glass-ceramic from a glass-forming melt. T_m = melt temperature; T_l = liquidus; T_g = temperature of maximum crystal growth rate; T_n = temperature of maximum nucleation rate (Ref. 16).

62

The first composition selected was designed to yield a mullite phase. This composition consisted of:

SiO_2	30 w/o
Al_2O_3	40 w/o
B_2O_3	20 w/o
MgO	5 w/o
ZnO	5 w/o

This composition was too refractory and could not be melted in the equipment available within our laboratories. The next composition evaluated was designated GC-1 and consisted of:

SiO_2	40 w/o
Al_2O_3	20 w/o
B_2O_3	20 w/o
MgO	10 w/o
ZnO	10 w/o

This glass was melted at 1755°K (2700°F) for 4 hours and fritted into water. Samples of this glass were given various heat treatments as listed in Table 21 and then characterized by XRD to determine the structure of the nucleated phase. X-ray diffraction photographs were obtained for each sample (utilizing a 57.3 mm diameter x-ray diffraction camera and nickel filtered copper radiation). Figures 35(a) through (d) are densitometer traces recorded from the resulting x-ray diffraction photographs.

Table 21

Heat Treatments of GC-1 Glass

Sample No.	Heat Treatment	Cooling Treatment
1	1644°K(2500°F) - 1 hr.	Air Quench
2	1644°K(2500°F) - 1 hr. plus 4 hrs @ 2000°F(1366°K)	Air Quench
3	1644°K(2500°F) - 1 hr. plus 4 hrs @ 2200°F(1477°K)	Furnace Cool
4	1644°K(2500°F) - 1 hr. plus 4 hrs @ 2200°F(1477°K)	Air Quench
5	1644°K(2500°F) - 1 hr. plus 4 hrs @ 2300°F(1533°K)	Furnace Cool
6	1644°K(2500°F) - 1 hr. plus 4 hrs @ 2300°F(1533°K)	Air Quench

63

Sample 1 (See Table 21) produced a non-crystalline type of x-ray diffraction pattern, i.e., no sharp peaks or diffraction lines. Samples 2 through 6 each indicated sharp peaks (diffraction lines) in addition to a diffuse background which indicates the presence of a non-crystalline component. Identification of these sharp peaks indicated the crystalline component to be zinc aluminate. This compound (zinc aluminate) appeared in all of these samples (2 through 6) in various concentrations.

This glass was formulated in the hope of yielding a glass-ceramic with a principal phase of cordierite. The constraints placed on the glass were a low thermal expansion, and a glass that could be heat treated and melted at a maximum temperature of 1644°K (2500°F). To maintain a low thermal expansion, it was imperative that the alkalis not be incorporated into the formulation. Of the alkaline earths, only MgO and ZnO appeared promising. When sufficient MgO, ZnO and B_2O_3 were incorporated into matrix to produce a glass which could be melted at the required temperature, the principal phase developed was zinc aluminate which would not be a desirable second phase because of its relatively high thermal expansion compared to REI-Mullite. Although not demonstrated on this subtask, it is believed that continued research on the development of a compatible RSI glass-ceramic coating would be a desirable approach toward achieving increased strain and strength capability, fracture toughness and impact resistance.

3.1.4.2 Cordierite Coatings

The crystalline nature and expansion characteristics of compositions in the region surrounding the cordierite area of the system $MgO-Al_2O_3-SiO_2$ have been examined by a number of investigators.[18,19] Their results indicate a coating based on the cordierite system would have thermal expansion characteristics compatible with REI-Mullite and have a maturing temperature in the proper range for this application. Hummel and Reid (Ref. 18) found, for example, that the thermal expansion varies from 1.1 to 2.8 x 10^{-6} in/in°F, the upper-limit expansion being compatible with REI-Mullite.

Four formulations were prepared as a slurry and "puttied" into a machined cavity in an REI block. After drying, the blocks were fired to 1644°K (2500°F) in 3 hours and held at 1644°K (2500°F) for one hour. Table 22 lists the chemical composition and the results of the experiment. The first three formulations severely attacked the REI during firing and there was no evidence of remaining coating material. The fourth formulation (CORD 4) attacked the REI to a much lesser degree and sintered into dense mass. An REI tile was coated with CORD 4 after being densified in the standard manner and fired to 1644°K (2500°F) for one hour. This formulation did not form an impervious coating but only sintered into a granular surface coating.

Table 22

Formulations and Results of First Series of Cordierite-Based Coatings

Coating	Composition (w/o)			Results of 1644°K (2500°F) Firing in REI Cavity
	MgO	Al_2O_3	SiO_2	
CORD-1	15	25	60	Very serious attack of REI
CORD-2	15	20	65	Very serious attack of REI
CORD-3	20	25	55	Very serious attack of REI
CORD-4	15	30	55	Some attack – refractory sphere of coating remained.

These results indicated that the range of compositions available as a potential coating in the pure MgO-Al$_2$O$_3$-SiO$_2$ system were extremely limited. The compositions with low alumina content severely attack the REI and a composition with a slightly higher alumina content (CORD 4) was too refractory.
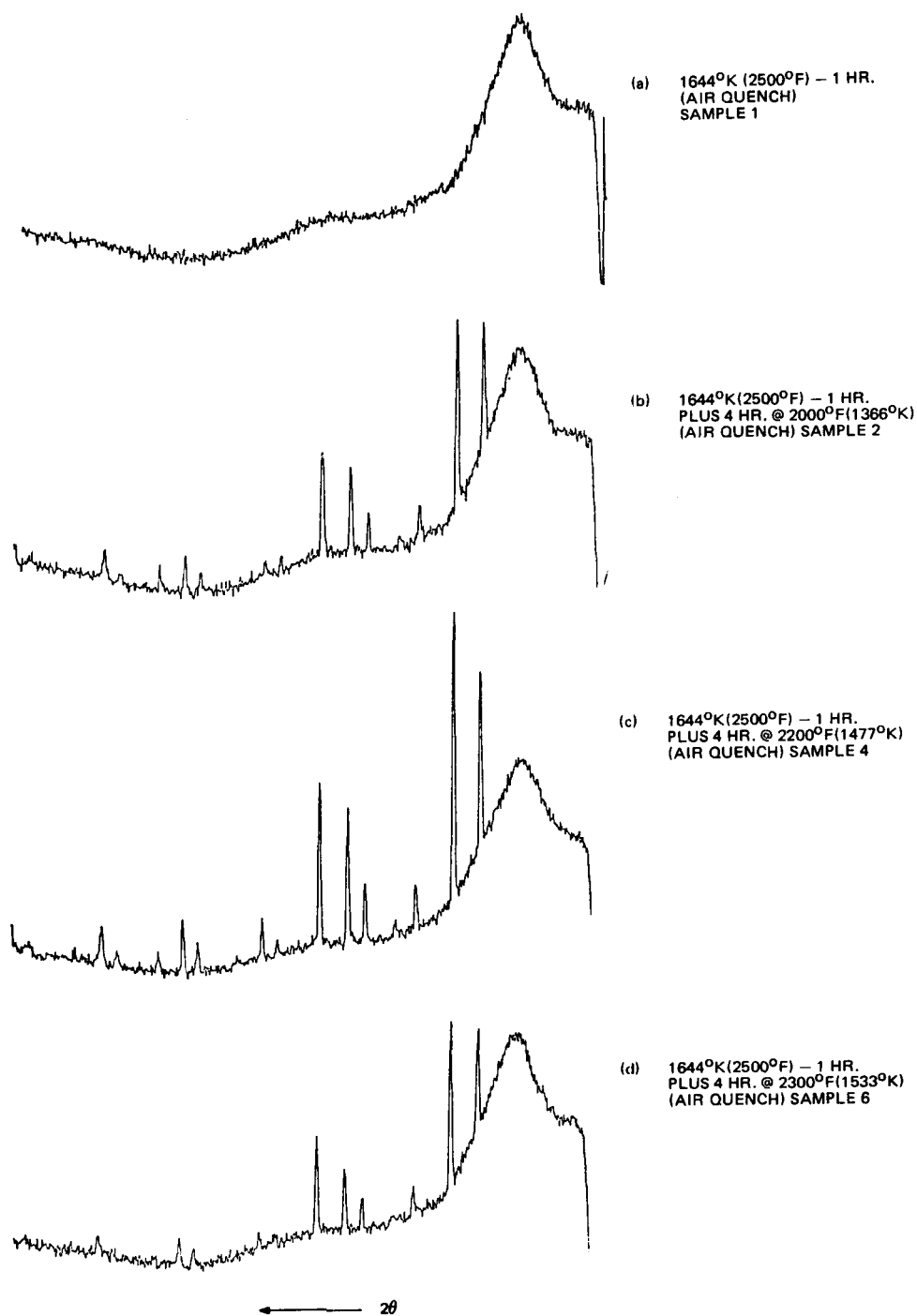

(a) 1644°K (2500°F) — 1 HR.
(AIR QUENCH)
SAMPLE 1

(b) 1644°K(2500°F) — 1 HR.
PLUS 4 HR. @ 2000°F(1366°K)
(AIR QUENCH) SAMPLE 2

(c) 1644°K(2500°F) — 1 HR.
PLUS 4 HR. @ 2200°F(1477°K)
(AIR QUENCH) SAMPLE 4

(d) 1644°K(2500°F) — 1 HR.
PLUS 4 HR. @ 2300°F(1533°K)
(AIR QUENCH) SAMPLE 6

2θ

Figure 35. XRD patterns of GC-1 glass-ceramic coating after several nucleation heat treatments

66

SECTION 4
DEFINITION OF AN OPTIMIZED RSI SYSTEM

4.1 BASIC INSULATION

The use of small diameter mullite fibers (1-2 μm), as synthesized by the Babcock & Wilcox Co., will result in optimized mechanical and thermal properties for a low-density, rigidized fibrous insulation. The intrinsic phase and dimensional stability (resistance to viscous flow) of this fiber at 1644°K (2500°F) are unequalled by currently commercially available fibers. Since the quaternary oxide system upon which this fiber is based is relatively unexplored in terms of physical properties, it is reasonable to assume that improvements in strength and strain capability of the fiber can be achieved through further research.

Reductions in thermal conductivity of the basic insulation can be achieved, not only through the use of small-diameter fibers, but also by applying fiber:void opacifiers to the system. Unfortunately, neither of these laboratory innovations could be incorporated into program deliverables.

The continued use of a ternary oxide glass binder (SBA-10) to initially form optimized fillets (and whose refractoriness increases through interaction with the mullite fiber during subsequent firing schedules) appears warranted. Control of firing temperature, time and atmosphere has been found to promote improved mechanical properties.

Table 23 defines an optimized basic insulation for the RSI-Mullite system which was arrived at as a result of both NASA-Langley and GE-RESD sponsored research. Also, listed are the improvements incorporated in program deliverables. In some instances, it was not possible to fully implement each improvement; the reasons for this are given in the remarks column.

4.2 SURFACE COATING

The use of a hafnia-modified SR-series coating has been found to yield a near-optimum RSI surface coating. Improvements in strength and strain capability and intrinsic high-temperature surface emittance are required to increase safety margins and reduce TPS weight, respectively. The use of supplemental reinforcement and/or achievement of mechanical properties characteristic of surface coating material processed in bulk by press and sinter techniques will be required in an optimized RSI system.

Table 23 also defines an optimized surface coating for an RSI system which was arrived at as a result of both NASA-Langley and GE-RESD sponsored research. As was found for the basic insulation component, it was not possible to fully implement each improvement in program deliverables.

Table 23. Definition of an Optimized RSI System

		Optimum	Deliverables	Remarks
I	BASIC INSULATION:			
	A. Fiber	Babcock & Wilcox (B&W) 1-2 μm experimental mullite fiber with opacification coating (or in solid solution)	Babcock & Wilcox (B&W) 4-5 μm experimental mullite fiber	1-2 μm B&W mullite fibers were not available in sufficient quantities to be used in program deliverables. Effects of opacification on physical properties remain to be evaluated.
	B. Binder	SBA-10 ternary oxide glass	SBA-10 ternary oxide glass	
	C. Firing Schedule	1 hr. @ 1533°K (2300°F) using proprietary controlled atmosphere (Mod 1B process)	1 hr. @ 1533°K (2300°F) using Mod 1B process	
II	SURFACE COATING:			
	A. Densifier	XSR-2 densifier fired 1 hr. @ 1366°K (2000°F)	XSR-2 densifier fired 1 hr. @ 1366°K (2000°F)	
	B. Overcoat	Reinforced SR-series coating with modified HfO_2 pigment to enhance intrinsic surface emittance	SR-2 HF-1 (SR-2 pigmented with 99.9 purity HfO_2).	Further optimization of intrinsic surface emittance is required above 1366°K (2000°F) Increase in intrinsic strength and strain capability is required (Note: strength and strain levels of 5590 psi and 0.056% have been measured on large press and sintered specimens) Supplemental fibrous coating reinforcements needed to increase safety margins.
	C. Firing Schedule	Double firing schedule: (1) Isothermal firing to 1533°K (2300°F) in sealed enclosure (side wall coating of lower refractoriness than top surface to promote side-wall groove waterproofing). (2) Gradient firing in sealed enclosure to surface temperature of 1644°K (2500°F) with back-face < 1533°K (2300°F). (3) Firing time: 1 hr. or less.	Double firing schedule: (1) Isothermal firing to 1533°K (2300°F) for 1 hr. with less refractory sidewall coating. (2) Isothermal firing to 1644°K (2500°F) for 1 hr.	Technique for firing in sealed enclosure with gradient firing was not perfected for deliverables (although several attempts were made to implement this technique).
	D. Sidewall Design	Grooved sidewalls with large radii of curvature are required to eliminate sidewall cracking. Also supplemental reinforcement would be desirable. These techniques may not be required if upper-bound achievable SR-2 HF-1 strength and strain levels are achieved.	Grooved sidewall design with less refractory side-wall coating.	

68

SECTION 5
CONCLUSIONS AND RECOMMENDATIONS

5.1 CONCLUSIONS

5.1.1 BASIC INSULATION OPTIMIZATION

The basic insulation optimization studies led to the following conclusions:

1. Significant reductions in thermal conductivity can be achieved by using 1-2 μ m diameter fibers in an RSI composite. Over typical Shuttle pressure and temperature regimes, a factor of two reduction was measured using the Carborundum small-diameter high alumina-silica fiber.

2. The Babcock and Wilcox fibers (both spun and blown) exhibit superior dimensional stability at 1644°K (2500°F) compared to the Carborundum high alumina-silica fiber.

3. The SBA-10 binder (utilized in both the Mod 1-A and 1-B basic insulation processes) yields near-optimum fillet formation with the 4-5 μ m standard Babcock and Wilcox fiber. When used to rigidize small-diameter Babcock and Wilcox fiber panels, binder accumulation on unfiberized debris, reduced the effectiveness of the binder. Modifications in binder viscosity may be required when processing improved small-diameter fibers produced by the blowing technique. These improved fibers should be available in laboratory-size quantities at the conclusion of a NASA-Lewis sponsored program (NAS 3-16764); also, at this time, a decision will be made regarding higher production quantities.

4. The feasibility of directionally molding panels (to reverse in-plane and transverse direction) such that maximum strength would be achieved in the transverse direction (Z) and maximum strain capability in-plane (X-Y) was demonstrated. Projected mechanical properties using the Mod 1-B process are a potential in-plane strain capability of 0.5-0.6 percent and a transverse tensile strength of 827.4 kN/m^2 ($\sim$ 120 psi) and higher.

5. Coated REI panels fired in a closed system exhibit minimal property degradation when exposed to temperatures of 1644°K (2500°F). Strength and strain capability retention has been partially attributed to minimization of grain-growth inhibiting oxide (B_2O_3, P_2O_5) losses due to vaporization. If this process modification is implemented, the multi-mission re-use capability of REI-Mullite at 1644°K (2500°F) can be significantly extended.

69

5.1.2 SURFACE COATING OPTIMIZATION

The surface coating optimization studies led to the following conclusions:

1. The hafnia modified SR-2 coating process provides a surface coating which meets the original NR/SD orbital $\alpha s/\epsilon_H$ requirement of 0.4-0.5 and also exceeds the entry emittance requirement of 0.80 at 1644°K (2500°F) as a result of its fully non-catalytic surface characteristics. Firing the coating in an impervious enclosure has eliminated mechanical property degradation during the coating firing cycle, thereby significantly extending the multi-mission use capability of the REI-Mullite thermal protection system.

2. The hafnia modified SR-2 coating has improved the surface coating texture, eliminated the frequency of pinhole formation (characteristic of the original SR-2 coating), and has also eliminated the presence of macrovoids in the coating.

3. Techniques for improving surface coating purity, homogeneity and strength:strain capability have been identified, however, additional work will be required to implement these techniques. Improvements include the use of high-purity acid leached kyanite, glass phase modifications to reduce surface roughness and surface coating:basic insulation interface reactivity, firing process modifications to achieve press and sintered properties and, also, the use of supplemental reinforcement (platinum mesh and/or mullite fibers).

5.2 RECOMMENDATIONS FOR FUTURE WORK

5.2.1 BASIC INSULATION OPTIMIZATION

With regard to future recommended basic insulation research, the following areas of work have been identified:

1. A more extensive evaluation of the improved small-diameter Babcock and Wilcox fiber currently being developed on a NASA-Lewis sponsored program (NAS 3-16764) should be conducted. Projected weight estimates indicate that a 1-2 μm RSI-Mullite system will result in a significant reduction in RSI-TPS weight. Further weight reductions may also be achieved through the implementation of fiber:void opacification.

2. The suitability of higher density RSI-Mullite insulation for use as a leading edge component at temperatures up to 1922°K (3000°F) should be assessed.

3. The development of a new fiber incorporating the attributes of both silica (low thermal expansion) and mullite (refractoriness and dimensional/phase stability at 1644°K (2500°F)) should be initiated to further optimize the RSI system margins of safety and overall Shuttle system capability. Research to-date indicates that stabilized phosphate fibers could provide the basic building block for this optimum RSI system.

5.2.2 SURFACE COATING OPTIMIZATION

With regard to future recommended surface coating research, the following areas of work have been identified:

1. Further research is needed to assess the stability of the hafnia-modified SR-2 coating in the orbital space environment and, also, to further enhance its intrinsic high temperature emittance (in the event surface non-catalyticity may not be operable on portions of the Shuttle orbiter).

2. Techniques for achieving press-and-sintered mechanical properties for the hafnia modified SR-2 coating system should be developed to fully utilize its potential intrinsic mechanical capability. In addition, the incorporation of supplemental reinforcement as a strengthening mechanism for the coating system should be fully evaluated.

SECTION 6
REFERENCES

1. R. A. Tanzilli (editor), "Development of an External Ceramic Insulation for the Space Shuttle Orbiter", NASA CR-112038, April 1972.

2. R. M. Fetterolf, "Development of High-Strength, High-Modulus Fibers", AFML TR70-197, August 1970, p. 41.

3. P. J. Gielisse and W. R. Foster, Quarterly Progress Report 931-8, Ohio State University Research Foundation, October 1961, p. 6.

4. "The Rotary Fiber Classifier", Composites, December 1969, pp. 114-117.

5. Vendor Literature on Fiber Classifiers, Ultrasonoscope Company Limited, Sudbourne Road, London SW 2.

6. H. E. Goldstein et. al., "Reusable Surface Insulation (RSI) Materials Research and Development", NASA TM X-2570, May 1972, Figure 28.

7. B. K. Larkin, S. W. Churchill, "Heat Transfer by Radiation through Porous Insulations", A. I. Ch. E. Journal, Vol. 5, 1959, p. 467.

8. H. M. Strong, F. P. Bundy, and H. P. Bovenkerk, "Flat Panel Vacuum Thermal Insulation", Journal of Applied Physics, Vol. 31, January 1960, p. 43.

9. NASA OAST Monthly Report, April 1972.

10. Parmelee, Ceramic Glazes, Industrial Publications, Chicago (2nd Edition), 1951, p. 18.

11. C. L. Statham, R. T. Tsutsui, "Effect of Optical Properties on Thermal Design", presented at the NASA Symposium on Reusable Surface Insulation, NASA-Ames Research Center, Nov. 1-3, 1972.

12. J. C. Richmond, "Thermal Radiation Properties of Ceramic Materials", NBS Special Publication 300, Vol. 7, November 1971.

13. V. S. Moore et. al., "Emittance Measurements of Refractory Oxide Coatings Up to 2900°K", Symposium of Thermal Radiation Properties of Solids, pp. 527-533.

14. "The Thermal Properties of Twenty-six Solid Materials to 5000°F or their Destruction Temperatures", ASD-TDR 62-765, August 1962, p. 164.

15. G.A.W. Rutgers, "Temperature Radiation of Solids", Handbuch de Physik, Vol. p. 167.

16. J. F. MacDowell, "Nucleation in Glasses", Nucleation Phenomena, ACS Publication, 1966, pp. 69-75.

17. S. W. Freiman, L. L. Hench, "Effect of Crystallization on the Mechanical Properties of Li_2O-SiO_2 Glass-Ceramics", Journal of the American Ceramic Society, February 1972, pp. 86-90.

18. F. A. Hummel and H. W. Reid, "Thermal Expansion of Some Glasses in the System MgO-Al_2O_3-SiO_2", J. Am. Ceramic Society, Vol. 34 No. 10, October 1951.

19. R. J. Beals and R. L. Cook, "Low Expansion Cordierite Porcelains", J. Am. Ceramic Society, Vol. 35 No. 2, February 1952.

20. Michalak, R. J., T. E. Hess, "Final Report-Design Applications of Rigidized Reusable Surface Insulation Thermal Protection System, " Contract No. NAS 9-12855, March 1973.

APPENDIXES

APPENDIX 1

COMPILATION OF PROPERTY DATA ON SMALL-DIAMETER FIBER PANELS AND ON DELIVERABLE STANDARD-DIAMETER MOD 1B PANELS

A compilation of the mechanical properties fabricated using small-diameter B&W and Carborundum fibers is given in Figures A-1 through A-10. Dimensional stability data is listed in Table A-1. Also included in Figures A-11 through A-23 are mechanical and thermal property data for Mod 1-B panels (processed using 4.7μ m B&W fibers) and associated SR-2 HF-1 surface coating. These data are representative properties for contract deliverable panels. It should be noted that the data in Figures A-11 through A-23 were generated under NASA-MSC Contract NAS 9-12855. (Reference 20)

Table A-1. Shrinkage Data on Small-Diameter Panels

Specimen	Density (lb/ft³)	Dimensional Change (%)			Volume Change (%)
		X	Y	Z	
Carborundum (FJC-1)	16.9	-0.90	-0.70	-0.70	-2.20
Carborundum (FJC-6)	11.5	-0.75	-0.60	-3.10	-4.50
B&W-Blown (FJC-8)	12.6	-0.10	-0.20	-0.10	-0.50
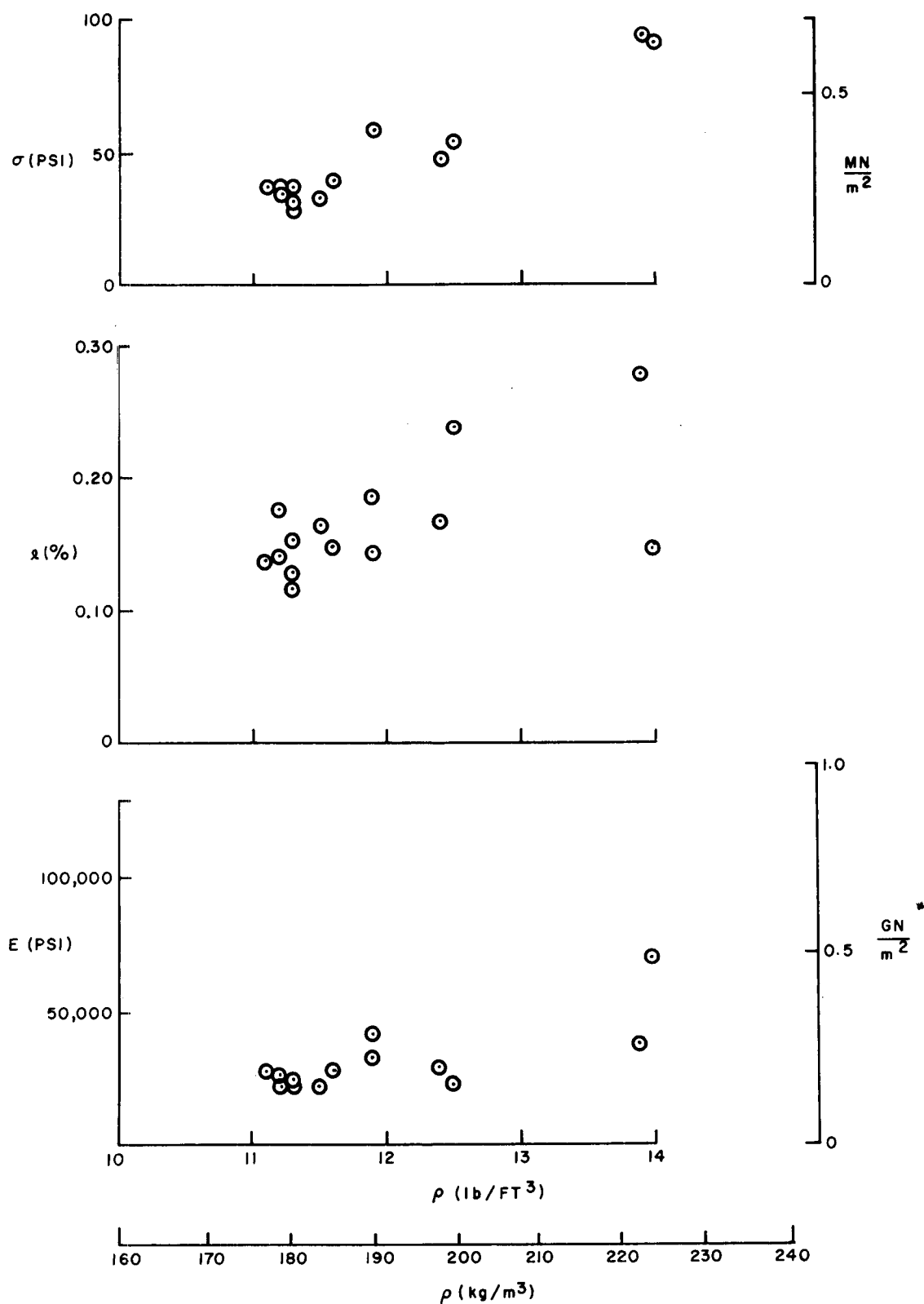
Figure A-1. Mechanical behavior of 4μm B&W spun fiber panel (in-plane, tension-FJC-5).
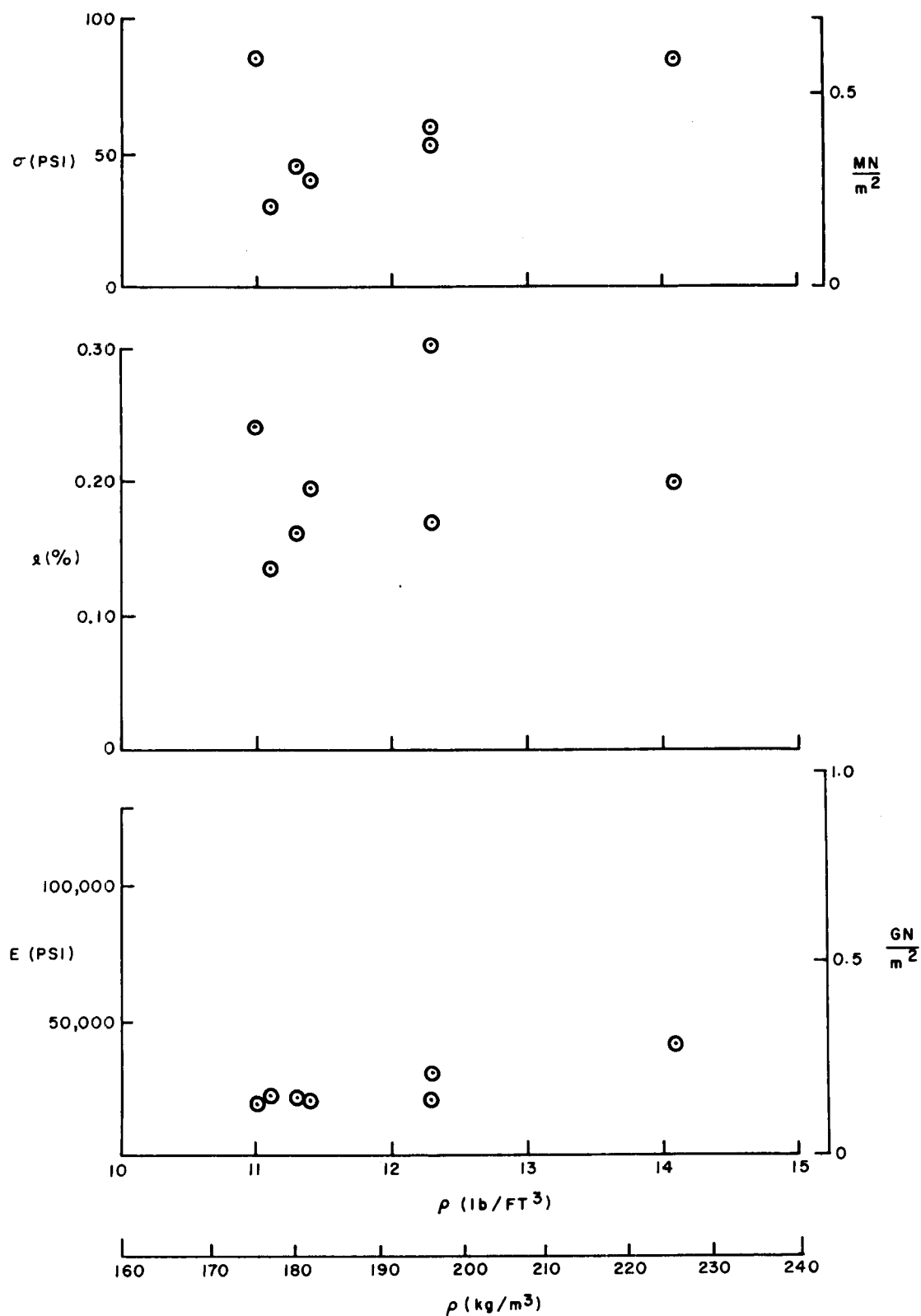
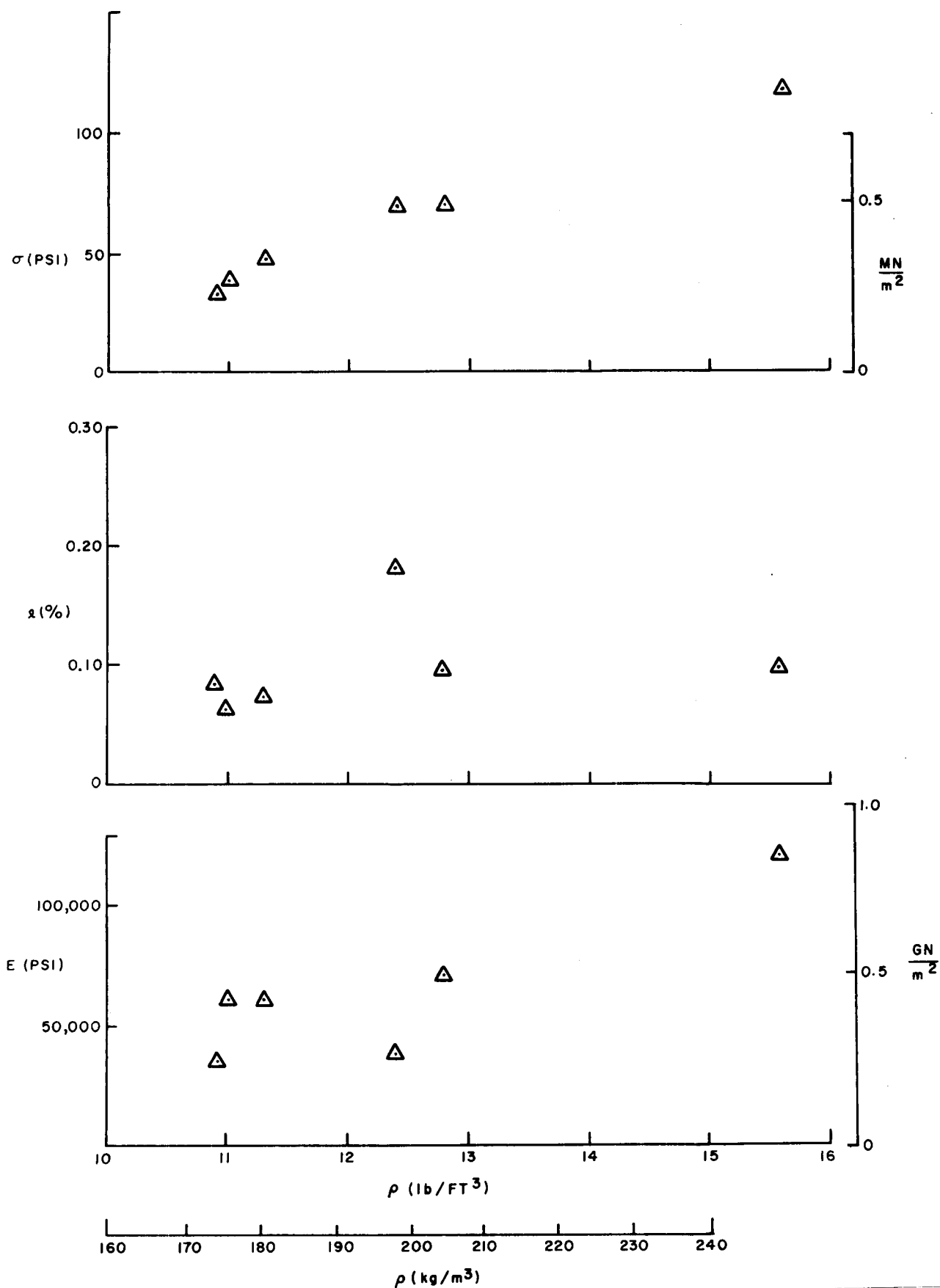Figure A-2. Mechanical behavior of 4μm B&W blown fiber panel (in-plane, tension-FJC-8).

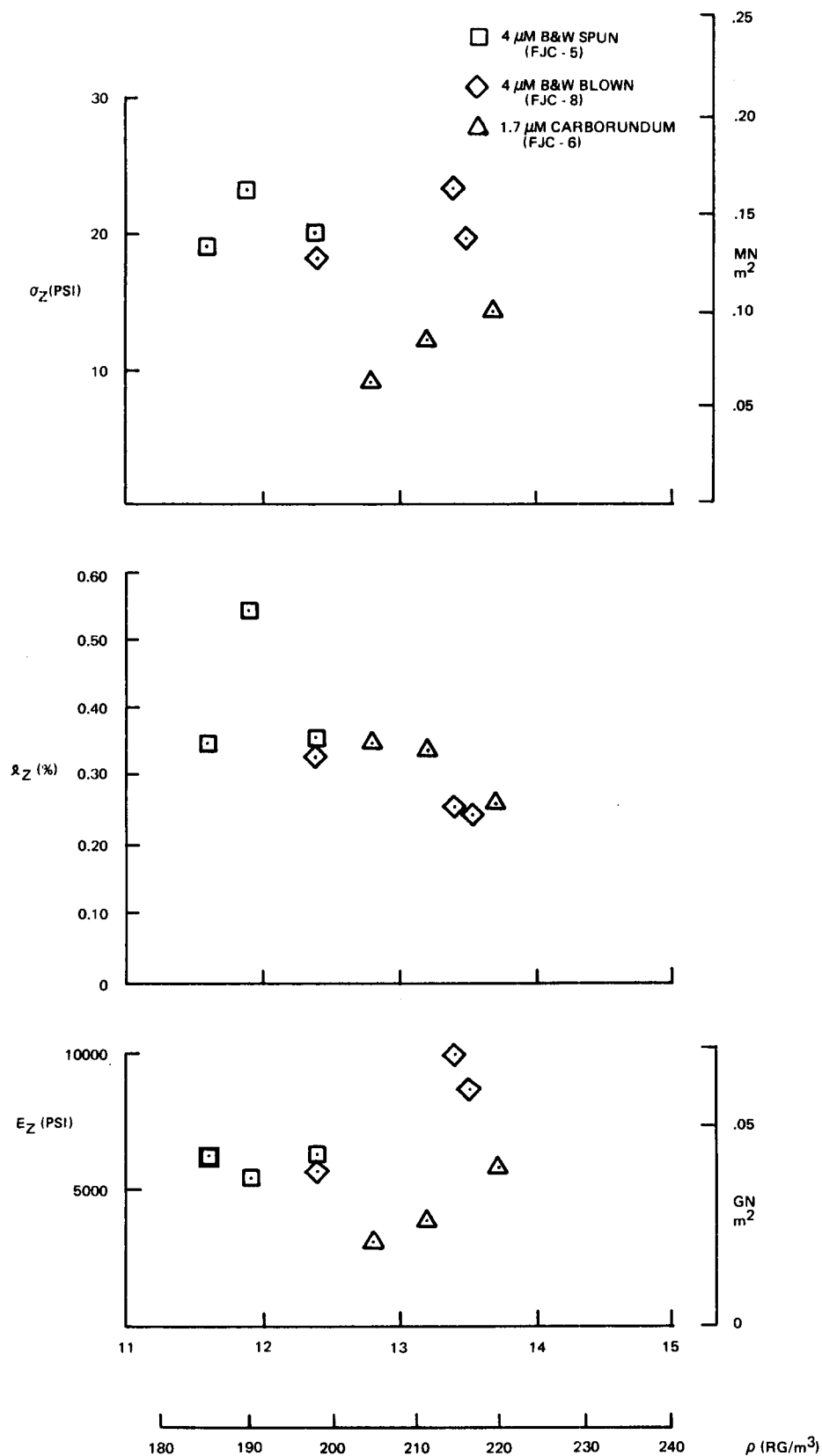Figure A-3. Mechanical behavior of 1.7μm Carborundum fiber panel (in-plane, tension-FJC-6).

78

Figure A-4. Mechanical behavior of small diameter fiber panels (transverse, tension).
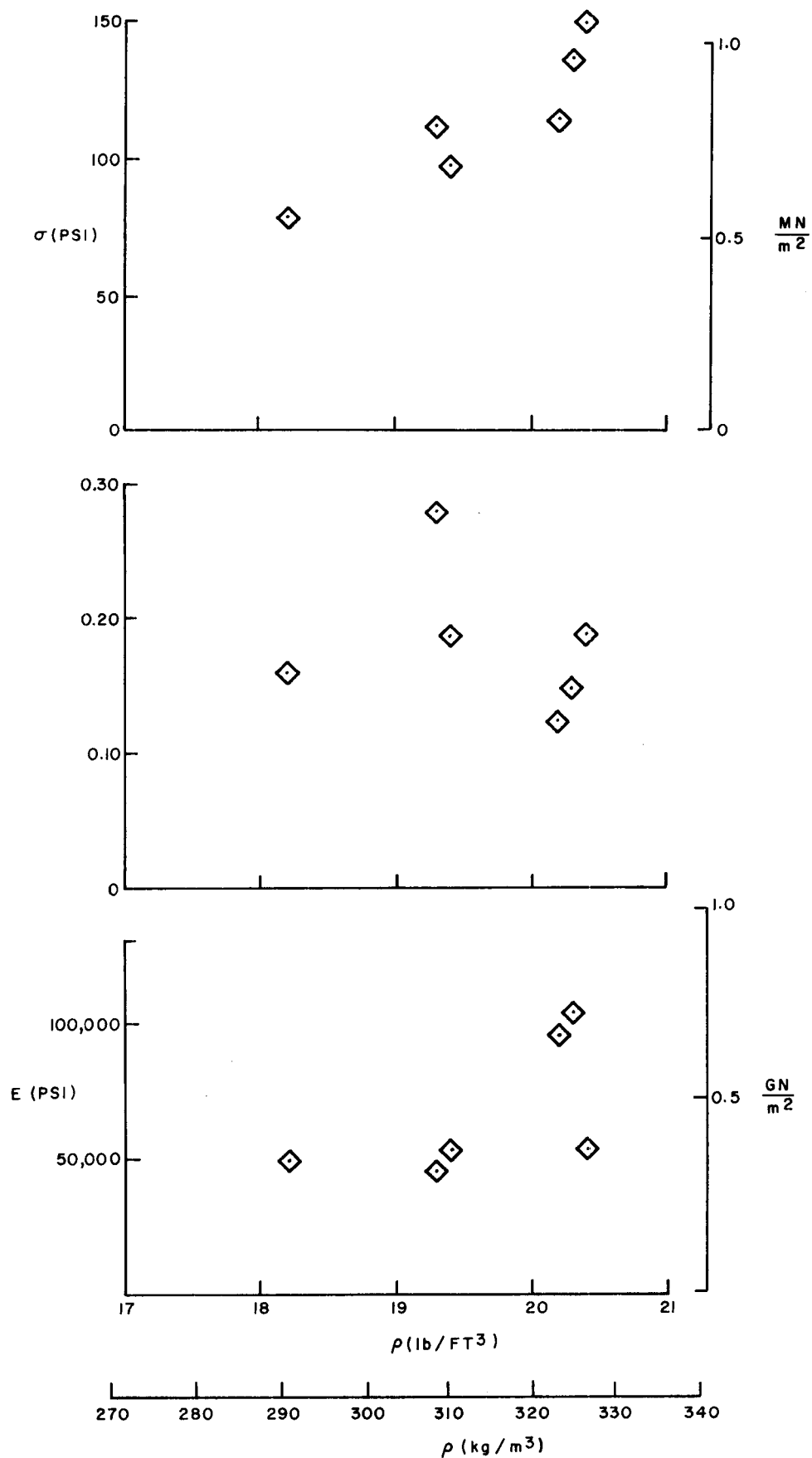
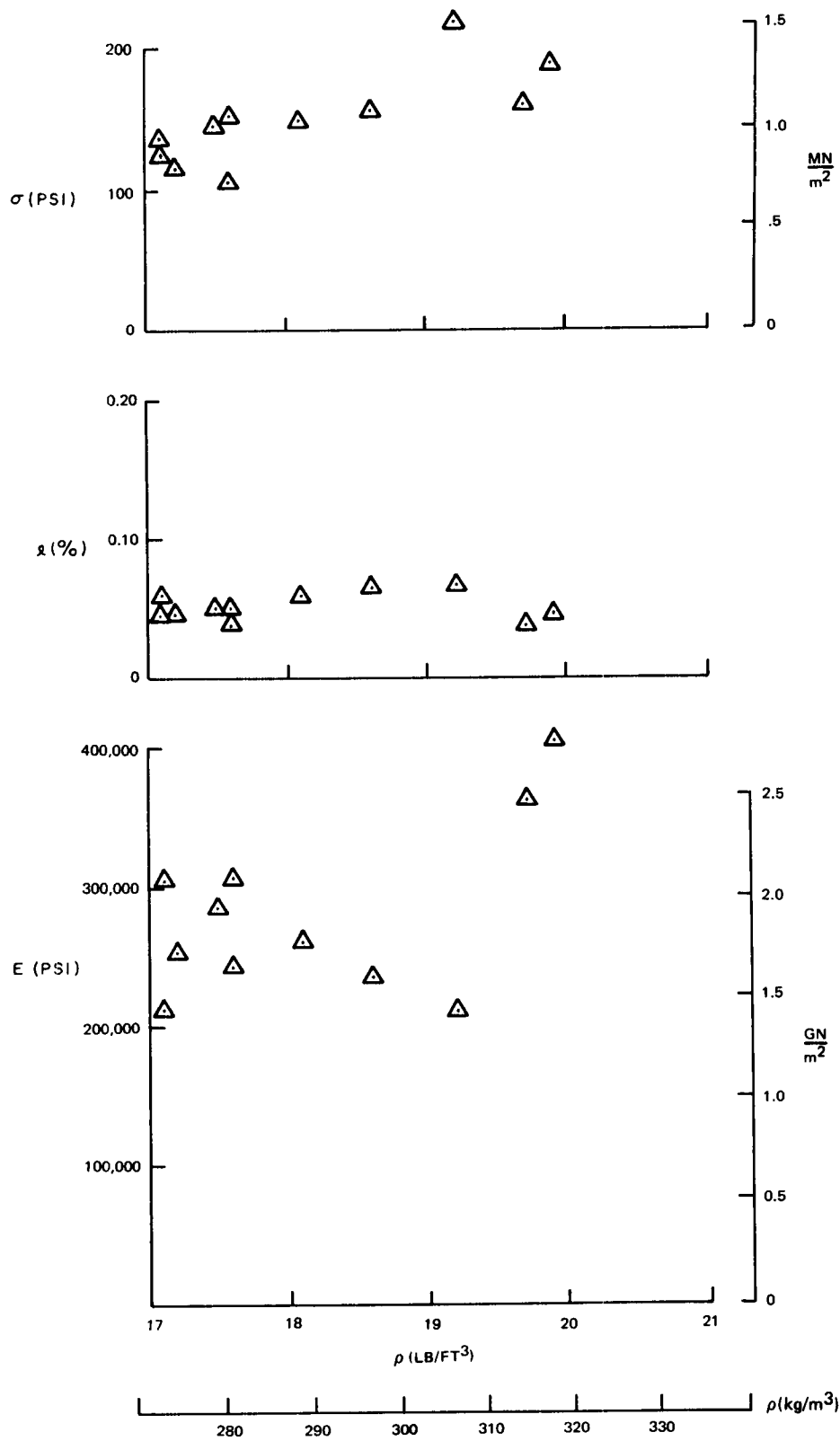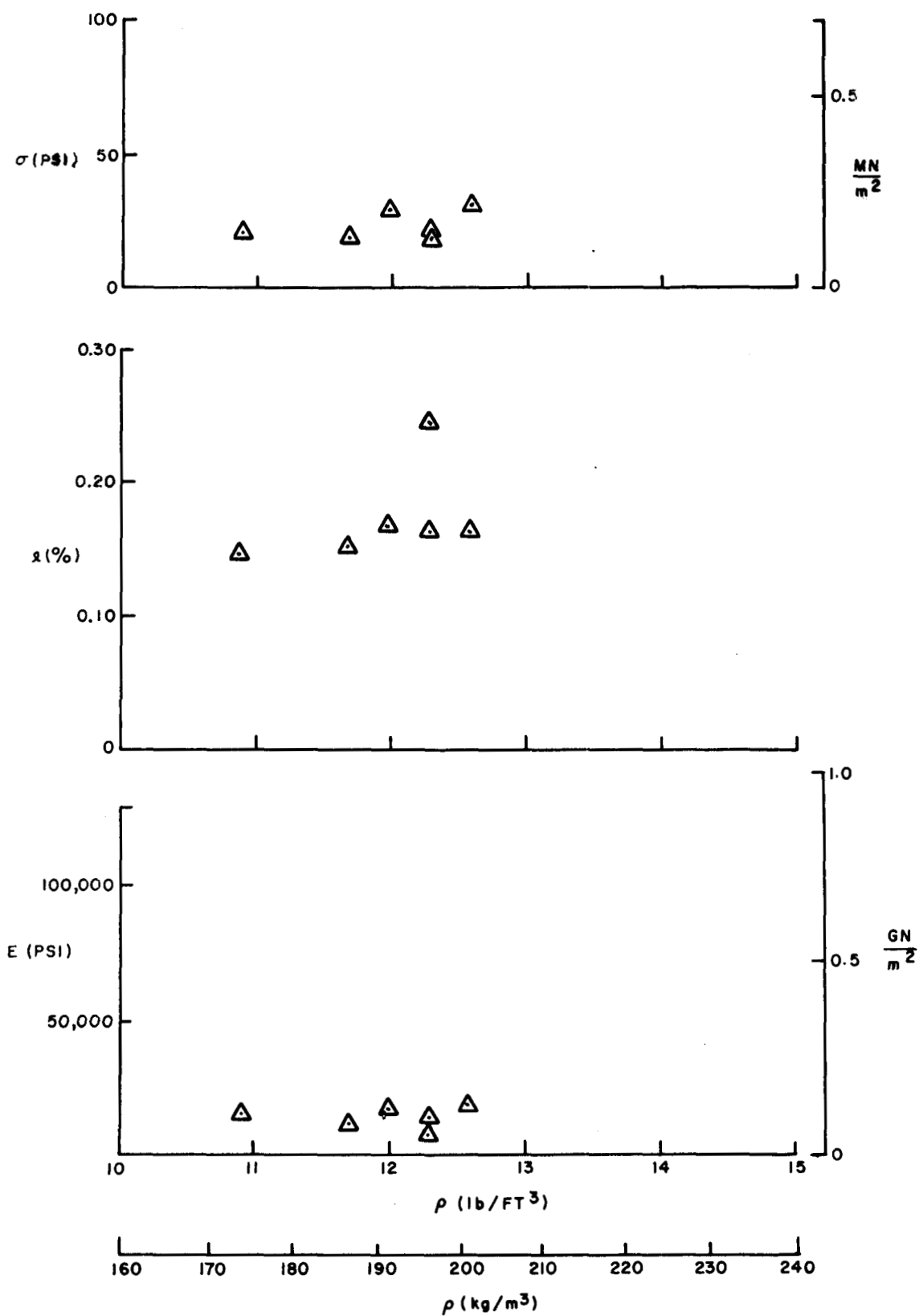Figure A-5. Mechanical behavior of 4μm B&W spun fiber panel-high density (in-plane, tension-FJC-4).

80

Figure A-6. Mechanical behavior of 1.7μm Carborundum fiber panel-high density (in-plane, tension-FJC-1).

81

Figure A-7. Mechanical behavior of 4μm B&W blown fibers panel with as-received fiber length (in-plane, tension FJC-11).
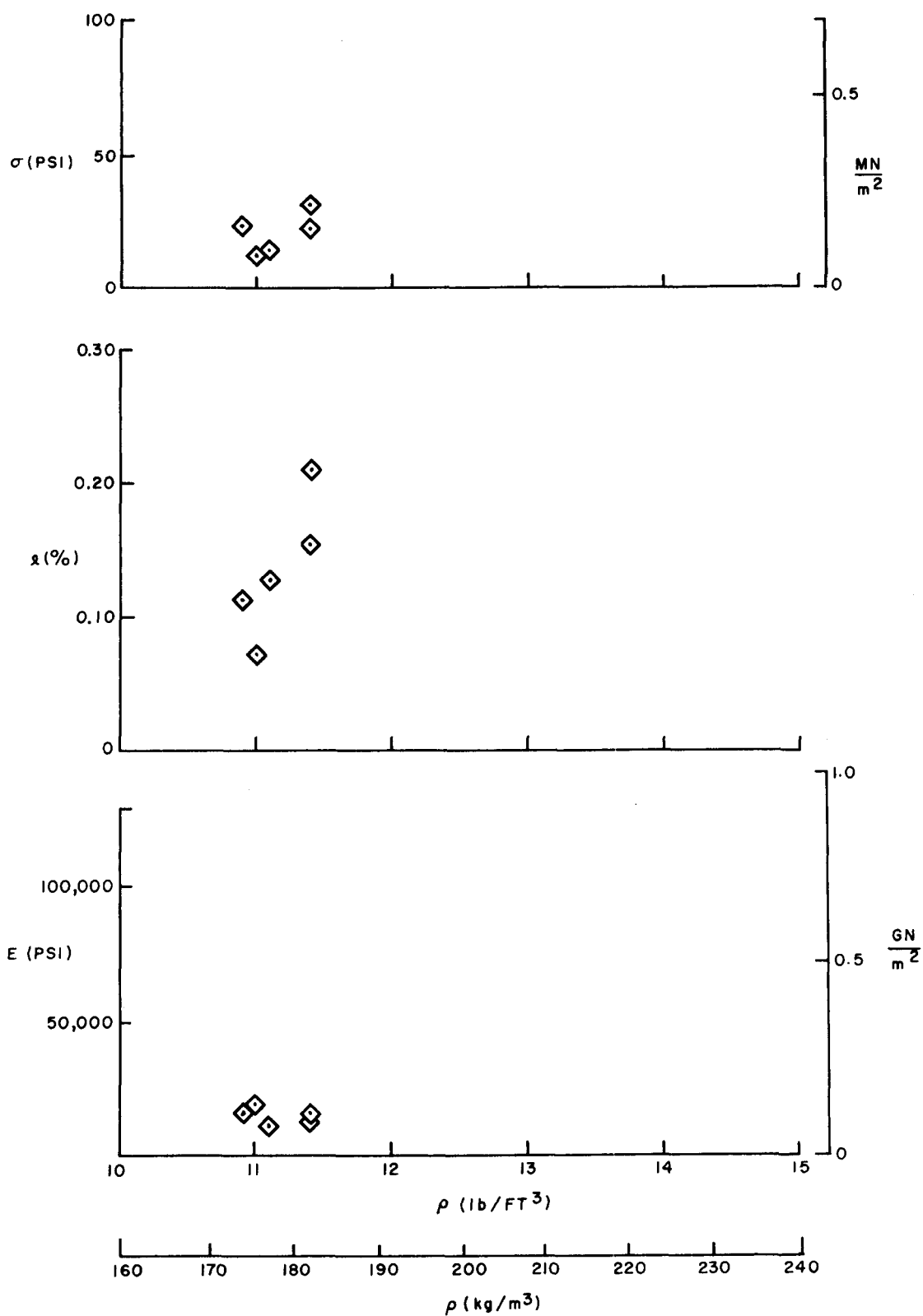
Figure A-8. Mechanical behavior of 4μm B&W spun fiber panel with as-received fiber length (in-plane, tension, FJC-12).
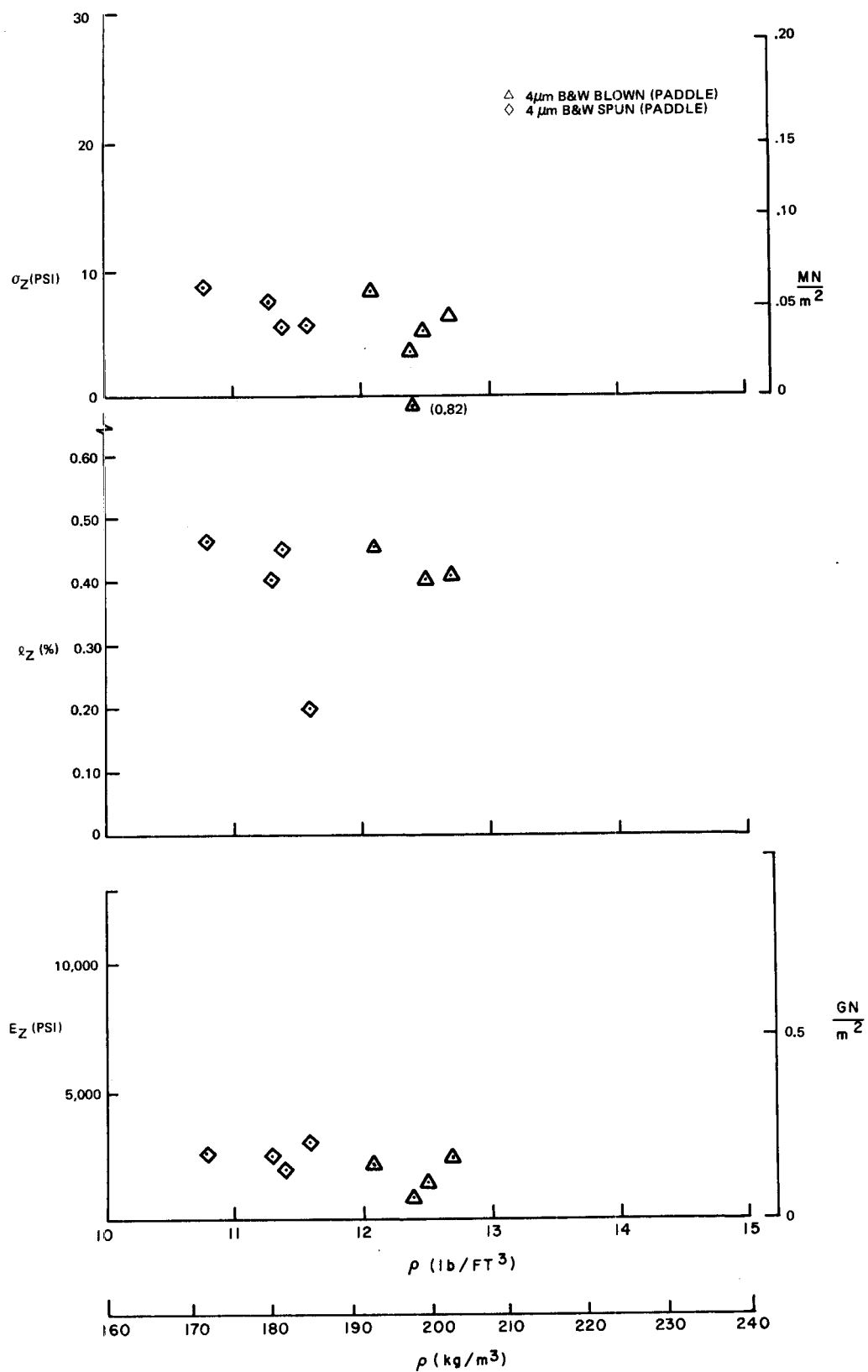
83

Figure A-9. Mechanical behavior of small diameter fiber panels with as-received fiber length (transverse, tension, FJC-11, 12).
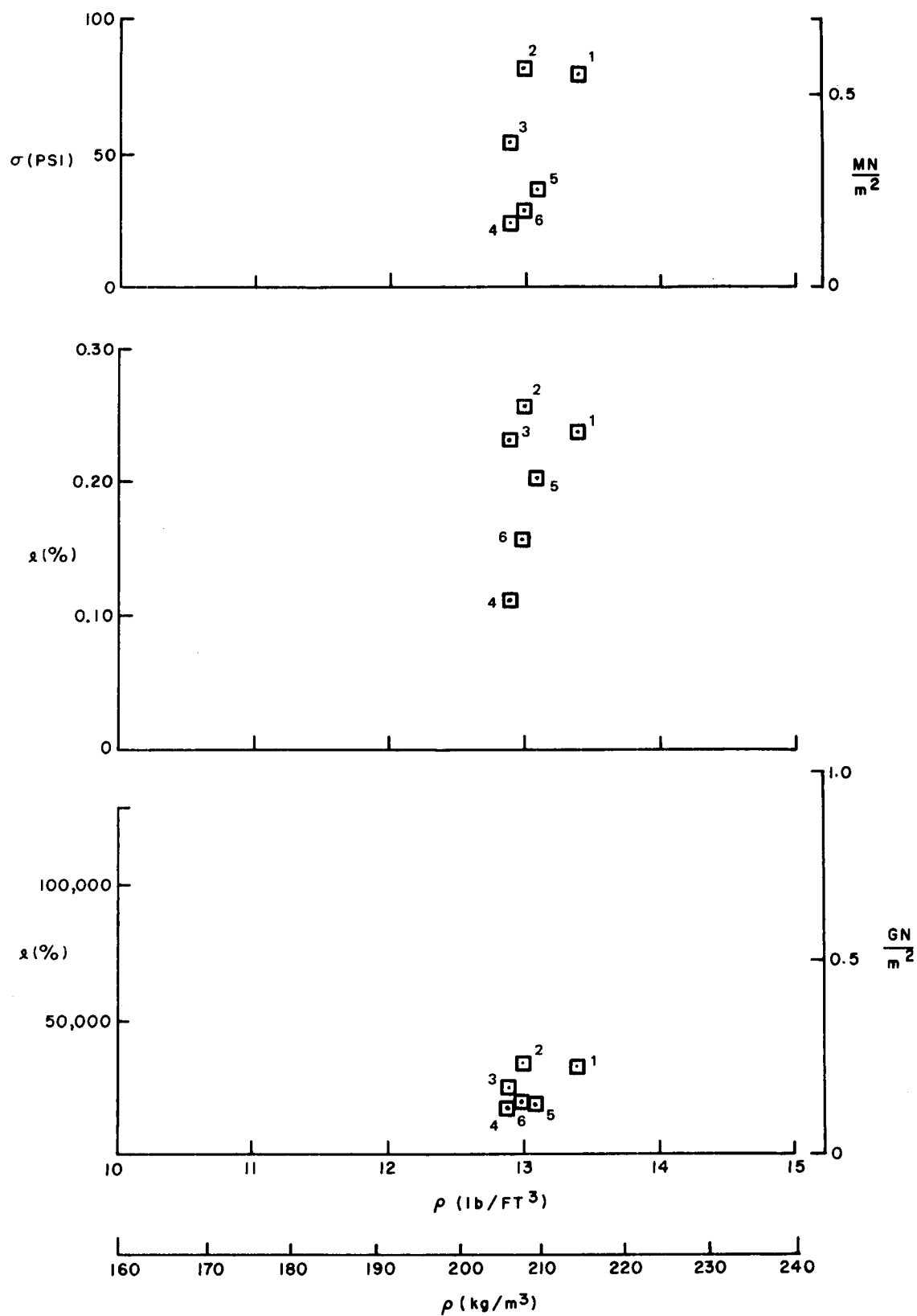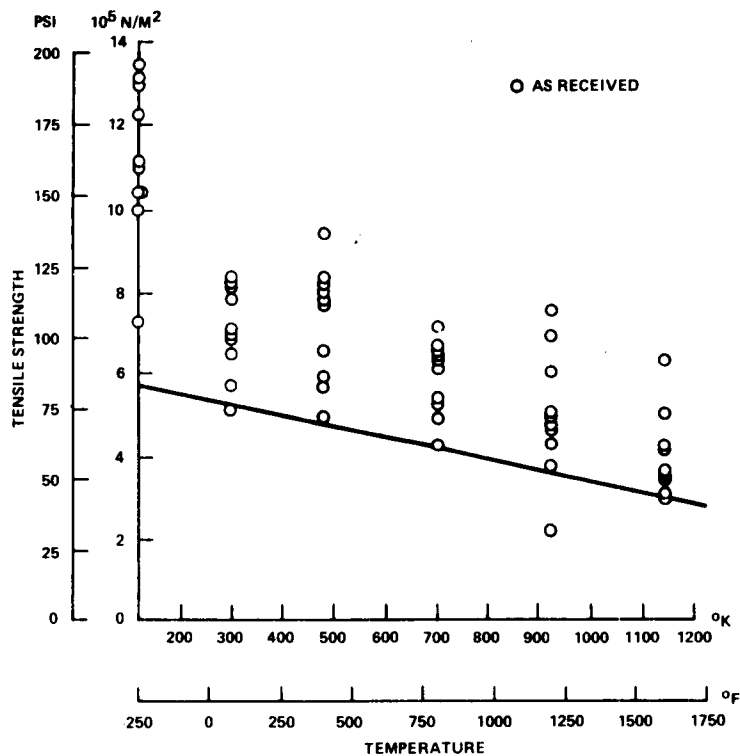
Figure A-10. Mechanical behavior of 4μm B&W spun fiber panel (marine impeller)-
full scale panel (in-plane, tension, FJC-9).

85

Figure A-11. Tensile strength of REI-Mullite Mod 1-B in XY direction (as received).

Figure A-12. Tensile failure strain of REI-Mullite Mod 1-B in XY direction (as received).
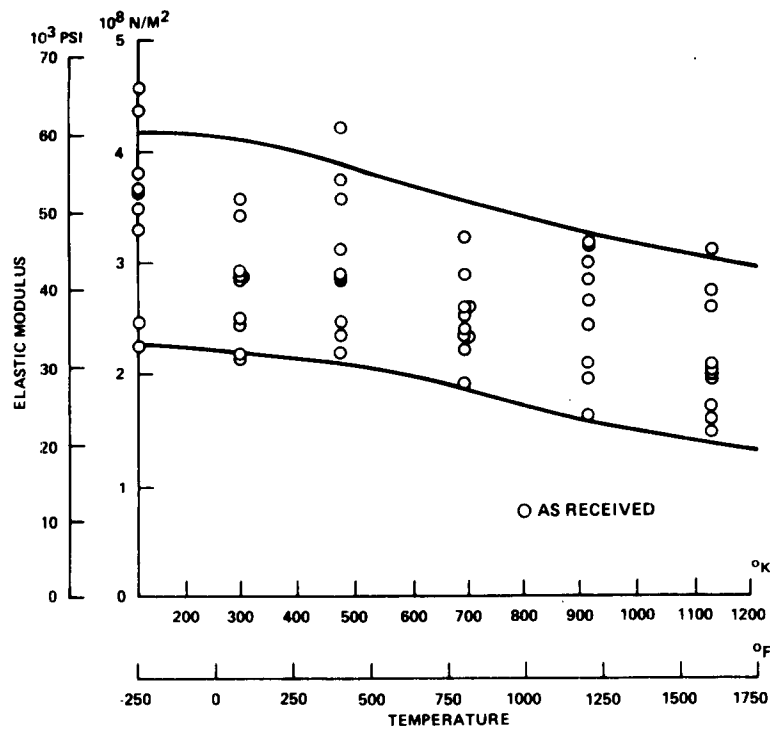
86

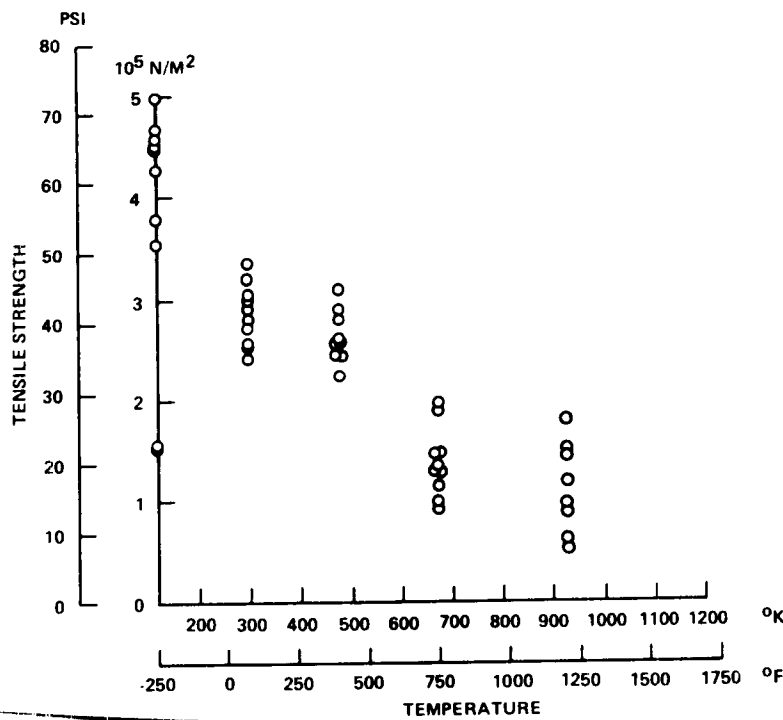Figure A-13. Tensile modulus of REI-Mullite in XY direction (as-received).

Figure A-14. Tensile strength of REI-Mullite in Z direction (as-received).

87

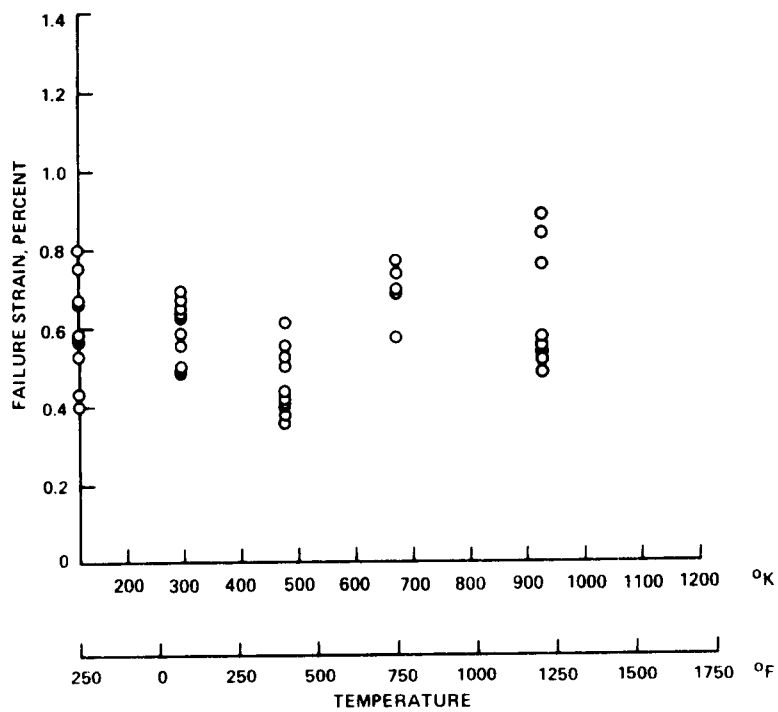Figure A-15. Failure strain of REI-Mullite in Z direction (as-received).
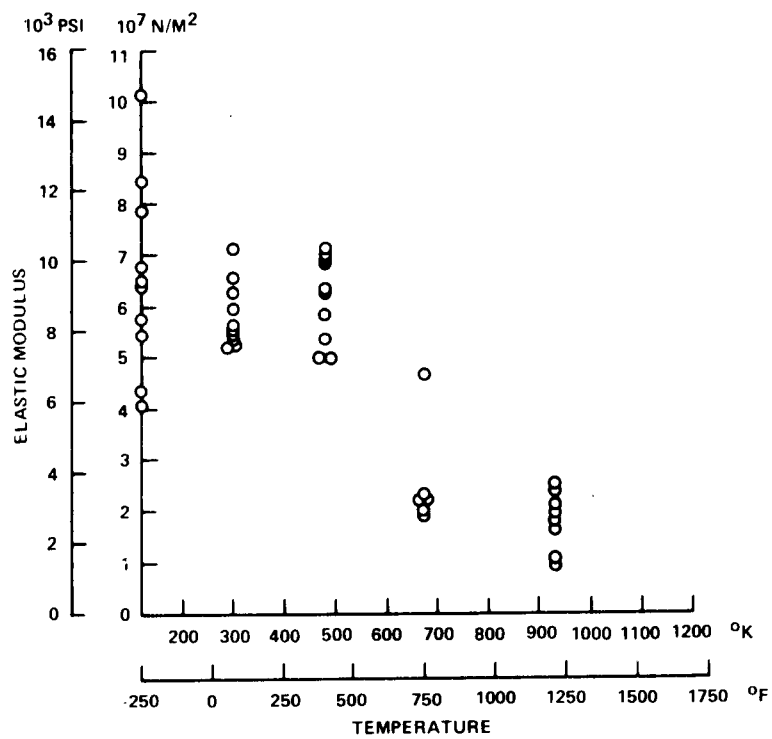
Figure A-16. Tensile modulus of REI-Mullite in Z direction (as received).
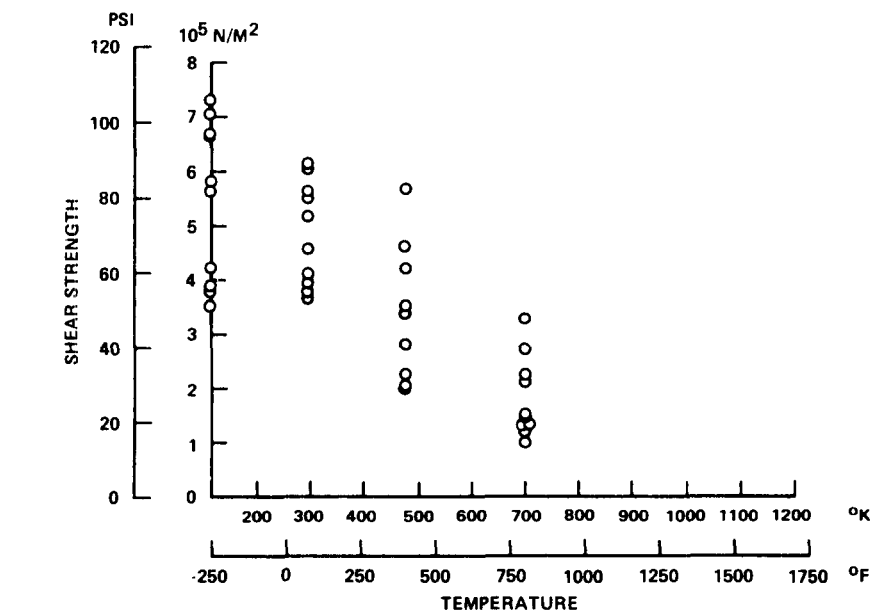
88

Figure A-17. Shear strength of REI-Mullite (as-received).

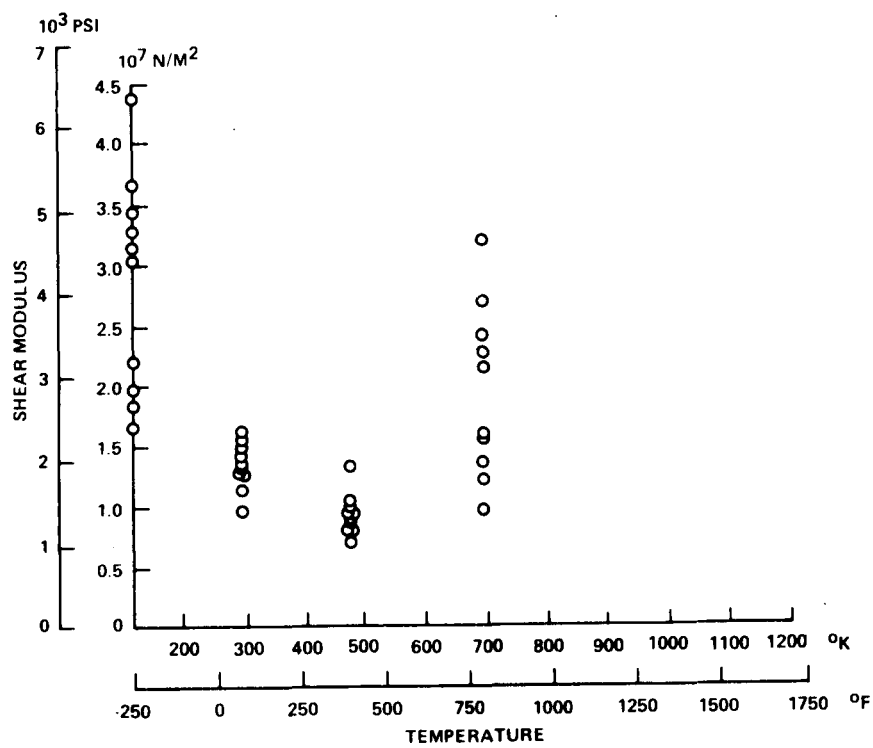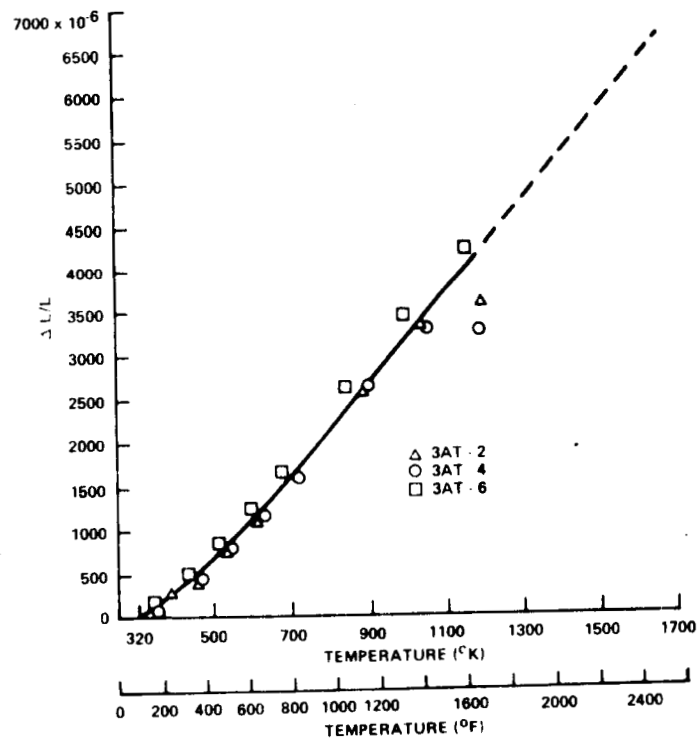Figure A-18. Shear modulus of REI-Mullite (as-received).

89

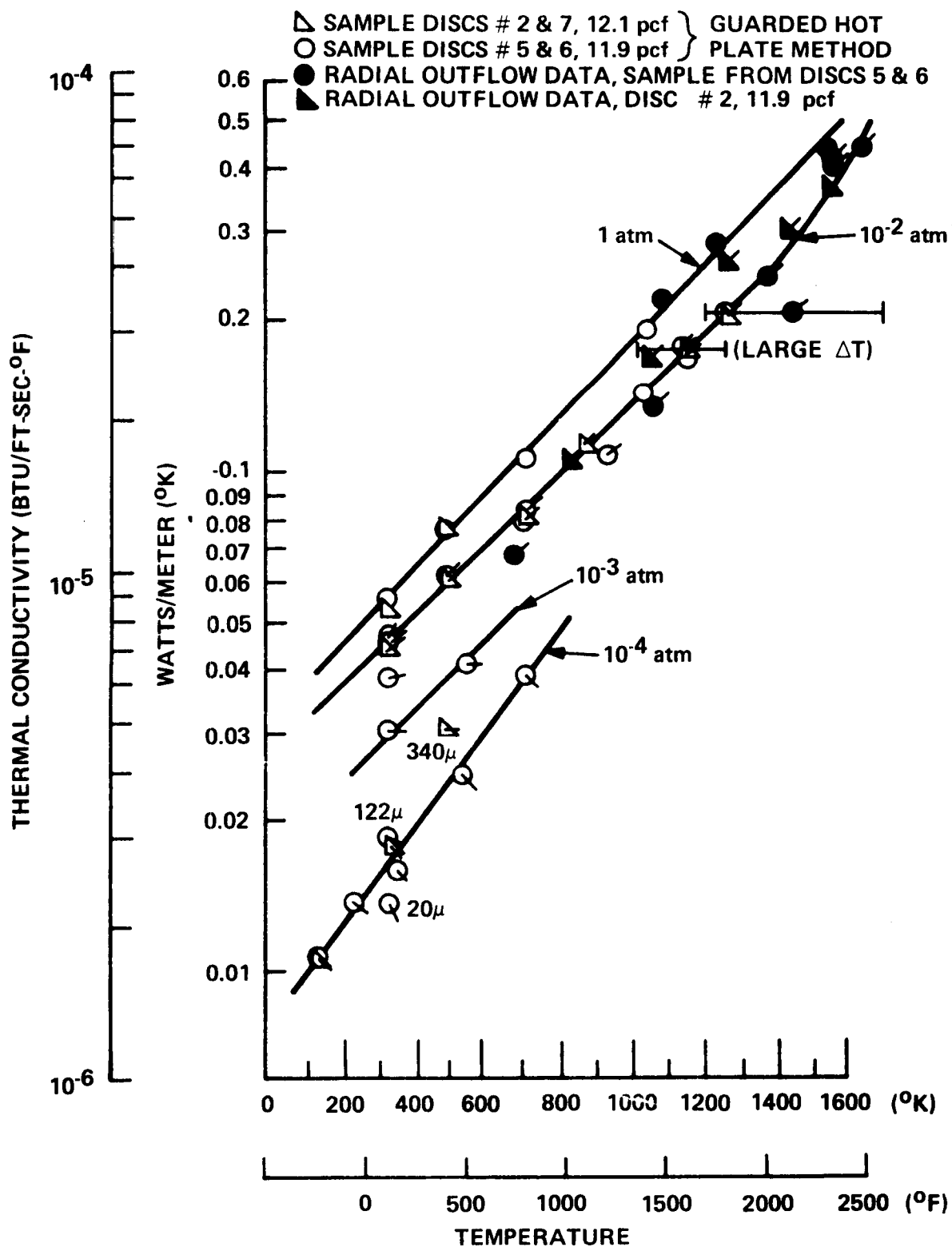Figure A-19. Thermal Expansion of REI-Mullite (as-received).

Figure A-20. Thermal conductivity of REI-Mullite, panel 334, as-fabricated (measured in air at indicated pressures)

APPENDIX 2

PROCESS DESCRIPTION FOR DELIVERABLES

APPENDIX 2

PROCESS DESCRIPTION FOR DELIVERABLES

A.2.1 BABCOCK & WILCOX MULLITE FIBER DESCRIPTION

Fibers are purchased from Babcock & Wilcox Co. in accordance with the B&W Manufacturing control specification:

B&W Salt Decomposition (Mullite) Fibers
Manufacturing Control Specifications

Chemical Analysis	Percentage by Weight
	Al_2O_3 – 77.0% ± 1.0% SiO_2 – 17.0% ± 1.0% B_2O_3 – 4.5% ± 0.5% P_2O_5 – 1.5% ± 0.3% _____ 100.0% Trace Elements – Less than 0.5%
Fiber Diameter	Average of 4.7 ± .5 μm (Microns)
Linear Shrinkage	% (Maximum) – 3% @ 1811°K (2800°F) for 2 hours

NOTE: All values determined by B&W testing methods (this
specification prepared by B&W).

In addition, the fibers shall be free of contamination such as unfiberized salts, machine
scale and other foreign materials.

INFORMATION

1. Fiber diameter determination shall be made by the following technique:

    Transmitted Light Microscopy – representative samples from each batch of
    fiber are placed on a standard petrographic slide, covered with a cover glass
    and examined in transmitted polarized light to determine fiber diameters. A
    point count method and a filar eyepiece are used. One hundred fiber count is
    made. The arithmetic average fiber diameter must be between 4.7 ± .5 μm.

93

2. Shrinkage test shall be conducted by B&W as follows:

Shrinkage Test – a piece of unbonded blanket is accurately cut by a steel rule die from the material 7.62cm x 10.16 cm x "as-processed" thickness. The sample is placed in a muffle furnace for two hours. Maximum allowable lineal shrinkage is 3%.

3. X-ray Analysis – an x-ray diffraction analysis shall be run on each lot of material. The analysis shall show the existence of γ-alumina in the fibers along with an amorphous phase and some mullite. Lack of γ-alumina and an excess of mullite indicate that the fibers are overfired. Figure A-21 shows a typical x-ray pattern of acceptable material. An x-ray film or diffraction pattern verifying compliance with this requirement shall accompany each lot of material.

A.2.2 BASIC INSULATION PROCESS

The Mod 1-B REI-Mullite* fabrication procedure is a proprietary GE-RESD process which has been evolved over a three-year time period. Figure A-22 outlines the process in terms of major processing steps. During the initial processing step, mullite fibers are blended into an aqueous binder solution using a high-speed shear impeller which chops them into desired lengths and disperses the fibers uniformly throughout the binder. The slurry is approximately 80 w/o fiber and 20 w/o binder. Upon firing the binder solution yields the following composition: 74.8 w/o SiO_2, 18.7 w/o B_2O_3 and 6.5 w/o Al_2O_3.

The agitated fibrous slurry is transferred into a mold having a porous base which retains the fibers, but allows passage of the excess binder solution. Rapid binder removal and fiber settling are necessary to maintain proper fiber orientation. The fibers are then compressed to the necessary height to produce the required panel density. After a short residence time in the mold, the panel is removed from the mold and dried in an air-circulating oven. The drying cycle removes binder water and rigidizes the mullite cake to permit subsequent handling and firing.

The dried panel is then fired in a controlled atmosphere to 1533°K (2300°F) for 1 hour. Typical panel density is $192.24 \frac{kg}{m^3}$ (12 pcf) after firing and trimming. Typical mechanical and thermal property data is shown in Figures A-11 through A-20.

*GE-RESD trademark (patent pending)

94

γ·ALUMINA
1.39 Å

γ·ALUMINA
1.98 Å

MULLITE
3.39 Å

MULLITE
5.39 Å

HIGH BACKGROUND
INDICATING A HIGH
GLASS CONTENT.

d-SPACING ——————► Å
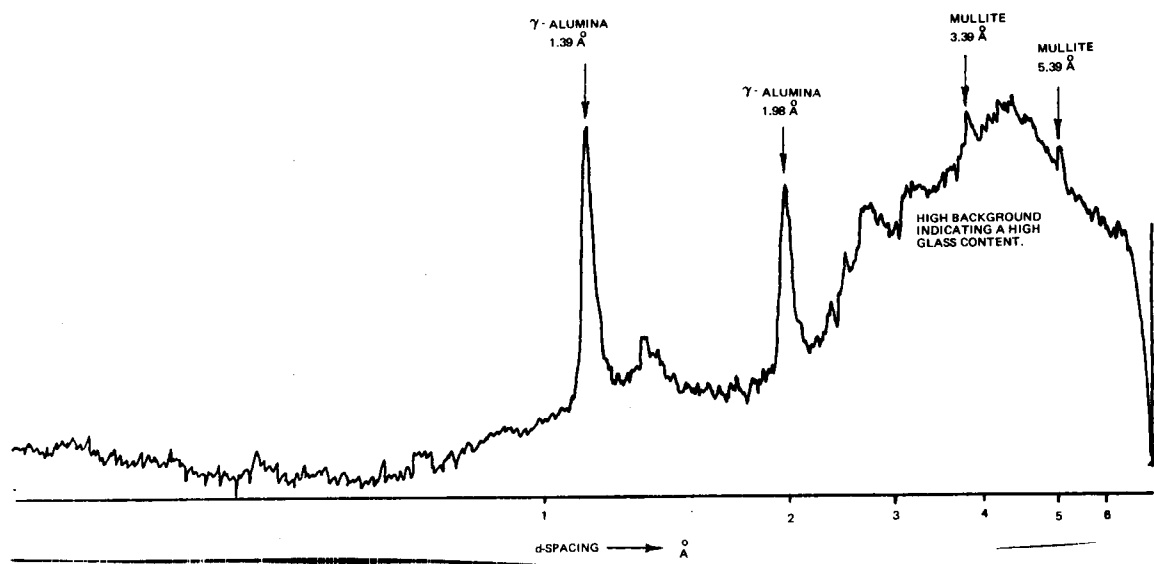
Figure A-21. X-ray diffraction pattern for acceptable fibers.

MOD 1B

CUT
FIBER IN
BINDER (SHEAR
BLADE
CUTTER)

GRAVITY
DRAIN
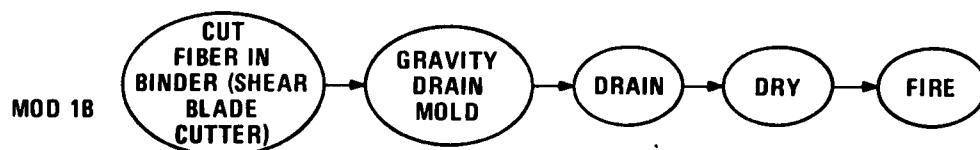MOLD

DRAIN

DRY

FIRE

Figure A-22. Process cycle for Mod 1-B REI-mullite basic insulation.

95

A.2.3 SURFACE COATING PROCESS

<u>Preparation of SR-2 HF-1 Coating</u>. The process consists of two major steps: application of a surface densification layer followed by application of a pigmented surface overcoat. The major constituents for each layer is listed below:

1. Densification Layer (XSR2)

    a.   Petalite (modified)   44.1 w/o

    b.   Kyanite (calcined)   44.1 w/o

    c.   Glass Frit   11.8 w/o

2. Coating Layer (SR-2 HF-1)

    a.   Petalite (modified)   33.25 w/o

    b.   Kyanite (calcined)   33.25 w/o

    c.   Glass Frit   27.75 w/o

    d.   Hafnia   7.75 w/o

A summary of the major processing steps are given below:

<u>Surface Densification</u>

1.   Remove all surface particles and weigh tile.

2.   Wet all surfaces to be densified with distilled H_2O.

3.   Brush slip of XSR2 on surface at a rate of 0.269 kg/m^2.

4.   Air dry for 15 hours minimum.

5.   Furnace dry at 1366°K (2000°F) for 1 hour.

6.   Brush all loose material from surface.

<u>Surface Overcoat</u>

7.   After surface densification, spray the SR-2 HF-1 slip uniformly on the top surface to be coated. Sidewall coating is similarly applied with reduced amount of hafnia.

8.   Allow to air dry for four hours, followed by the following programmed drying cycle.

    1 hr. @ 311°K (100°F)

    1 hr. @ 339°K (150°F)

1 hr. @ 366°F (200°F)

1 hr. @ 383°K (230°F)

9. The coating shall be fired for 1 hr. at 1533°K (2300°F) followed by a 1-hour cycle to 1644° (2500°F) in a sealed enclosure.

10. Weight gain due to XSR-2 and SR-2 HF-1 shall be 1.076 kg/m^2.

APPENDIX 3

PROPERTY CHARACTERIZATION TEST TECHNIQUES

APPENDIX 3

PROPERTY CHARACTERIZATION TEST TECHNIQUES

A.3.1 MECHANICAL PROPERTY TESTING TECHNIQUES

A.3.1.1 Four Point Bending Tests

Four point bending (flexure) tests have been utilized to a limited extent as a screening test for REI strength and stiffness in the in-plane (XY) direction within the as-fabricated panel. Test specimens consist of rectangular parallellepipeds nominally 1.77 cm thick (0.50 in), 1.91 cm wide (0.75 in) and 15.24 to 22.86 cm in length (6 to 9 in). Loading is accomplished with an Instron test machine utilizing a standard four point flexure tool with modified loading and support pads consisting of one inch diameter RTV-560 silicone rubber cylinders. These rubber pads are used in place of the standard, smaller diameter steel parts in order to minimize local compressive deformation in the test specimens. Deformation of the rubber pads is calibrated as a function of applied load using a steel bar having dimensions equivalent to the nominal test specimen dimensions. Using this calibration data, load-deflection curves for test specimens are obtained from load versus test machine cross head displacement traces. Modulus of rupture (flexural strength) and bending modulus are computed from the derived load-deflection curves.

This testing technique was not used extensively since it does not provide a measurement of failure strain, which has been shown to be the most critical mechanical property of REI materials for thermostructural design considerations.

Four point bending tests have also been utilized to obtain tensile properties of REI coating materials. Test specimens for these experiments consist of rectangular parallelopipeds of REI as described above with a coating on the two wider surfaces. When loaded in the four point flexure tool, one surface coating is in uniaxial tension, the other in compression. A bonded, metal-foil strain gage located at the center of the tension face is used to obtain load vs strain curves from which coating strain to failure, elastic modulus and tensile strength are derived. Failure strain data thus obtained are considered to be quite accurate. Strength and modulus data, however, are dependent on the actual thickness of the coating. Since coating thickness varies considerably (as a fraction of total thickness) due to the nature of the substrate, strength and modulus data obtained by this technique are somewhat indeterminate. This points out the need for test technique development studies to devise methods for accurate determination of coating strengths and elastic constants.

A.3.1.2 Bonded Butt Tension Tests

Bonded butt (flatwise) tension tests have been used extensively for the determination of tensile strength, modulus of elasticity and failure strain of REI materials in

both the in-plane (XY) and through thickness (Z) panel orientations. Test specimens consist of rectangular parallelopipeds of REI, 2.54 cm square (1 in) by 2.54 to 5.08 in long (1 to 2 in) bonded to aluminum loading blocks with RTV 102. Loading is accomplished in a table model Instron testing machine equipped with a lightweight chain loading system and a pair of clevises into which the aluminum loading blocks were pinned. This test specimen-load train assembly is shown in Figure A-23. Strain measurements are made with a small, lightweight, clip-on, strain gage extensometer attached directly to the REI material. Very few failures have occurred at the point of extensometer/specimen contact, hence this technique is considered satisfactory for determination of meaningful tensile properties. Extensometer output is recorded continuously as a function of applied load to obtain load-deformation curves from which tensile strength, modulus of elasticity and failure strain are calculated.
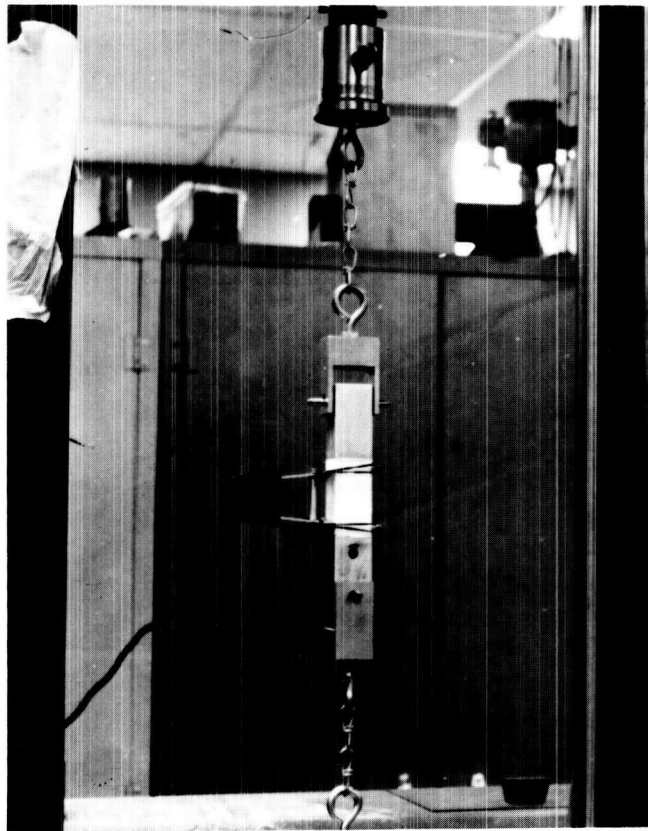

Figure A-23. Extensometer mounted on butt tensile specimen.

100

This testing technique has proven to be a valuable tool for obtaining screening test data for REI material. The specimen geometry is simple, easy to machine and uses a relatively small quantity of material. For design data testing, however, this technique has the limitation of being applicable over only a limited temperature range (i.e., the temperature range where the bond strength exceeds the strength of the REI material under test).

A.3.1.3 "Dogbone" Tension Test

Tensile tests on "Dogbone" type test specimens have been used for determination of in-plane (XY) direction tensile properties of REI materials in the temperature range 172 to 1366°K (-150 to 2000°F). Test specimens are 3.81 cm (1.5 cm) wide with a 2.54 cm (1. in) wide reduced gage section and 0.635 cm (0.25 in) thick. Since this thickness is almost an order of magnitude less than typical as-fabricated panel thicknesses, the "dogbone" specimens have been utilized to investigate the effect of through-the-thickness density gradients on mechanical behavior. Specimens 10.16, 15.24 and 20.32 cm (4, 6, and 8 in) in length have been tested. The 10.16 cm (4 in.) length is used only when dictated by material quantity limitations and the 20.32 cm (8 in.) specimen is used primarily for elevated temperature tests where a longer gage length is required to keep grips out of the hot zone.

Tensile tests of this type are performed in a table model Instron testing machine using pneumatic grips in a rigid load train assembly. Positioning of these grips has been accomplished with the aid of a transit to assure good load alignment. Pneumatic grips are used to permit adjustment of the constant lateral gripping force to obtain specimen failures within the test section without significant slippage from the grips. Strain measurements for these tests are obtained with lightweight, clip-on extensometers as described above for butt tension tests.

Comparative tests using both the "dogbone" and butt tensile specimens on the same panel of material have not shown any significantly different results. This indicates that the effect of specimen cross-section does not influence test results. It is recommended, however, that future characterization testing of REI materials include a more thorough investigation of test specimen size effects.

As mentioned above, elevated temperature tensile tests have been performed using a 15.24 cm long "dogbone" specimen. Heating is accomplished using a high intensity radiant patch heater on either side of the test specimen. Test temperatures are measured and controlled using fine wire thermocouples imbedded in the test specimen. Specimen strain is sensed and recorded as a continuous function of applied load using a lightweight, clip-on, strain gage extensometer with ceramic arms going into the hot zone. Both the room temperature and elevated temperature tension test set-ups are shown in Figures A-24, A-25 and A-26.

Further characterization testing efforts must include continuous evaluation and improvement of mechanical property testing techniques, particularly in the area of strain measurement.
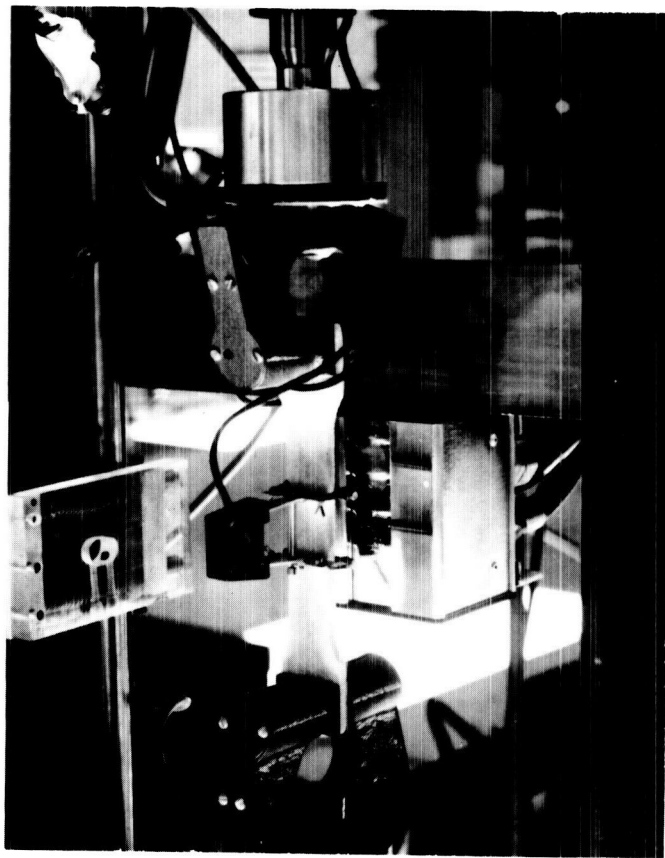
101

Figure A-24. Extensometer mounted on tensile specimen in pneumatic grips (room temperature test set-up).

Compression testing, though more straightforward in technique than tensile testing, has not been utilized as extensively since tensile properties, particularly strain to failure have been shown to be more critical. Compression tests have been performed on rectangular solid specimens 2.54 cm (1 in) square and 5.08 cm (2 in) in height using an Instron test machine for load application. Specimens are loaded between two flat parallel plates. Load train deformations have been calibrated so that specimen load-deformation behavior can be derived from test machine crosshead displacement traces. This technique has proven quite satisfactory since the load levels are sufficiently low that fixture deformation is very small compared to specimen deformation.
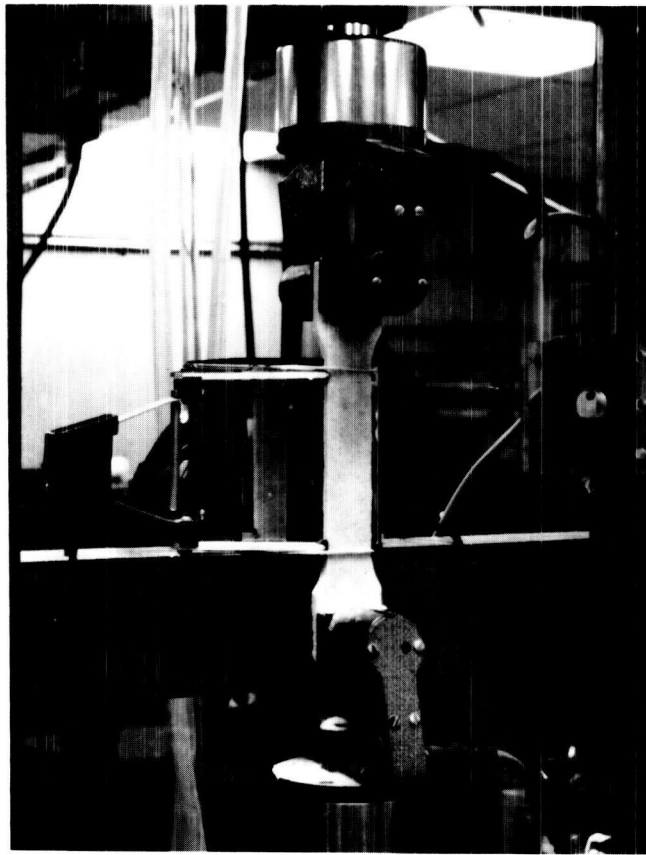
Figure A-25. Extensometer assembly shown complete with radiant patch heater.

A high temperature compression test facility is currently being developed for testing at temperatures up to 1922°K (3000°F). This facility contains a platinum wire resistance furnace and alumina loading rods and platens which are mounted in an Instron test machine. The temperature test technique is basically identical to the room temperature technique described above.

A.3.2 THERMOPHYSICAL PROPERTY TEST TECHNIQUES

A.3.2.1   Thermal Conductivity

Thermal conductivity measurements were made on the Advanced Materials Development Laboratory's new hot plate facility. This instrument is capable of making high accuracy thermal conductivity measurements from cryogenic temperatures to 1273°K and is designed and operated in accordance with ASTM Specification C-177 and recommended high temperature modifications.
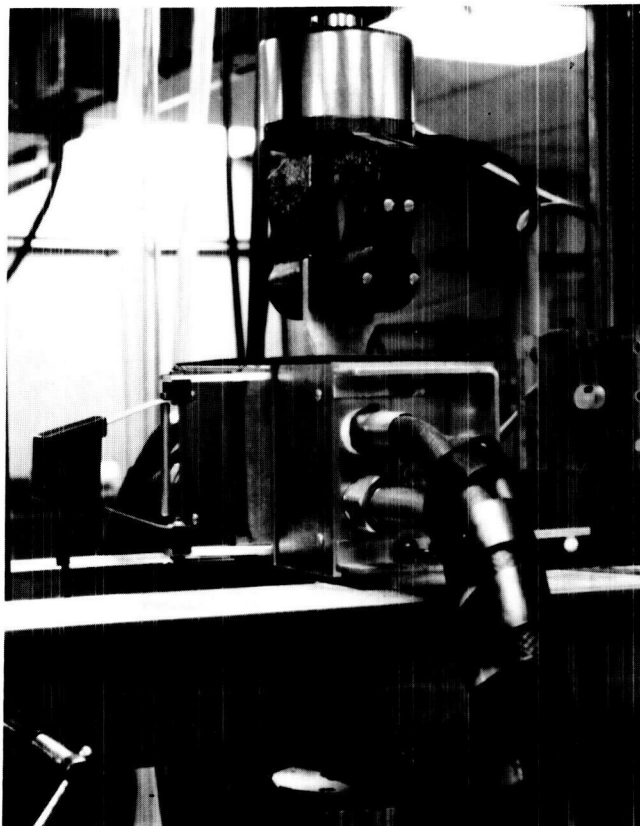
Figure A-26. High temperature tension test set-up with both heaters in place.

The test stack assembly for this instrument is shown in Figure A-27, without the outer guard ring required for reliable operation above about 673°K, or the water-cooled shroud enclosure and low density insulation packing to further prevent radial heat loss. The test samples are evident as two white 20.32 cm (8 in.) diameter discs with the (low temperature aluminum) main guarded heater between them and the top and bottom "cold face" heaters and heat sinks above and below respectively. For high temperature operation alumina ceramic heaters and the outer guard ring are used.

The thermal conductivity measurements are made with a hemispherical vacuum dome and safety guard cage mounted over the stack, resting on the base plate so that the 1.013×10^5, 1.013×10^3 and 10.13 N/m^2 (1, 10^{-2} and 10^{-4} atm) measurements can all be made on the same set-up, changes only being made at about 477°K (400°F) from aluminum to ceramic heaters. Automatic electronic proportional control of the main and auxiliary guards is provided in this instrument.
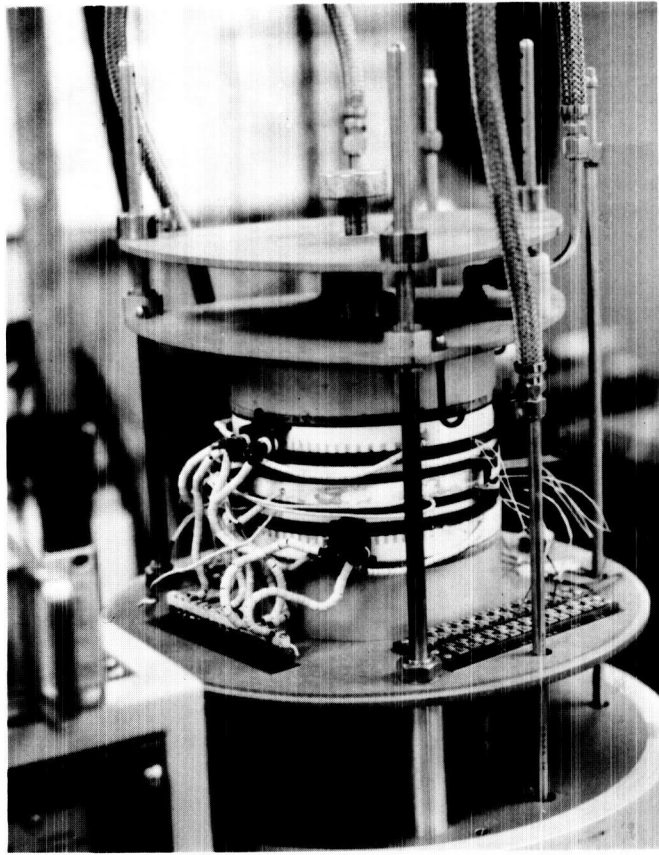
Figure A-27. Guarded hot plate thermal conductivity instrument.

High temperature data, to 1644°K (2500°F) above the guarded hot plate upper limit of 1273°K have been obtained using the radial outflow technique. However, the extremely low thermal conductivity of the material has caused an inordinate amount of axial heat loss up to the central heater, manifested in an apparently higher thermal conductivity, even in temperature ranges covered by the GHP. The problem of lowering and accounting for these losses is being actively studied at this time.

A.3.2.3 Room Temperature Spectral Emittance, Integrated Spectral Emittance, and Solar Absorptance Measurements

1. Emittance by Heated Cavity

A directional heated cavity reflectometer apparatus, designed and fabricated by Gier-Dunkle Instruments, Inc., is used for measurements of the absolute directional, spectral reflectance from 1.0 to 25×10^{-6} m. Figure A-28 shows the directional heated cavity unit mounted on the source-transfer optical system. The assembly consists of a grooved black-nickel cavity (Figure A-29) with 5 separate heaters individually controlled to achieve an isothermal cavity operation at 1061°K (1450°F). The specimen is mounted in a water-cooled holder located at the center of the cylindrical heated cavity, and by rotation of the indexed sample holder, incidence angles between 20 and 75 degrees (0.349 and 1.309 rad) are achieved. The operation of the instrument in both the heated cavity and integrating sphere is presented schematically in Figure A-30. Spectral reflectance data is obtained by comparing the radiant flux reflected from the specimen with that from a platinum fin which is located near the specimen and is used to reduce errors due to non uniformity of the cavity wall intensity. A standard Perkin-Elmer Model 98 monochrometer is used to disperse the reflected energy and direct it into a vacuum thermocouple detector. A sodium chloride prism is used for the 1 to $15 \times 10^{-6} \mu m$ range, and
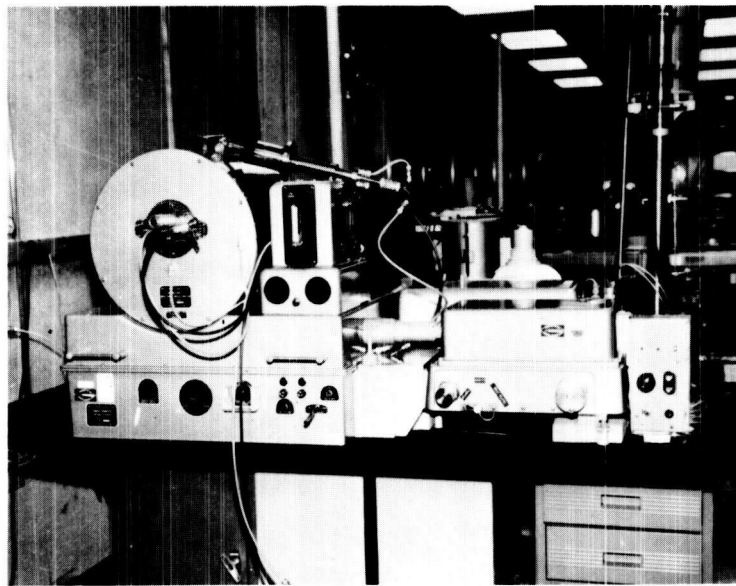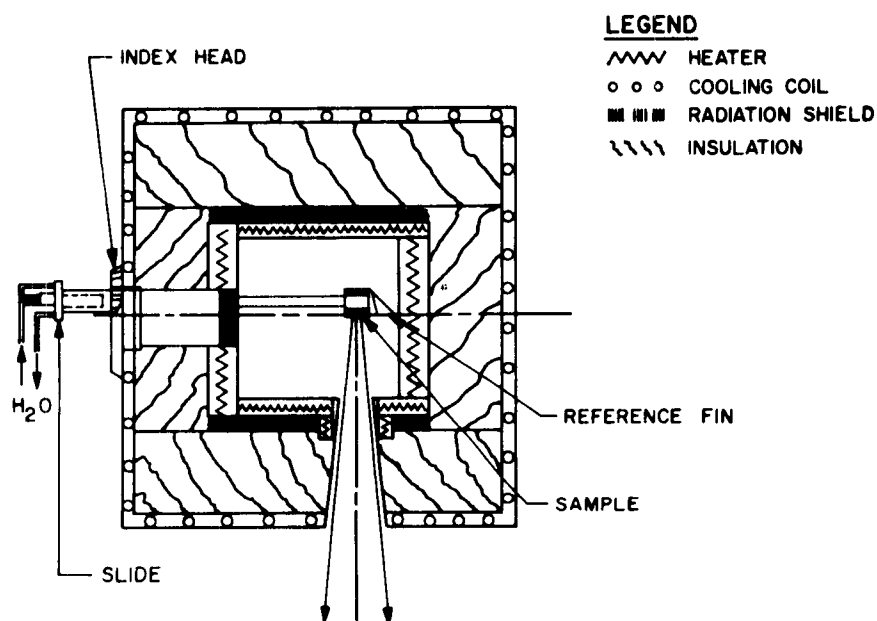

Figure A-28. Gier-Dunkle heated cavity reflectometer.

106

Figure A-29. Schematic of heated cavity and specimen holder.

a potassium-bromide prism for the 13 to 25 x $10^{-6}\mu$m range. The total hemispherical emittance is determined from intermediate infrared, directional spectral reflectance measurements utilizing the following definition:

$$\epsilon_H = \frac{1}{\pi} \frac{\int_0^\pi \int_0^{2\pi} \int_0^\infty \left[1 - \rho_\lambda (\theta, \varphi)\right] E_\lambda \sin\theta \cos\theta \, d\theta \, d\varphi \, d\lambda}{\int_0^\infty E_\lambda \, d\lambda}$$

where:

E_λ is the spectral emissive power

$\rho_\lambda (\theta, \varphi)$ is the directional reflectance as a function of polar angle "θ" measured from the normal to the surface, and

φ is the azimuth angle measured in the plane of the surface from an arbitrary reference.
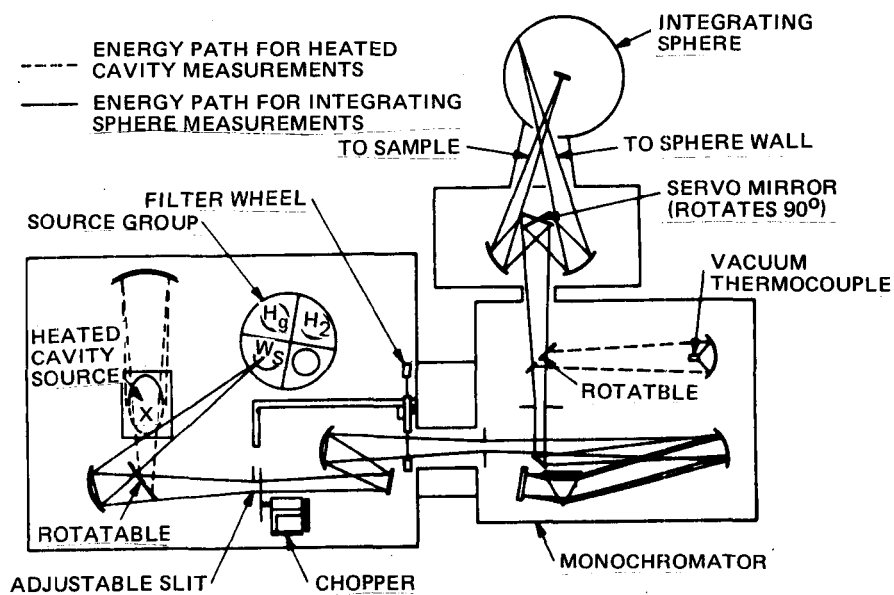
107

Figure A-30. Schematic of the heated cavity source optics in both the heated cavity and integrating sphere (Figure A-31) mode of operation.

2. Gier-Dunkle Absolute Directional Integrating Sphere Reflectometer Solar Absorptance

An integrating sphere directional reflectometer apparatus, designed and fabricated by Gier-Dunkle Instruments, Inc., is used for measurements of the absolute spectral reflectance from 0.30 to 3.0 x 10^{-6} m. Directional solar absorptance (deduced from directional spectral reflectance measurements) may be also determined for angles of incidence from 15 to 80 degrees (0.262 to 1.396 rad). Figure A-31 illustrates the integrating sphere directional reflectometer apparatus and associated auxiliary equipment required for operation. The system consists of a source and transfer optics unit which generates the spectral energy in the solar spectrum. This energy is dispersed spectrally by a monochromator which, in turn, directs monochromatic radiation (wavelengths chosen manually corresponding to two percent of the solar spectrum) into the integrating sphere reflectometer and onto a specimen suspended at the center of the sphere. The reflected radiation and subsequent interreflections from the sphere wall (coated with magnesium oxide) cause a diffuse irradiation upon detectors which view the entire sphere but not the specimen. The detector signal is calibrated when the incident energy is directed past the specimen to the sphere wall by means of a remote-controlled rotary mirror in the optical box. The solar absorptance of surfaces is determined from spectral reflectance measurements by the following numerical integration techniques:

$$\alpha_s = 0.02 \sum (1 - \rho_i)$$

where:

α_s is the solar absorptance

ρ_i is the spectral reflectance determined at wavelength intervals corresponding to two percent of the solar spectrum.

A.3.2.4 High Temperature Total Hemispherical Emittance

A.3.2.4.1 Calorimetry

An absolute calorimetric method was developed for total hemispherical emittance measurement of the coatings developed on this program. The technique used the heated filament method in which the electrical dissipation in the specimen is equated to radiated thermal flux.

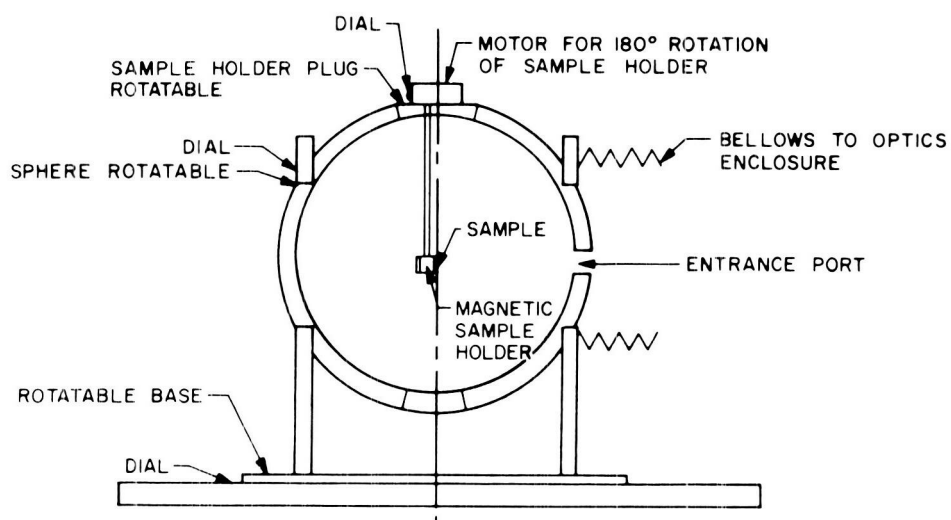$$I \cdot V = \epsilon_H \sigma T^4 \left[Area \right]$$
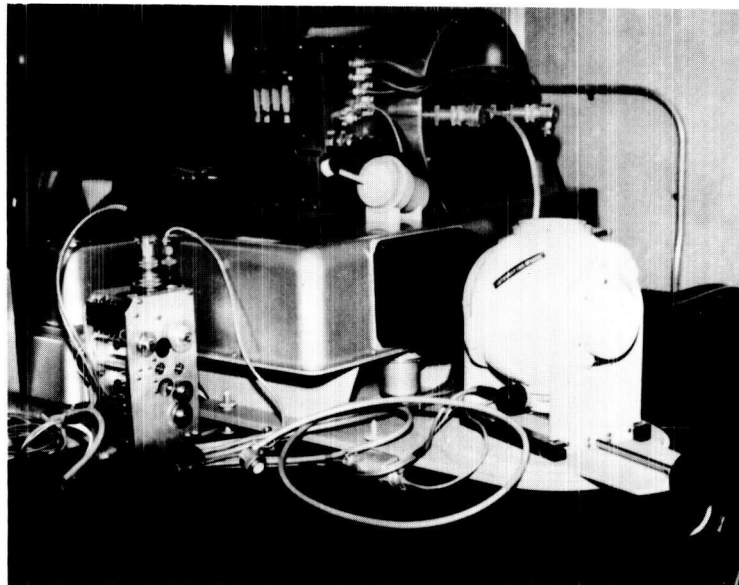
Figure A-31. Integrating sphere directional reflectometer showing cross-sectional view of the sphere.

110

where:

I   = electrical current

V   = electrical voltage

ϵ_H = total hemispherical emittance

σ = Stefan – Boltzmann constant

T   = absolute surface temperature

Area   = surface area of gauge section between voltage probes

Two alternate designs for realizing this condition are shown in Figure A-32. The tube design on the right is to be preferred because it allows use of either an optical pyrometer or surface thermocouple. However, the strip specimen on the left is more flexible for preparation of representative specimens and has been used in the current testing. An actual strip-type specimen is shown in Figure A-33 with the vacuum chamber and control console in the background.
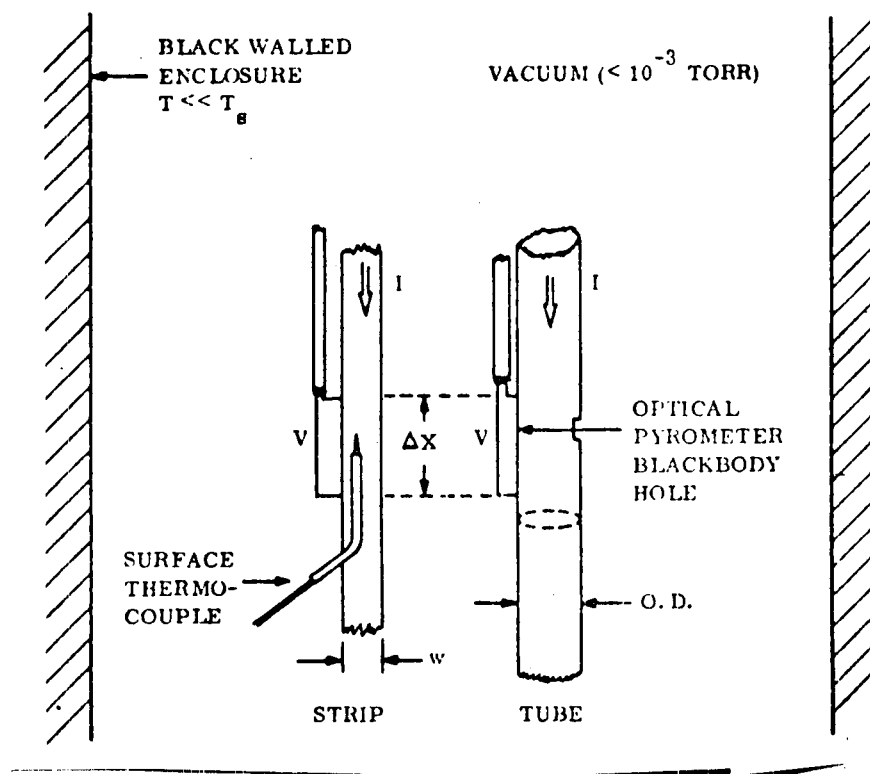

Figure A-32. Schematic of sample designs suitable for absolute calorimetric determination of total hemispherical emittance.
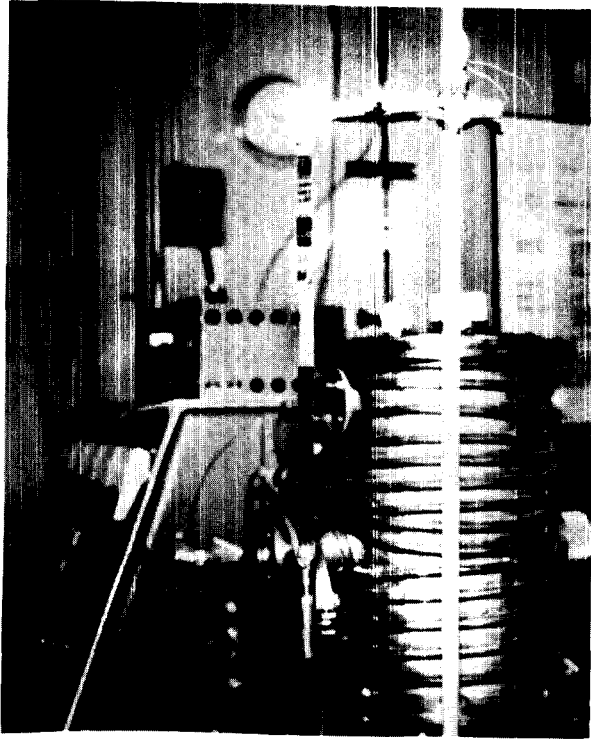
111

Figure A-33. Strip-type, high-temperature total hemispherical emittance specimen.

The measurement must be made in a vacuum of less than 10^{-3} torr to eliminate gaseous conduction to the walls and "chimney effect" convection up the sample strip. Also, the sample enclosure is painted black with Parson's satin finish paint and cooled by chilled water so that reflection and re-radiation to the sample does not occur. The sample design must be thin walled in relation to the radiating area so that axial conduction is significant.

For the design used in this laboratory, it is less than one part in a thousand at 811°K (1000°F) less above that. If these conditions are satisfied the emittance is solved for:

$$\epsilon_H = \frac{I \cdot V}{\sigma T_s^4 \, [\text{Area}]}$$

The sensitivity of this determination to accurate surface temperature measurement can be seen by differentiation:

$$\frac{\partial \epsilon_H}{\partial T_s} = \frac{-4 \; I \cdot V}{\sigma T^5} = \frac{-4}{T} \epsilon_H$$

112

or taking the finite increment form for percentage errors.

$$\frac{\Delta \epsilon_H}{\epsilon_H} = -4 \frac{\Delta T}{T}$$

This shows that the measured emittance error is four times as large as the surface temperature measurement error. Moreover, since the systematic experimental errors of surface temperature measurement are predominantly negative ($\Delta T < 0$), a corresponding positive error is made in indicated emittance. This observation may explain a tendency toward optimistically high emittance data in the literature. The GE strip absolute calorimetric method for total hemispherical emittance has been calibrated on thermo-couple grade platinum strip 1.27 cm (0.50 in) wide by 0.0127 cm (0.005 in) thick in the model geometry shown in Figure A-33. The data points for two successive runs are shown in Figure A-34 compared to the recommended TPRC curve for pure platinum. The maximum absolute deviation is plus 1.2 percent at 780° K (945° F).

This standardization demonstrates the high accuracy of the data obtained on REI coating materials in this program using the absolute calorimetric technique for total hemis-pherical emittance. Note that an absolute error of 1.2% in emittance translates into a smaller relative error in emittance at higher emittance levels ($\Delta \epsilon_H / \epsilon_H$). In addition,
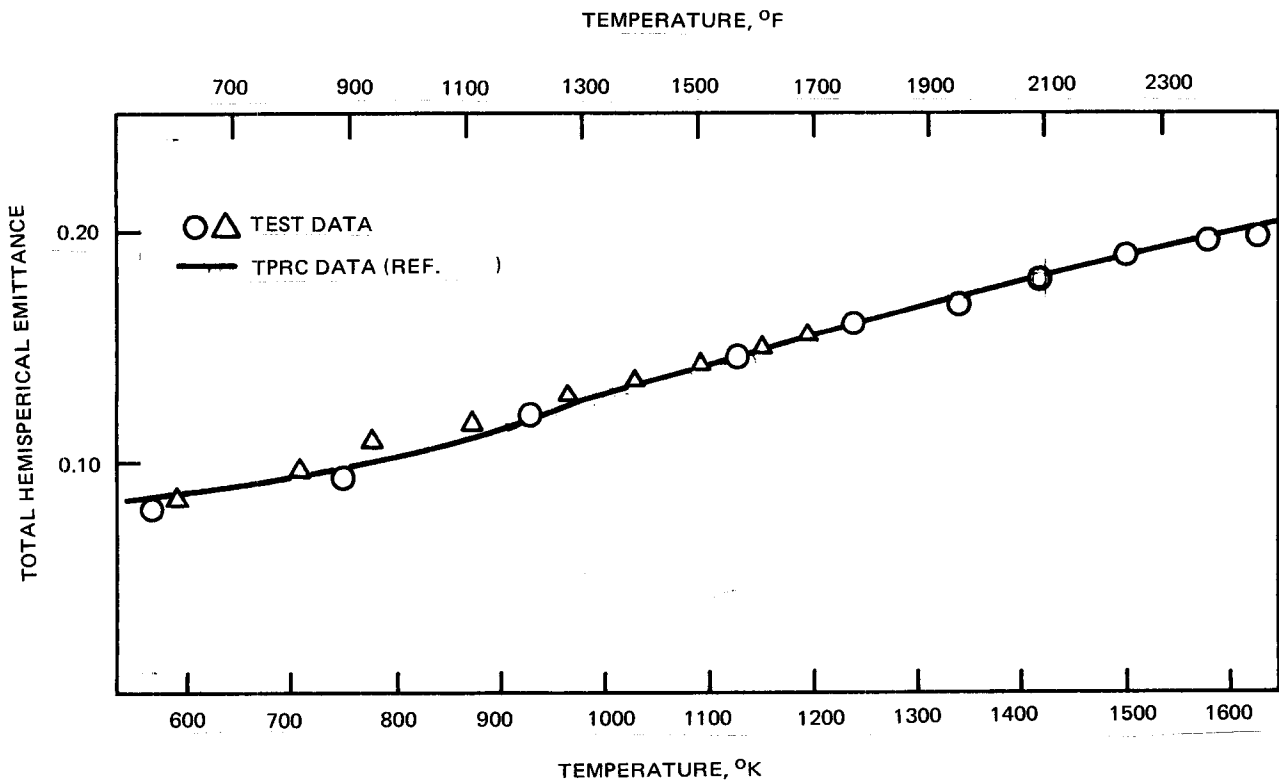

Figure A-34. Calibration of total hemispherical emittance calorimeter using a platinum standard.

the higher emittance levels of the coating measurements correspond to higher voltage and current levels further reducing contributions from these electrical parameters to the error in emittance determination.

3. Radiometric Technique (Push Rod Geometry)

This technique utilizes a radiometer to view a specimen along the axis of a cylindrical furnace. The specimen is mounted on a push rod, (see Figure A-35) which is used to move the specimen from the center of the furnace to a position just outside the furnace. During measurement, the output of the radiometer is plotted as a function of time with an oscillograph recorder as the sample is quickly moved from the position at the center of the furnace to the position at the end. The radiometer observes blackbody radiation, a radiant power level of E_{BB}, from the sample when the sample is at the center of the long tube furnace, regardless of the emittance of the sample because the furnace core and sample plug constitute a blackbody cavity. When the sample is moved to the end of the furnace, the radiant power observed by the radiometer drops to a value of $\epsilon_N E_{BB}$, since only the self-emitted power from the sample is the observed. Hence, the total normal emittance of the sample, ϵ_N, is the ratio of the radiometer output with the sample at the end of the furnace to the radiometer output with the sample at the center of the furnace.

4. Plasma Arc Technique

Plasma arc testing from which total hemispherical emittance was deduced was conducted in the GE Hyperthermal Arc facility, using the tunnel mode of operation. In this mode, flow is delivered to the model at a low supersonic Mach number with a stagnation pressure on the order of 4137 N/m^2 (0.6 psia). Total enthalpy for these runs was nominally 1.16 x 10^7 J/K_g (5000 BTU/lb.).

The facility has two identical perpendicularly mounted model holders which accept 5.08 x 5.08 cm (2 x 2 in.) samples. One holder was used to hold the test sample and the other to hold a calorimeter plate. Heat flux was varied by moving the model closer to the nozzle during the run. Sting positioning was remotely controlled from the control room. Measured heat flux values were corrected to hot wall values using the following equation:

$$\dot{q}_{HW} = \dot{q}_{CW} \left[\frac{H_o - H_{model}}{H_o - H_{calor}} \right]$$

v_S = RAYOTUBE OUTPUT WITH APPARATUS IN THE SAMPLE MEASUREMENT POSITION.

v_B = RAYOTUBE OUTPUT WITH APPARATUS IN THE BLACKBODY POSITION.

$$\epsilon_N = \frac{v_S}{v_B}$$

BLACK BODY POSITION

SAMPLE MEASUREMENT POSITION

FURNACE

PUSH ROD

COATING SAMPLE
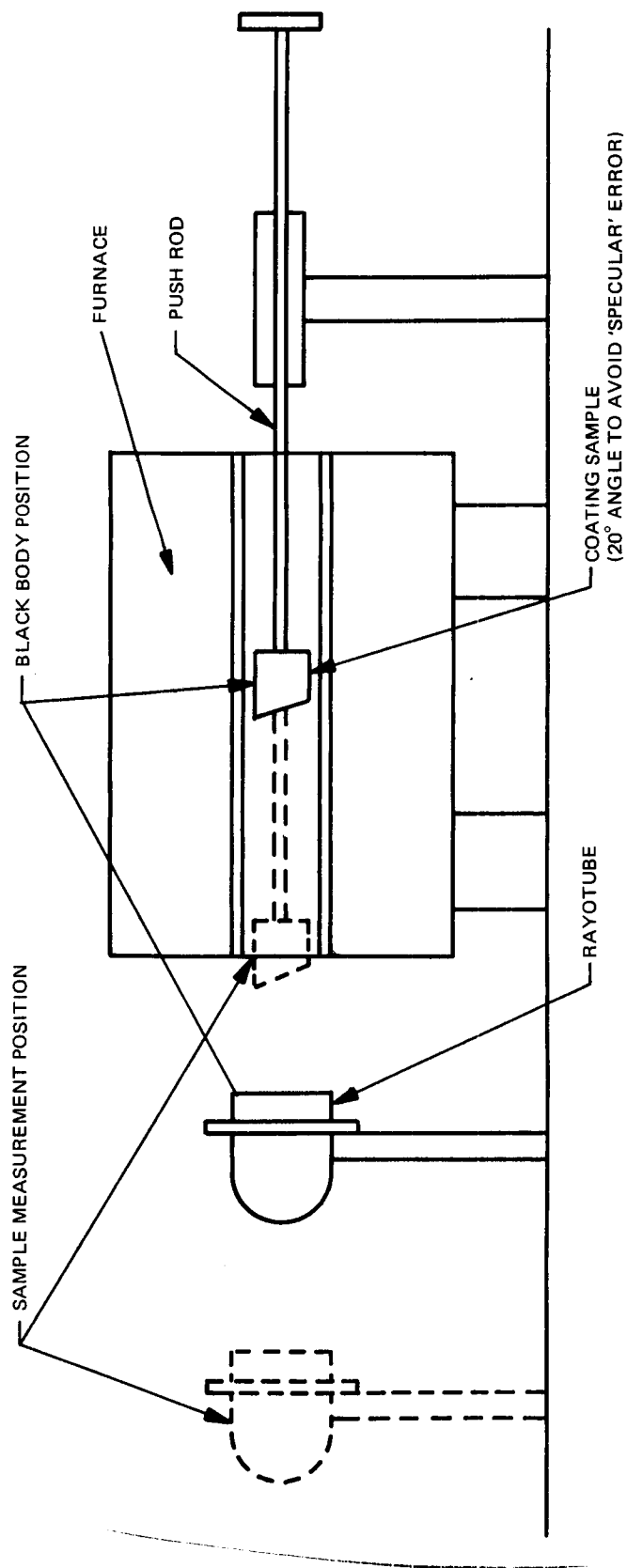(20° ANGLE TO AVOID 'SPECULAR' ERROR)

RAYOTUBE

Figure A-35. "Push rod" comparative method for the measurement of total normal emittance, ϵ_N.

115

Using the measured surface temperatures and the calorimeter heat flux ($\dot{q}_{HW}$) for each data point, the effective surface emittance was calculated. The effective surface emittance, ϵ_{eff}, was then determined using the following energy balance:

$$\varphi \, \dot{q}_{HW} = \dot{q}_{net} + \epsilon \sigma T_W^4$$

where $\quad \epsilon_{eff} = \epsilon/\varphi \;$ and $\; \varphi = \dot{q}_{actual}/\dot{q}_{catalytic}$

and $\dot{q}$ net ≈ 0 in the computation since it comprises only 3% of the total incident heat flux to the material. The value of φ may be greater or less than 1 depending upon the degree of non-catalyticity (or catalyticity).

A.3.3 MICROSTRUCTURAL CHARACTERIZATION - XRD

A.3.3.1 X-Ray Diffraction Procedures

All powders used in this analysis were first sized by passing through a 230 mesh screen. X-ray diffraction specimens consisted of 0.3×10^{-3}m diameter Linderman glass capillaries packed with the appropriate powders. Diffraction photographs were prepared in a 57.3×10^{-3}m diameter powder camera using nickel filtered copper radiation (Figure A-36).

A.3.3.2 Densitometer Traces

A Joyce-Loebl double beam recording micro-densitometer was used to measure and record photographic blackening (Figure A-37). This blackening, in the case of x-ray diffraction photographs, relates to diffracted x-ray intensity.
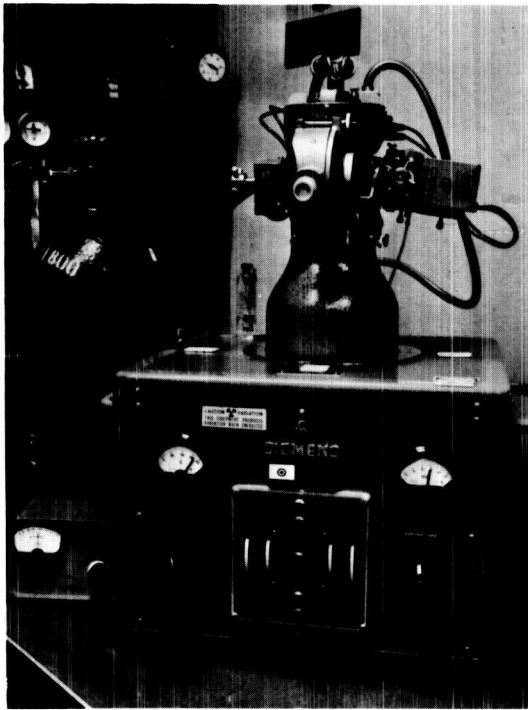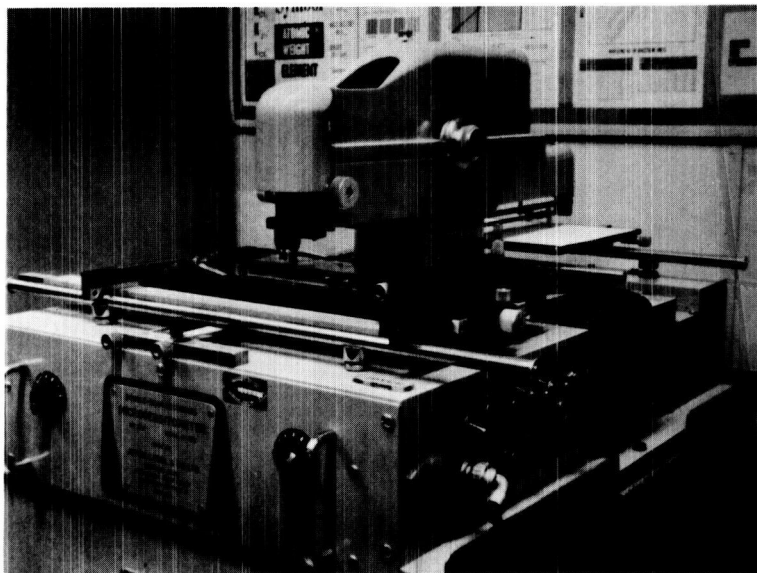
Figure A-36. Siemens powder camera.

Figure A-37. Joyce-Loebl microdensitometer.

117/118

APPENDIX 4

CONVERSION FACTORS FOR UNITS USED IN REPORT

APPENDIX 4

CONVERSION FACTORS FOR UNITS USED IN REPORT

A summary of pertinent conversion factors relating English Units to the International System of units is given below. A more detailed compilation is contained in Reference.

Table A-2. Conversion Factors

To Convert From	To	Multiply By
British thermal unit	joule	1.05587×10^3
Celsius (temperature)	Kelvin	$K = C + 273.15$
Degree (angle)	radian	1.745×10^{-2}
Fahrenheit (temperature)	Celsius	$C = (5/9)(F - 32)$
Fahrenheit (temperature)	Kelvin	$K = (5/9)(F + 459.67)$
foot	meter	3.048×10^{-1}
inch	meter	2.54×10^{-2}
lbm (pound mass)	kilogram	4.536×10^{-1}
mil	meter	2.54×10^{-5}
mm of mercury (0°C)	newton/meter^2	1.33×10^2
lbm/foot^3	kilogram/meter^3	16.0185
micron	meter	10^{-6}
atmosphere	newton/meter^2	1.0133×10^5
lbf/inch^2 (psi)	newton/meter^2	6.8947×10^3
BTU/ft-sec-°F	watts/m-°K	6.23×10^3
calorie (mean)	joule	4.19

119